

“CLEAN” HEAT FLUX SENSOR FOR ASH FOULING MONITORING

by

ZhengYu Hu

A thesis submitted to the Department of Mechanical and Material Engineering

In conformity with the requirements for
the degree of Master of Science Engineering

Queen's University

Kingston, Ontario, Canada

(September, 2009)

Copyright ©ZhengYu Hu, 2009

Abstract

An ash monitoring system prototype that consists of a “clean” heat flux sensor and a “dirty” heat flux sensor was developed in this study. The “clean” heat flux sensor was studied numerically and experimentally while the “dirty” heat flux sensor was tested in the experiment. Two different measurement methods were applied on the “clean” sensor, one from the original study and one proposed in the present work. The new method required additional data processing procedures to be able to work in an on-line basis. Among the three data processing procedures developed in this study the central temperature difference procedure was found to be the most reliable one. Numerical results provided valuable information about the heat transfer pattern at the sensing element and also the performance of the sensor at high radiation heat flux levels. A rough calibration of both “clean” and “dirty” heat flux sensors was conducted experimentally. Nevertheless, the experimental results still served as a primary assessment for both sensors. Observed disagreements between the original study and the present one were probably caused by the modification of the sensor structure made in the present study. Sensitivity variation at high heat flux levels did not appear in the numerical results of either measurement method. Low overall sensor temperature change was believed to be the main reason as it meant less change in thermal properties of the sensing disc. Although the results of the study suggested that the proposed oscillation method was less attractive than the original one, it increased the possibility of resolving the surface characteristic variation problem that was considered crucial for the performances of the “clean” heat flux sensor regardless of the measurement method used.

Acknowledgements

I would like to express my gratitude to my supervisor Dr Darko Matovic for his supervision and support over the course of this work. I would also like to acknowledge the financial support of Ontario Center of Excellence and the assistance from Atikokan Power Station during the *in-situ* test.

Table of Contents

Abstract.....	ii
Acknowledgements.....	iii
Table of Contents.....	iv
List of Figures.....	vi
Nomenclature.....	xii
Chapter 1 Introduction.....	1
1.1 Background.....	1
1.2 Project Scope.....	3
Chapter 2 Literature Review.....	4
2.1 Heat Transfer.....	6
2.1.1 Momentum and Convection Heat Transfer.....	7
2.1.2 Radiation Heat Transfer.....	11
2.1.3 Conduction Heat Transfer.....	14
2.2 Heat Flux Measurement.....	17
2.2.1 Measurement Based On Spatial Temperature Gradient.....	17
2.2.2 Measurement Based On Temporal Temperature Difference.....	20
2.3 Heat Flux Sensors for Ash Fouling Monitoring.....	22
Chapter 3 Sensor Design.....	30
3.1 “Clean” Heat Flux Sensor.....	30
3.1.1 Sensor Structure.....	30
3.1.2 Measurement Concepts.....	34
3.2 “Dirty” Heat Flux Sensor.....	38
3.3 Data Processing Procedures.....	41
Chapter 4 Numerical Model and Results.....	45
4.1 Physical Models.....	46
4.1.1 Turbulence Model.....	46
4.1.2 Wall Functions.....	48
4.1.3 Heat Transfer.....	49
4.2 Model Setup.....	51
4.2.1 Layout and Boundary Conditions.....	51
4.2.2 Grid Setup.....	54
4.2.3 Material Properties.....	56

4.2.4 Numerical Setup.....	57
4.3 Numerical Results.....	58
Grid Sensitivity Test	58
Steady State Results (1mm channel).....	64
Steady State Results (0.5mm channel).....	70
Transient Simulation Results (1mm channel).....	76
Transient Simulation Results (0.5mm channel).....	80
Chapter 5 Experimental Study and Results.....	84
5.1 Apparatus and Setup	84
5.2 Incident Radiation Estimation.....	90
5.3 Experimental Results	94
5.3.1 Steady Radiation Heat Flux	95
Constant Air Flow Rate (1mm channel)	95
Constant Air Flow Rate (0.5mm channel)	100
Oscillating Air Flow Rate (1mm channel).....	104
Oscillating Air Flow Rate (0.5mm channel).....	108
“Dirty” Heat Flux Sensor.....	111
5.3.2 Unsteady Radiation Heat Flux	112
5.4 Data Processing Procedure Assessment.....	114
Chapter 6 Discussion	123
6.1 Comparing Experimental and Numerical Results.....	123
6.2 Discussion on Data Processing Procedures	132
6.3 Comparing RTD and Oscillation Method	135
Chapter 7 Conclusion.....	137
References.....	139
Appendix A Preliminary model results.....	144
Appendix B FLUENT, UDF	148
Appendix C Excel VB, flow control and data acquisition code	150
Appendix D Matlab, data processing	153

List of Figures

Figure 2-1: Energy balance at a system boundary [20].....	6
Figure 2-2: Air flow in “clean” heat flux sensor.....	8
Figure 2-3: Steady laminar and turbulent flow velocities.....	10
Figure 2-4: Relative orientation between two surfaces in space.....	13
Figure 2-5: One-dimensional planar sensor concept [20]	17
Figure 2-6: Schmidt heat flux sensor [18]	18
Figure 2-7: Section and top view of Schmidt-Boelter gage [29]	19
Figure 2-8: Gardon type heat flux sensor [29].....	19
Figure 2-9: Slug calorimeter schematic [29].....	21
Figure 2-10: Inserted thermocouples [1].....	23
Figure 2-11: Guarded cylinder heat flux sensor, a) surface mounted, b) embedded [1].....	23
Figure 2-12: Thermocouple locations in the guarded cylinder sensor [35]	24
Figure 2-13: Disc type heat flux meter [1].....	24
Figure 2-14: Disc type heat flux meter [33].....	25
Figure 2-15: Heat flux sensor with an air screen [37].....	25
Figure 2-16: a) Structure [14] and b) operation principle of the “clean” heat flux sensor.....	26
Figure 2-17: Disc temperature field under $4.6 \cdot 10^{-3} \text{ m}^3/\text{s}$ air flow rate [15]	28
Figure 2-18: Sensor response curve: a) analytical results, b) experimental results [15].....	28
Figure 2-19: Cross section view of the porous media sensor [29].....	29
Figure 3-1: Access port on the boiler wall.....	30
Figure 3-2 : Body of the heat flux probe with sensor tip detached.....	31
Figure 3-3: Rear end of the “clean” heat flux probe	31
Figure 3-4: Sensor tip components a) outer casing, b) sensing element.....	31
Figure 3-5: Sensing element connected to casing by three screws	33
Figure 3-6: “Clean” sensor thermocouple installation.....	33
Figure 3-7: Tip of the “dirty” heat flux sensor a) top view, b) bottom view	39
Figure 3-8: Assembled “dirty” heat flux sensor.....	39
Figure 3-9: Structure of the “dirty” heat flux sensor	40
Figure 3-10: Rear end of the “dirty” sensor probe.....	40
Figure 4-1: Layout for preliminary models (all units in mm).....	52
Figure 4-2: Layout and boundary conditions for final model (1mm channel).....	53
Figure 4-3: Layout for final model (0.5 mm channel).....	53

Figure 4-4: Grid within and near the sensor (preliminary model)	55
Figure 4-5: Grid within and near the sensor (final model).....	55
Figure 4-6: Velocity profile in the annular channel, $\dot{m}=2\text{g/s}$, $\text{Re}=14061$, \blacklozenge Coarse, \square Medium, \blacktriangle Fine, location: a) $x/H=0$, b) $x/H=0.3$, c) $x/H=1$	60
Figure 4-7: Velocity profile in the annular channel, $\dot{m}=7.9\text{g/s}$, $\text{Re}=56243$, \blacklozenge Coarse, \square Medium, \blacktriangle Fine, location: a) $x/H=0$, b) $x/H=0.3$, c) $x/H=1$	61
Figure 4-8: Velocity profile of the annular jet, $\dot{m}=2\text{g/s}$, $\text{Re}=14061$, \blacklozenge Coarse, \square Medium, \blacktriangle Fine, location: a) $x/D_i=0.1$, b) $x/D_i=1$, c) $x/D_i=4$	62
Figure 4-9: Velocity profile of the annular jet, $\dot{m}=7.9\text{g/s}$, $\text{Re}=56243$, \blacklozenge Coarse, \square Medium, \blacktriangle Fine, location: a) $x/D_i=0.1$, b) $x/D_i=1$, c) $x/D_i=4$	63
Figure 4-10: Path line in the annular channel, a) $\dot{m}=2\text{ g/s}$, $\text{Re}=14061$, b) $\dot{m}=7.9\text{ g/s}$, $\text{Re}=56242$	64
Figure 4-11: Center recirculation zone, a) $\dot{m}=2\text{ g/s}$, $\text{Re}=14061$, b) $\dot{m}=7.9\text{ g/s}$, $\text{Re}=56242$	64
Figure 4-12: Total heat flux variation along the radius of the top sensor surface, \blacksquare BFT=800K, \blacktriangle BFT=1000K, \blacklozenge BFT=1200K, \square BFT=1400K, \triangle BFT=1600K, \diamond BFT=1700K, a) $\dot{m}=2\text{ g/s}$, b) $\dot{m}=7.9\text{ g/s}$	66
Figure 4-13: Total heat flux variation in axial direction along circumference surface sensor surface, \blacksquare BFT=800K, \blacktriangle BFT=1000K, \blacklozenge BFT=1200K, \square BFT=1400K, \triangle BFT=1600K, \diamond BFT=1700K, a) $\dot{m}=2\text{ g/s}$, b) $\dot{m}=7.9\text{ g/s}$	67
Figure 4-14: Temperature variation in radial direction at the bottom surface of the sensing element, \blacksquare BFT=800K, \blacktriangle BFT=1000K, \blacklozenge BFT=1200K, \square BFT=1400K, \triangle BFT=1600K, \diamond BFT=1700K, a) $\dot{m}=2\text{ g/s}$, b) $\dot{m}=7.9\text{ g/s}$	69
Figure 4-15: Sensitivity for RTD method (1mm channel), \blacklozenge $\dot{m}=2\text{g/s}$, \square $\dot{m}=7.9\text{g/s}$	70
Figure 4-16: Path line in the annular channel a) $\dot{m}=0.95\text{ g/s}$, $\text{Re}=7071$, b) $\dot{m}=3.8\text{ g/s}$, $\text{Re}=28282$	71
Figure 4-17: Center recirculation zone, a) $\dot{m}=0.95\text{ g/s}$, $\text{Re}=7071$, b) $\dot{m}=3.8\text{ g/s}$, $\text{Re}=28282$	71
Figure 4-18: Total heat flux variation along the radius of the top sensor surface, \blacksquare BFT=800K, \blacktriangle BFT=1000K, \blacklozenge BFT=1200K, \square BFT=1400K, \triangle BFT=1600K, \diamond BFT=1700K, a) $\dot{m}=0.95\text{ g/s}$, b) $\dot{m}=3.8\text{ g/s}$	72
Figure 4-19: Total heat flux variation in axial direction along circumference surface sensor surface, \blacksquare BFT=800K, \blacktriangle BFT=1000K, \blacklozenge BFT=1200K, \square BFT=1400K, \triangle BFT=1600K, \diamond BFT=1700K, a) $\dot{m}=0.95\text{ g/s}$, b) $\dot{m}=3.8\text{ g/s}$	73

Figure 4-20: Temperature variation in radial direction at the bottom surface of the sensing element, ■ BFT= 800K, ▲BFT= 1000K, ◆ BFT=1200K, □ BFT=1400K, △ BFT=1600K, ◇ BFT=1700K, a) $\dot{m}=0.95$ g/s, b) $\dot{m}=3.8$ g/s.....	75
Figure 4-21: Sensitivity for RTD method (0.5mm channel), ◆ $\dot{m}=0.95$ g/s, □ $\dot{m}=3.8$ g/s	76
Figure 4-22: Air flow rate oscillation (1mm channel)	77
Figure 4-23: Estimated net internal energy and the corresponding T_c oscillation (1mm channel), ◆ Net internal energy change, ■ T_c	78
Figure 4-24: Oscillation of the total heat transfer rate oscillation at the top, circumference and bottom surfaces and rate of internal energy change (1mm channel), ■ q'_{top} , △ q'_{cir} , * q'_{bot} , ○ $d\Delta E_{net}/dt$	79
Figure 4-25: Sensitivity of the oscillation method (1mm channel).....	80
Figure 4-26: Air flow rate oscillation (0.5 mm channel)	81
Figure 4-27: Estimated net internal energy and the corresponding T_c oscillation (0.5 mm channel), ◆ Net internal energy change, ■ T_c	81
Figure 4-28: Total heat flux oscillation at the top and circumference surfaces (0.5 mm channel), ■ q'_{top} , △ q'_{cir} , * q'_{bot} , ○ $d\Delta E_{net}/dt$	82
Figure 4-29: Sensitivity of the oscillation method (0.5 mm channel).....	83
Figure 5-1: Layout of the experiment setup.....	84
Figure 5-2: Two heat flux probes a) held together by b) two aluminum brackets.....	85
Figure 5-3: Spherical blackbody furnace [47]	86
Figure 5-4: Effective emissivity of spherical cavities [48]	86
Figure 5-5: Rectangular cavity of the AKL-1297 furnace.....	88
Figure 5-6: Furnace door modification, a) outside view, b) inside view	88
Figure 5-7: Front plate, a) front view, b) side view, c) disassembled.....	89
Figure 5-8: Spectral transmissivity of sapphire window [53].....	89
Figure 5-9: Testing position of the sensors, a) outside view, b) inside view	90
Figure 5-10: Disc to parallel coaxial disc of unequal radius.....	91
Figure 5-11: Air flow rate signals (T2-c-1700), ◆ $\dot{m}=2$ g/s, □ $\dot{m}=7.9$ g/s.....	95
Figure 5-12: “Dirty” sensor temperature difference (T2-c-1700), ◆ $\dot{m}=2$ g/s, □ $\dot{m}=7.9$ g/s ..	96
Figure 5-13: Center and periphery temperatures (T2-c-1700), ■ T_c , ◇ T_p , a) $\dot{m}=2$ g/s, b) $\dot{m}=7.9$ g/s.....	97
Figure 5-14: RTD (T2-c-1700), ◆ $\dot{m}=2$ g/s, □ $\dot{m}=7.9$ g/s.....	98

Figure 5-15: Sensitivity for the RTD method, \square T1-c, \blacktriangle T2-c, \circ T3-c, a) $\dot{m}=2\text{g/s}$, b) $\dot{m}=7.9\text{ g/s}$	99
Figure 5-16: Air flow rate signals (T4-c-1700), \blacklozenge $\dot{m}=0.95\text{g/s}$, \square $\dot{m}=3.8\text{g/s}$	100
Figure 5-17: “Dirty” sensor temperature difference (T4-c-1700), \blacklozenge $\dot{m}=0.95\text{g/s}$, \square $\dot{m}=3.8\text{g/s}$	101
Figure 5-18: Center and periphery temperatures (T4-c-1700), \blacksquare T_c , \diamond T_p , a) $\dot{m}=0.95\text{g/s}$, b) $\dot{m}=3.8\text{ g/s}$	102
Figure 5-19: RTD (T4-c-1700), \blacklozenge $\dot{m}=0.95\text{g/s}$, \square $\dot{m}=3.8\text{g/s}$	103
Figure 5-20: Sensitivity for the RTD method, \square T4-c, \blacktriangle T5-c, a) $\dot{m}=0.95\text{g/s}$, b) $\dot{m}=3.8\text{ g/s}$	103
Figure 5-21: Effect of flow oscillation period on T_c oscillation, \diamond $P=40\text{s}$, \blacksquare $P=40\text{s}$, \square $P=200\text{s}$, \blacktriangle T_c at $\dot{m}=2\text{ g/s}$, \star T_c at $\dot{m}=7.9\text{ g/s}$	105
Figure 5-22: Air flow rate signal (T2-s-1700)	106
Figure 5-23: “Dirty” sensor temperature difference (T2-s-1700)	106
Figure 5-24: T_c oscillation (T2-s-1700)	107
Figure 5-25: Sensitivity for the oscillation method, \square T1-s, \blacktriangle T2-s, \circ T3-s.....	107
Figure 5-26: Air flow rate signal (T4-s-1700)	108
Figure 5-27: “Dirty” sensor temperature difference (T4-s-1700)	109
Figure 5-28: T_c oscillation (T4-s-1700)	109
Figure 5-29: Sensitivity for the oscillation method, \square T4-s, \blacktriangle T5-s.....	110
Figure 5-30: Sensitivity for “dirty” heat flux sensor, \diamond T2-c, \square T4-c	111
Figure 5-31: “Dirty” sensor temperature difference (T4-s-heating)	112
Figure 5-32: T_c oscillation (T4-s-heating).....	113
Figure 5-33: “Dirty” sensor temperature difference (T4-s-cooling)	113
Figure 5-34: T_c oscillation (T4-s-cooling)	114
Figure 5-35: Result after first step of the HPTD procedure (T4-s-1700).....	115
Figure 5-36: Estimated amplitude values, HPTD procedure, (T4-s-1700)	115
Figure 5-37: Result of the OPTD procedure (T4-s-1700).....	116
Figure 5-38: Result after first step of the CTD procedure (T4-s-1700).....	116
Figure 5-39: Estimated amplitude values, CTD procedure (T4-s-1700)	117
Figure 5-40: Result after first step of the HPTD procedure (T4-s-heating).....	117
Figure 5-41: Estimated amplitude values, HPTD procedure (T4-s-heating)	118
Figure 5-42: Result of OPTD procedure (T4-s-heating).....	118

Figure 5-43: Result after first step of the CTD procedure (T4-s-heating)	119
Figure 5-44: Estimated amplitude values, CTD procedure (T4-s-heating).....	119
Figure 5-45: Result after first step of the HPTD procedure d (T4-s-cooling).....	120
Figure 5-46: Estimated amplitude, HPTD procedure (T4-s-cooling)	120
Figure 5-47: Result of OPTD procedure (T4-s-cooling).....	121
Figure 5-48: Result after first step of the CTD procedure (T4-s-cooling).....	121
Figure 5-49: Estimated amplitude, CTD procedure (T4-s-cooling).....	121
Figure 6-1: “Clean” heat flux sensor surface a) before and b) after experiments	124
Figure 6-2: “Dirty” sensor surface a) before and b) after experiments	125
Figure 6-3: Correlation between the amplitude and RTD results, numerical results, a) $\dot{m}=2$ g/s, b) $\dot{m}=7.9$ g/s.....	127
Figure 6-4: Correlation between the amplitude and RTD results, experimental, \square T1-c & T1-s, \blacktriangle T2-c & T2-s, \circ T3-c & T3-s, a) $\dot{m}=2$ g/s, b) $\dot{m}=7.9$ g/s	128
Figure 6-5: Correlation between the amplitude and RTD results, numerical, a) $\dot{m}=0.95$ g/s, b) $\dot{m}=3.8$ g/s	129
Figure 6-6: Correlation between the amplitude and RTD results, experimental, \square T4-c & T4-s, \blacktriangle T5-c & T5-s, a) $\dot{m}=0.95$ g/s b) $\dot{m}=3.8$ g/s	130
Figure 6-7: Temperature contour at the sensing element (1mm channel, $\dot{m}=2$ g/s, 56.6kW/m^2)	131
Figure 6-8: Quadratic approximation of T_c (T4-s-heating).....	132
Figure 6-9: T_{dc} component of T_c (T4-s-heating).....	133
Figure 6-10: T_{ac} component of T_c (T4-s-heating).....	133

List of Tables

Table 3-1: Air flow rates for the two sensors.....	37
Table 4-1: Air inlet mass flow rates.....	53
Table 4-2: BFT and corresponding incident radiation heat flux.....	54
Table 4-3: Material properties of mineral wool.....	56
Table 4-4: Grid sensitivity test results.....	59
Table 5-1: Estimated view factors for each test.....	92
Table 5-2: Estimated percentage transmitted radiation at each testing temperature.....	93
Table 5-3: Estimated incident radiation heat flux for the “clean” sensor.....	93
Table 5-4: Configurations of the experiments and the corresponding codes.....	94
Table 6-1: Summary of the parameters in the conversion equations.....	123

Nomenclature

A	Dependent variable, K
A	Surface area, m ²
A_c	Amplitude of T_c oscillation, K
Bi	Biot number
Br	Brinkman number
c_p	Constant pressure specific heat capacity, J/kg·K
C_1, C_2	Constants for emissive power calculation
$C_{1\varepsilon}, C_{2\varepsilon}, C_\mu, C_2$	Constants for turbulence transport equations
$C_{RTD}, C_{A_c}, C_{1P}, C_{Dir}$	Constants for heat flux estimation
$dT_{1/2P}$	Half period temperature difference, K
dT_{1P}	One period temperature difference, K
$dT_{central}$	Central temperature difference, K
D_i, D_o	Inner and outer diameter of the annular channel, mm
$e_b, e_{b\lambda}$	Hemispherical spectral and total emissive power of a blackbody, W/m ²
E	Internal energy, J
E	Output voltage of a sensor, mV
F_{1-2}	View factor between surface A_1 and A_2
$F_{\lambda 1-\lambda 2}$	Fraction of the radiation within the wavelength range
G_k	Generation of turbulence kinetic energy
h	Sensible enthalpy, J
h	Heat transfer coefficient, W/m ² ·K
$h_1, h_2 (h_{top}, h_{cir})$	Heat transfer coefficients at the top and circumference sensor surface, W/m ² ·K
I_{inc}	Incident radiation intensity, W/m ²
k, k_{eff}	Thermal conductivity and effective thermal conductivity, W/m ² ·K

k	Turbulent kinetic energy
l	Characteristic length, m
m	Mass, kg
\dot{m}_1, \dot{m}_2	Minimum and maximum air flow rates, g/s
\dot{m}_0, \dot{m}_A	Mean air flow rate and amplitude of air flow rate oscillation, g/s
Ma, Ma_t	Mach number and turbulent Mach number
\bar{n}	Refractive index of the medium
N	Number of thermocouple junction pairs
Nu	Nusselt number
p, \bar{p}, p'	Instantaneous, mean and fluctuating pressure, Pa
P	Period of air flow rate oscillation, s
Pr, Pr_t	Prandtl number and turbulent Prandtl number
q	Heat transfer rate, W
$q_{cond}, q_{conv}, q_{rad}$	Heat transfer rate through conduction, convection and radiation, W
q'', q''_0	Heat flux density and amplitude of heat flux oscillation, kW/m ²
q''_{inc}, q''_a	Incident and absorbed radiation heat flux, kW/m ²
q''_{mes}	Measured heat flux, kW/m ²
q''_{tot}	Total heat flux, kW/m ²
$q''_{initial}$	Initial heat flux, kW/m ²
R_s	Specific gas constant, (8.314 J/K·mol)
Re	Reynolds number
\bar{s}	Directional vector
S	Surface to surface distance, m
S	Sutherland constant, (110.56 K)
S_A	Area of the surface, m ²
S_k	Heat source term in energy equation
t	Time, s
Δt	Time interval for temperature sampling, s
T, \bar{T}, T'	Instantaneous, mean and fluctuating temperature, K

T_c, T_p	Temperature at the center and periphery of the bottom sensor surface, K
T_w, T_f	Temperature at the surface, and of the fluid, K
T_{amb}, T_{ac}, T_{dc}	Three components contained in the oscillating sensor temperature, K
T_{env}	Environment temperature, K
T_{top}, T_{cir}	Temperature at the top and circumference sensor surfaces, K
T_1, T_2	Upper and lower steady state temperature under \dot{m}_1 and \dot{m}_2 , K
u_i, \bar{u}_i, u_i'	Instantaneous, mean and fluctuating velocity components in i direction, m/s
U	Velocity of the fluid, m/s
U_o	Axial mean velocity at the exit of the annular channel, m/s
U_m	Volumetric-mean axial velocity, m/s
X	Sensitivity of the sensor, K/(kW/m ²) or mV/(kW/m ²)
X_{RTD}, X_{A_c}	Sensitivity for the RTD method and oscillation method, K/(kW/m ²)
X_T	Thermoelectric sensitivity, mV/K
Y_j	Mass fraction of species j
Y_M	Contribution of the fluctuation dilatation in compressible turbulence

Greek letters

α	Absorptivity
α	Diffusivity, m ² /s
γ	Dimensionless adiabatic coefficient of the fluid
δ	Thickness of the sensing disc, mm
δ_{ij}	Kronechker delta
ε	Emissivity
ε	Effusivity, J/m ² ·K·t ^{1/2}
ε	Rate of dissipation of turbulent kinetic energy, m ² /s ³
θ_1, θ_2	Relative angles between surface A ₁ and A ₂
λ	Wavelength of light, μ m
μ, μ_t, μ_0	Fluid viscosity, turbulent viscosity and reference viscosity, kg/m·s
μ	Diffusion distance, m/rad ^{1/2}

ρ	Density, kg/m ³
σ	Stefan-Boltzmann constant ($5.672 \cdot 10^{-8}$ W/m ² ·K ⁴)
τ	Time constant of the heat flux sensor, s
τ, τ_{eff}	Stress and effective stress, Pa
ν	Kinematic fluid viscosity, m ² /s
ω	Angular velocity, rad/s
Θ	Characteristic radial temperature difference, K
Ω	Solid angle

Acronyms

HPTD	Half Period Temperature Difference
OPTD	One Period Temperature Difference
BFT	Back Flow Temperature
CTD	Central Temperature Difference
CFD	Computational Fluid Dynamics
CRZ	Center Recirculation Zone
DO	Discrete Ordinates
DTRM	Discrete Transfer Radiation Model
HPCVL	High Performance Computing Virtual Laboratory
RANS	Reynolds-averaged Navier-Stokes
RSM	Reynolds Stress Transport Models
RTD	Radial Temperature Difference
S2S	Surface to surface
SLM	Standard Liter per Minute
UDF	User Defined Function

Chapter 1 Introduction

1.1 Background

A coal-fired power plant boiler is usually designed for a specific type of coal [1]. However, due to mine closures, government regulations, market forces, etc, fuel change sometimes is unavoidable [2]. One important issue often associated with fuel variation and fuel mixing is boiler fouling. Although great improvements have been made in understanding the phenomenon, slagging and fouling still pose a great threat to the boiler efficiency when there is a fuel change. The definition of slagging and fouling varies with the source. Valero, et al [1], defined slagging as the ash deposits at the radiation region and fouling as at the convection region, while the terms were defined as solidified ash deposit and powdered ash deposit respectively in [3]. To avoid confusion, “fouling” is used to represent all types of ash deposits in the present report.

Deposit formation can be very complex and different for each power station. Many studies have been done in the past to investigate the relationship between the fouling condition and the type of coal used [3, 4], while some other studies evaluated the economic cost due to fouling in the boiler [2, 5]. More recently, following the trend of biomass and biomass-coal mixture firing, researchers have started to pay attention to the impact on ash fouling conditions caused by this new family of fuels [6-10]. Most of the results showed that biomass firing or biomass-coal mixture firing generally cause more severe ash fouling problem.

In a typical coal-fired boiler, on-load ash deposit removal is done by sootblowers that blow superheated steam, air or water onto the deposit layer. Number and location of these cleaning devices are customized for the each boiler to achieve effective deposit removal. The standard sootblowing schedule is determined by preset sequences, and is adjusted in accordance to initial assessments and operating experience.

However, when there is a significant change in fuel, the fouling pattern variation may render the preset sootblowing schedule ineffective. When this happens, sootblowing could fail to remove

ash deposits and stubborn deposits could build-up which disturbs the energy layout assumed in the design. In extreme cases, reduced efficiency and losses of availability also result from massive accumulation and shedding of deposits [1]. On the other hand, excess sootblowing will increase the operation cost due to expenditure of power and increased gas losses, and it can also cause damage to the water tube and therefore reduce the operation period of a boiler.

To tackle the problem, the development of fouling monitoring systems has started since the beginning of 1980s. The measurement of locally absorbed heat fluxes soon became the most widely used method [1]. The heat flux monitoring concept was established based on the impact of ash deposits on the heat transfer rate into the water tube due to its low thermal conductivity. Each heat flux sensor can provide a direct on-line assessment of local ash deposit condition. An ash monitoring system is basically a group of specially designed heat flux meters deployed inside the boilers as illustrated in [11-13]. The system can provide an assessment of overall fouling condition and the distribution of the deposits if the number of heat flux meters deployed is large enough. As a result, the sootblowing operation can be determined according to the real-time ash fouling condition estimated by the monitoring system.

Among the previously developed systems, one incorporates a “clean” heat flux sensor as opposed to the conventional “dirty” heat flux sensor. In such system, the “dirty” sensors are the traditional heat flux sensors that allow ash to deposit and hence measure the amount of heat flux received by the water tube. The additional “clean” sensors in the system are intended to measure the available radiation heat flux in the boiler. The sensing surface of a “clean” sensor is kept free of ash by the air screen surrounding the surface of the sensing element. By comparing the results of the two types of sensors, the system provides an estimation of ash fouling condition that takes into account the available radiation heat flux variation. Given the situation of the current project in which different biomass material and fuel mixture ratio will be tested in the boiler, this type of monitoring system is considered more suitable because it is able to identify the source of the absorbed heat flux change and hence provides more accurate ash fouling estimation.

1.2 Project Scope

The main objective of the project is to develop an ash monitoring system prototype that consists of one “clean” heat flux sensor and one “dirty” heat flux sensor. The focus of the present work is on the design and improvement of the “clean” heat flux sensor. The basis of the current design is the sensor developed by Afgan, et al [14, 15]. Based on the requirements of this project, the structure of the sensor is modified, and attempts are made to improve the sensor performance. The performances of the two measurement methods and their relationships with various parameters of the “clean” heat flux sensor are studied numerically and experimentally. The numerical results and experimental results are analyzed and discussed, and the performances of the two measurements methods are also compared.

Chapter 2 Literature Review

Measuring temperature alone in a thermodynamic system, such as a furnace boiler, is not enough to understand the heat transfer and thermal efficiencies of the system. Most of the time, accurate measurement of heat flux density inside the system is also necessary. Arai, et al [16] summarized heat flux measurement concepts into two categories: indirect measurements, made by calculating heat transfer rates using fundamental theories together with measurements of temperature and thermo physical properties, and direct measurements, using non-perturbing heat flux sensors placed in the thermal field.

Heat flux estimation using the first concept is generally regarded as inverse heat transfer problem where the heat flux or temperature histories at the surface of a solid are determined from transient temperature measurements at the surface or interior locations. It is normally used where direct heat flux measurement devices can not be deployed, such as the surface of a space shuttle [17]. However, solving an inverse heat conduction problem is relatively difficult and requires good knowledge of the properties of the material and high accuracy temperature measurements. Therefore, in most situations, heat flux sensors are used to provide direct measurements of surface heat fluxes.

Heat flux sensors can be treated as small-scale thermal systems, in which the relationship between the surface heat flux and the temperature response of the sensor is obtained before deployment by solving the direct heat transfer problem analytically or numerically, and eventually, by experimental calibration. The temperature response of the sensor is usually referred to as the dependent variable A of the sensor and the relationship between the dependent variable and the measured heat flux q''_{mes} is often referred to as the sensitivity of the sensor X . Although the actual sensitivity of a heat flux sensor is always determined through experiment calibration, analytical or numerical results can reveal the relationships between the sensor

parameters and the performance providing guidance in sensor design. The responsivity or sensitivity of a sensor can be defined as [17]:

$$X = \frac{dA}{dq''_{mes}} \quad 2-1$$

However, when designing heat flux sensors, the dependent variables are often chosen to vary linearly with the measured heat flux. Therefore, the sensitivity of a sensor can often be simplified to:

$$X = \frac{A}{q''_{mes}} \quad 2-2$$

Once the sensor is installed in the target system, heat flux measurement can be obtained directly by combining the readings of the dependent variable and the value of sensitivity obtained previously:

$$q''_{mes} = \frac{1}{X} \times A \quad 2-3$$

In general, sensors with higher sensitivity are desired [17].

There are roughly three types of heat flux sensors: contact type sensor, thermal radiative sensors, and convective heat flux sensors [18]. Although numerous variations in sensor structures and measurement techniques were developed to satisfy their specific purposes, the principle of heat flux measurement involves the three fundamental forms of heat transfer: conduction, convection and radiation.

The following section gives a brief review of the three forms of heat transfer. Basic heat flux measurement concepts and sensors as well as sensors used for the ash monitoring purpose are introduced. Details of the “clean” heat flux sensor that initiates the present work are also included in this chapter.

2.1 Heat Transfer

Heat transfer, q with a unit of (J/s=W), denotes the rate at which heat is being transferred, and heat flux is heat transfer per unit of area, which is represented by q'' with a unit of (W/m²) [19]. The first law of thermodynamics states that the overall energy transferred to and from a system is conserved. This includes all three forms of heat transfer: convection, radiation and conduction, across the system boundary as illustrated in Figure 2-1

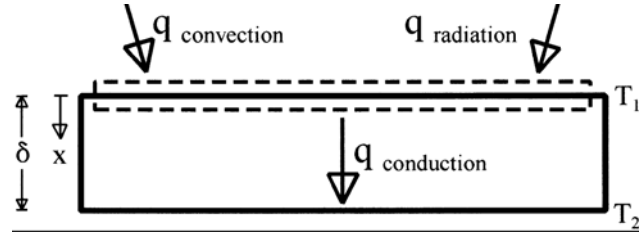


Figure 2-1: Energy balance at a system boundary [20]

In this case, heat is transferred into the control volume through convection and radiation while it leaves the control volume through conduction. The transient energy balance of the system in the control volume can be expressed as:

$$mc_p \frac{\partial T}{\partial t} = q_{net} = q_{conv} + q_{rad} - q_{cond} \quad 2-4$$

where m is the mass of the system in the control volume, c_p is the specific heat of the material and q_{net} is the rate of net heat absorbed by the control volume. The thermal capacitance (mc_p) of the control volume is responsible for the temperature time response of the system when subjected to a change in incoming heat flux. When the system is in thermal equilibrium, $\frac{\partial T}{\partial t} = 0$, and the three

modes of heat transfer are balanced as:

$$q_{cond} = q_{conv} + q_{rad} \quad 2-5$$

Therefore, in principle, the total heat flux imposed on the surface can be estimated by calculating the conductive heat transferred through the system.

2.1.1 Momentum and Convection Heat Transfer

Heat convection is the term applied to the process involved when energy is transferred between a surface and a fluid flowing over it as a result of a difference between the temperatures of the surface and the fluid. Fluid motion greatly complicates the analysis by coupling the heat transfer problem with fluid mechanics, particularly when the flow is turbulent. Therefore, a convection heat transfer coefficient is introduced to account for all the fluid flow effects.

$$q''_{conv} = h(T_w - T_f) \quad 2-6$$

The above equation is often referred to as Newton's Law of Convection, where T_w is the temperature at the surface and T_f is the fluid temperature and h is the heat transfer coefficient. The heat transfer coefficient is affected not only by the properties of the fluid, but also the fluid flow conditions and surface conditions.

Due to their complexity, analytical and experimental studies of fluid flow and convection problems often employ dimensional analysis which can reduce the number of variables that affect a given physical phenomenon. Several dimensionless parameters that are considered related to the present work are introduced below.

The most commonly used dimensionless parameter is Reynolds number, which is expressed as:

$$Re = \frac{\rho U l}{\mu} \quad 2-7$$

where l is the characteristic size of the surface, ρ , U , and μ are fluid density velocity magnitude and viscosity, respectively. Reynolds number indicates ratio of the inertia forces magnitude to the viscous forces magnitude in the flow. When the Reynolds number is low, the flow stays laminar, while for high Reynolds numbers the flow tends to become turbulent. As shown in Figure 2-2, the air screen surrounding the "clean" heat flux sensor studied in the present work is essentially an annular air jet.

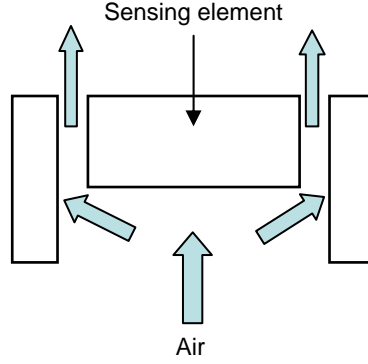


Figure 2-2: Air flow in “clean” heat flux sensor

Reynolds numbers for annular jet are defined differently by different authors. Warda, et al [21] defined the Reynolds number of an annular jet as:

$$\text{Re} = \frac{\rho U_o D_o}{\mu} \quad 2-8$$

where D_o is the outer diameter of the annular channel, U_o is the axial mean velocity at the exit of the annular jet. Chattopadhyay [22], Sheen, et al [23] and Vanierschot, et al [24] defined the Reynolds number of the annular jet as:

$$\text{Re} = \frac{\rho U_m (D_o - D_i)}{\mu} \quad 2-9$$

where D_i is the inner diameter of the annular channel and U_m is the volumetric-mean axial velocity, calculated as:

$$U_m = \frac{\dot{V}}{\pi(D_o^2 - D_i^2)/4} \quad 2-10$$

where \dot{V} is the volume flow rate.

Prandtl number is a ratio of the momentum and thermal diffusivity:

$$\text{Pr} = \frac{\nu}{\alpha} \quad 2-11$$

where $\nu = \frac{\mu}{\rho}$ is the kinematic viscosity of the fluid and $\alpha = \frac{k}{\rho c_p}$ is the thermal diffusivity of the

fluid. For air, Prandtl number is approximately 0.7 to 0.8.

Nusselt number represents the ratio of the convective heat transfer rate to the heat transfer rate that would exist when the flow is stagnate and heat is transferred by conduction only. It is defined as:

$$Nu = \frac{hl}{k} \quad 2-12$$

For flow with high velocities, the velocity of the flow can be represented with Mach number which is defined as

$$Ma = \frac{U_\infty}{a} = \frac{U_\infty}{\sqrt{\gamma R_s T_f}} \quad 2-13$$

where, a is the speed of sound, U_∞ is the flow velocity, γ is the dimensionless adiabatic coefficient of the fluid and R_s is the specific gas constant of the fluid. When Mach number is greater than 0.5, compressibility needs to be taken into consideration.

Another dimensionless parameter that is important in high velocity convection problems is Brinkman number. It is a measure of viscous heating when the fluid is flowing over a surface and is defined as:

$$Br = \frac{\nu U^2}{k(T_w - T_f)} \quad 2-14$$

Viscous heating becomes important when Brinkman number is close to or greater than one [25].

In order to estimate the convective heat transfer rates directly, the distributions of three variables through the flow fields have to be determined: pressure P , velocities u_i and temperature T . The variables can be estimated by solving the three governing equations of a fluid flow: continuity equation, Navier-Stokes equation and energy equation simultaneously. Under the axisymmetrical

assumption, the governing equations of an incompressible steady laminar flow can be expressed in the following forms [26]:

Continuity equation:

$$\frac{1}{r} \frac{\partial}{\partial r} (ru_r) + \frac{\partial u_z}{\partial z} = 0 \quad 2-15$$

Momentum Equation:

$$\begin{aligned} u_r \frac{\partial u_r}{\partial r} + u_z \frac{\partial u_r}{\partial z} &= -\frac{1}{\rho} \frac{\partial p}{\partial r} + \nu \left[\frac{1}{r} \frac{\partial}{\partial r} \left(r \frac{\partial u_r}{\partial r} \right) + \frac{\partial^2 u_r}{\partial z^2} \right] \\ u_r \frac{\partial u_z}{\partial r} + u_z \frac{\partial u_z}{\partial z} &= -\frac{1}{\rho} \frac{\partial p}{\partial z} + \nu \left[\frac{1}{r} \frac{\partial}{\partial r} \left(r \frac{\partial u_z}{\partial r} \right) + \frac{\partial^2 u_z}{\partial z^2} \right] \end{aligned} \quad 2-16$$

Energy equation:

$$\begin{aligned} u_r \frac{\partial T}{\partial r} + u_z \frac{\partial T}{\partial z} &= \left(\frac{k}{\rho c_p} \right) \left(\frac{\partial^2 T}{\partial z^2} + \frac{1}{r} \frac{\partial}{\partial r} \left(r \frac{\partial T}{\partial r} \right) \right) + \left(\frac{\mu}{\rho c_p} \right) \Phi \\ \Phi &= 2 \left[\left(\frac{\partial u_z}{\partial z} \right)^2 + \left(\frac{\partial u_r}{\partial r} \right)^2 \right] + \left[\left(\frac{\partial u_r}{\partial z} \right) + \left(\frac{\partial u_z}{\partial r} \right) \right]^2 \end{aligned} \quad 2-17$$

However, the majority of flows encountered in practice are turbulent. In turbulent flows, even when the mean flow is steady, the flow variables fluctuate randomly with time due to the superposition of the turbulent eddies on the mean flow. The difference in flow velocity between a steady laminar flow and a steady turbulent flow can be seen in Figure 2-3.

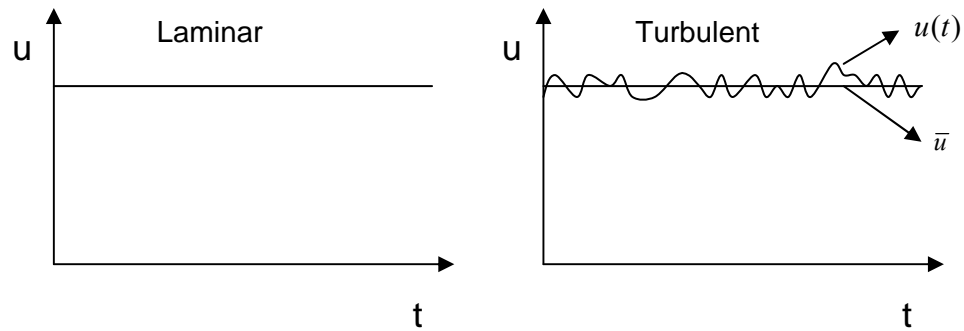


Figure 2-3: Steady laminar and turbulent flow velocities

The mean values of the variables in a steady turbulent flow can be defined as the time average of the actual variables over a time interval. These instantaneous values of the flow variables can be decomposed into the mean and fluctuating components:

$$\begin{aligned} u_i &= \bar{u}_i + u_i' \\ P &= \bar{P} + P' \\ T &= \bar{T} + T' \end{aligned} \tag{2-18}$$

Mean momentum, heat and mass transfer are now governed by Reynolds average equations:

Continuity equation:

$$\frac{1}{r} \frac{\partial}{\partial r} (r \bar{u}_r) + \frac{\partial \bar{u}_z}{\partial z} = 0 \tag{2-19}$$

Momentum Equation:

$$\bar{u}_r \frac{\partial \bar{u}_r}{\partial r} + \bar{u}_z \frac{\partial \bar{u}_r}{\partial z} = -\frac{1}{\rho} \frac{\partial \bar{p}}{\partial r} + \frac{\nu}{r} \frac{\partial}{\partial r} \left(r \frac{\partial \bar{u}_r}{\partial r} \right) - \frac{1}{r} \frac{\partial}{\partial r} (r \overline{u_r' u_z'}) \tag{2-20}$$

Energy equation:

$$\bar{u}_z \frac{\partial \bar{T}}{\partial z} + \bar{u}_r \frac{\partial \bar{T}}{\partial r} = \left(\frac{k}{\rho c_p} \right) \frac{1}{r} \frac{\partial}{\partial r} \left(r \frac{\partial \bar{T}}{\partial r} \right) - \frac{1}{r} \frac{\partial}{\partial r} (r \overline{u_r' T'}) \tag{2-21}$$

In the original work [15], heat transfer coefficient within the annular channel was handled by Roisen-Petuhov expression, and the heat transfer coefficient at the top surface was estimated based on the radial velocity measured in [14]. However, the calculation procedure and the values of the heat transfer coefficients were not reported.

2.1.2 Radiation Heat Transfer

As described in [27], electromagnetic radiation is continuously emitted from all substances because of the molecular and atomic agitation associated with their internal energy. Thermal radiation is especially important in high temperature applications due to the manner in which it depends on temperature. For conduction and convection, energy transfer between two locations

depends on their temperature difference to approximately the first power. However, thermal radiation energy transfer between two bodies depends on the difference between fourth powers of absolute temperatures. Consequently, radiation contributes substantially to energy transfer in furnaces, combustion chambers etc.

The basic radiative heat transfer calculation uses the concept of blackbody, an ideal absorber that absorbs all the incident radiation at all wavelengths and incident angles. In thermal equilibrium, the body temperature remains constant, and the energy absorbed by the body is equal to the energy emitted by the body. Hence, blackbody also defines the maximum energy emission corresponding to the body temperature. The hemispherical spectral emissive power of a black body can be expressed as:

$$\frac{e_{\lambda b}(\lambda, T)}{T^5} = \frac{2\pi C_1}{(\lambda T)^5 (e^{C_2/\lambda T} - 1)} \quad 2-22$$

where T is the temperature of the blackbody, λ is the wavelength of the radiation, and $C_1 = 5.96 \cdot 10^7$, $C_2 = 14387.75$ are two constants.

The hemispherical total emissive power of a blackbody radiating into vacuum is defined as

$$e_b = \int_0^\infty e_{\lambda b}(\lambda) d\lambda = \sigma T^4 \quad 2-23$$

where $\sigma = 5.6704 \times 10^{-8} \text{ W}/(\text{m}^2 \text{ K}^4)$ is the Stefan-Boltzmann constant.

The fraction of the total emissive power emitted in a wavelength band can be calculated as:

$$F_{\lambda_1 \rightarrow \lambda_2} = \frac{1}{\sigma} \left[\int_0^{\lambda_2} \frac{e_{\lambda b}(\lambda)}{T^5} d(\lambda T) - \int_0^{\lambda_1} \frac{e_{\lambda b}(\lambda)}{T^5} d(\lambda T) \right] \quad 2-24$$

where λ_1 and λ_2 represent the upper and lower limits of the wavelength band.

However, real body does not absorb all the incident radiation and therefore its emissive power is also a fraction of the blackbody emission. The ratio between the radiation energy emitted from a real body and that of a blackbody is specified by the emissivity ε . Emissivity depends on factors such as body temperature, wavelength and angle of emission. The absorptivity α is defined as the

fraction of the absorbed incident radiation on a body. Absorptivity has additional complexities because directional and spectral characteristics of the incident radiation must be included. However, emissivity and absorptivity can be considered equivalent when the incident radiation is independent of angle and has a spectral distribution proportional to that of a black body. For a heat flux sensor deployed into a boiler, this requirement is generally satisfied. Therefore, the absorptivity of the sensor surface can be regarded the same as its emissivity.

Another important parameter in radiation heat transfer is the view factor. View factor defines the portion of the energy emitted by one object (A_1 in Figure 2-4) reaches the other object (A_2 in Figure 2-4).

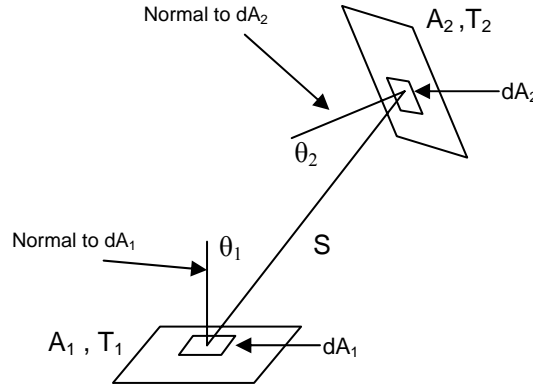


Figure 2-4: Relative orientation between two surfaces in space

The view factor can be calculated as

$$F_{1-2} = \frac{1}{A_1} \int_{A_1} \int_{A_2} \frac{\cos(\theta_1) \cos(\theta_2)}{\pi S^2} dA_1 dA_2 \quad 2-25$$

where S is the distance between dA_1 and dA_2 , θ_1 and θ_2 are the angles between line S and the surface normal of dA_1 and dA_2 .

To estimate the actual incident radiation on the sensor surface, the factors mentioned above have to be taken into consideration. The incident radiation on the surface of the sensor can be calculated as:

$$q_{inc}'' = F_{sur-rad} F_{\lambda_1-\lambda_2} \varepsilon_{rad} \sigma T_{rad}^4 \quad 2-26$$

where ε_{rad} is the emissivity of the radiation source, T_{rad} is the temperature of the radiation source, $sur-rad$ denotes the view factor of the radiation source respect to the sensor surface. The above expression is used to estimate the incident radiation in the experiment. The actual calculation procedure is outlined in Chapter 5.

2.1.3 Conduction Heat Transfer

When heat is transferred from one part of a body to another part or from one body to another which is in contact with it, the process is generally referred to as heat conduction. The basic equation for heat condition analysis is Fourier's law, which is established according to experimental observation [28]. Heat flux can be related to the temperature distribution inside the body as:

$$q_n'' = -k_n \frac{\partial T}{\partial n} \quad 2-27$$

where heat flux q_n'' is the heat transfer rate in the n direction per unit area perpendicular to the direction of the heat flow, k_n is the thermal conductivity in the direction n . When there is no heat production in the system, the general equation of heat conduction in the Cartesian coordinates is:

$$\rho c \frac{\partial T}{\partial t} = \frac{\partial}{\partial x} \left(k \frac{\partial T}{\partial x} \right) + \frac{\partial}{\partial y} \left(k \frac{\partial T}{\partial y} \right) + \frac{\partial}{\partial z} \left(k \frac{\partial T}{\partial z} \right) \quad 2-28$$

For a material with homogeneous thermal conductivity and specific heat, Equation 2-28 becomes:

$$\frac{\partial T}{\partial t} = \alpha \left(\frac{\partial^2 T}{\partial x^2} + \frac{\partial^2 T}{\partial y^2} + \frac{\partial^2 T}{\partial z^2} \right) \quad 2-29$$

where $\alpha = \frac{k}{\rho c_p}$ is the thermal diffusivity of the body.

The temperature distribution inside the solid can be estimated using the above equation when the boundary conditions and initial condition are provided. The three basic boundary conditions are: constant surface temperature, constant surface heat flux, and a prescribed relationship between the surface heat flux and the surface temperature. For a one-dimensional transient condition in a semi-infinite solid, the first two types of boundary conditions can be expressed in the following forms:

$$T(0,t) = T_s(t) \quad 2-30$$

$$-k \frac{\partial T(0,t)}{\partial x} = q''_s(t) \quad 2-31$$

where T_s and q''_s represent constant temperature and heat flux at the boundary. The third type of boundary can be either a convection boundary condition or radiation boundary condition as shown in Equation 2-32 and 2-33

$$-k \frac{\partial T(0,t)}{\partial x} = h[T(0,t) - T_f] \quad 2-32$$

$$-k \frac{\partial T(0,t)}{\partial x} = \varepsilon \sigma [T_{rad}^4 - T^4(0,t)] \quad 2-33$$

The solution of the conduction equation can become complicated when combined boundary conditions (radiation and convection) are applied and multiple multidimensional effects are present [29].

Another type of boundary condition often encountered in practice is harmonic surface temperature or heat flux such as the one given in Equation 2-34 [30]:

$$-k \frac{\partial T}{\partial x}(0,t) = q''_s(0,t) = \frac{q''_0}{2} (1 + \cos(\omega t)) \quad 2-34$$

The above equation describes a sinusoidal oscillating heat flux with an amplitude of $q''_0/2$ and a frequency of $\omega/2\pi$ imposing on the surface. For a semi-infinite solid with such boundary condition, the steady state temperature inside the body can be divided into three components:

$$T(x, t) = T_{amb} + T_{dc}(x) + T_{ac}(x, t) \quad 2-35$$

where T_{amb} is the ambient temperature surrounding the body, T_{dc} is the time independent component when the temperature stabilizes, and T_{ac} is the time dependent component that oscillates with the surface heat flux. T_{dc} is determined by the heat capacity of the body while T_{ac} can be related to the surface heat flux amplitude in terms of a function of time t , and distance from the surface x [30]:

$$T_{ac}(x, t) = \frac{q''_0}{2} \frac{e^{-x/\mu}}{\varepsilon\sqrt{\omega}} \cos\left[\frac{x}{\mu} - \omega t + \frac{\pi}{4}\right] \quad 2-36$$

where ε is the thermal effusivity of the material:

$$\varepsilon = \frac{k}{\sqrt{\alpha}} = \sqrt{\rho c_p k} \quad 2-37$$

and μ is the diffusion distance of the material

$$\mu = \sqrt{\frac{2\alpha}{\omega}} = \sqrt{\frac{k}{\rho c_p \omega}} \quad 2-38$$

Several conclusions can be drawn by observing Equation 2-36. First, the temperature in the body oscillates with the same frequency as the heat flux oscillation at the surface. Second, the amplitude of temperature oscillation decays exponentially with distance x . Third, the amplitude of temperature oscillation decays exponentially with the square root of ω , which indicates a more rapid damping effect for heat flux oscillation with higher frequencies. Forth, the phase angle of the temperature oscillation increases as the depth x increases with the minimum phase angle of $\pi/4$ occurring at the surface where $x=0$ [28]. This expression serves as the basis of the heat flux measuring method proposed in the present work.

2.2 Heat Flux Measurement

Most methods for heat flux measurement are based on temperature difference measurements on the surface or close to the surface of the sensing element made of some solid material. Different heat flux sensors may vary in how the temperature difference is measured, the dimensions and the material of the sensing element, and the structure of the sensor. Nevertheless, in terms of measuring concept, there are generally two types as summarized in [20]: sensors based on spatial temperature gradient and sensors based on temporal temperature difference.

2.2.1 Measurement Based On Spatial Temperature Gradient

One-dimensional planar sensor is the simplest heat flux sensor concept as illustrated in Figure 2-5. The sensor is essentially a thermal resistance layer with thickness δ , and the thermocouples are placed at the two sides of the sensing plate

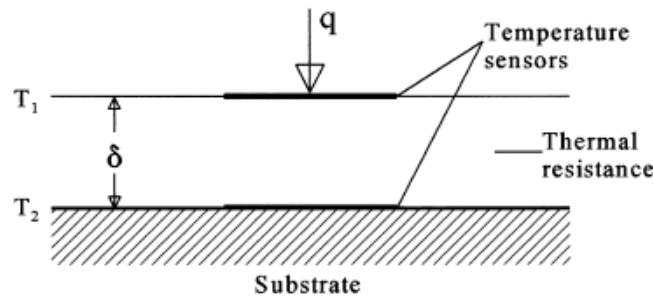


Figure 2-5: One-dimensional planar sensor concept [20]

Under a steady incident heat flux, heat conduction through the thin plate can be assumed as one-dimensional. Therefore, the heat flux can be estimated directly from the temperature difference by utilizing Fourier's Law (Equation 2-27) if the thickness and the thermal conductivity of the plate are known.

$$q'' = k \frac{T_1 - T_2}{\delta} \quad 2-39$$

where δ is the thickness of the sensing element, and T_1 and T_2 are the temperatures at the top and bottom surfaces of the element. The most commonly used temperature measurement device is thermocouple. For one dimension planar sensors, thermocouples can be connected in series to form a thermopile to amplify the voltage output under a given temperature difference. In this case, the voltage output becomes:

$$E = NX_T(T_1 - T_2) \quad 2-40$$

where, N represents the number of thermocouple junction pairs, and X_T is the thermoelectric sensitivity of the materials. The sensitivity of the sensor can be expressed as:

$$X = \frac{E}{q''} = \frac{NX_T\delta}{k} \quad 2-41$$

The time constant τ of this type of sensor, which indicates the response speed of the sensor when subject to a step change heat flux, is related to the thickness and the diffusivity of the sensing element by the following function [20]:

$$\tau = \frac{3}{2} \frac{\delta^2}{\alpha} \quad 2-42$$

The first sensor that utilizes this thermal pile technique is the Schmidt-Boelter heat flux sensor as shown in Figure 2-6.

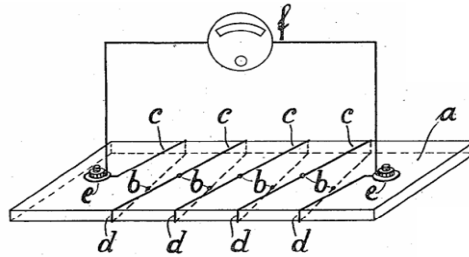


Figure 2-6: Schmidt heat flux sensor [18]

The sensing element is wrapped by a series of thermocouples with their junctions on the top and bottom of the element. The element is mounted on the gage body as shown in Figure 2-7.

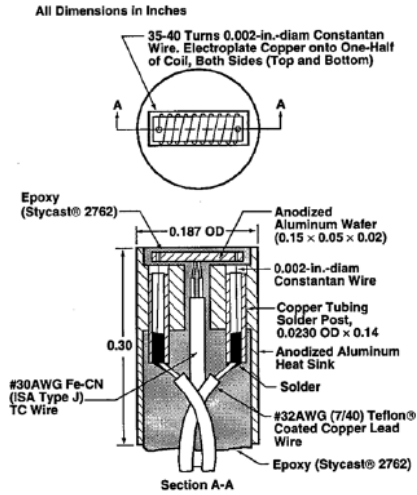


Figure 2-7: Section and top view of Schmidt-Boelter gage [29]

Besides the one-dimensional planar concept, some other sensors are made based on the circular foil gage, also known as Gardon gage that was designed by Robert Gardon [31] mainly to measure radiation heat flux. Its sensing element consists of a thin foil made of constantan, and a hollow cylinder, usually made of copper, which is attached underneath the foil as shown in Figure 2-8. When subject to a uniform radiation heat source, the majority of the absorbed heat flux is conducted radially towards the copper body. A copper-constantan thermocouple is used to measure the radial temperature difference. The copper wire is attached to the cylinder body and the constantan wire is attached to the foil at the center as illustrated in Figure 2-8

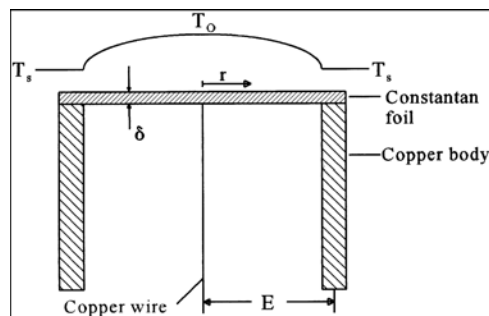


Figure 2-8: Gardon type heat flux sensor [29]

It was recognized that the radial temperature difference is not a linear function of the radiation heat flux unless the thermal conductivity of the foil material is not temperature dependent [31]. However, the design utilized the nonlinear output of copper-constantan thermocouples to offset

the nonlinearity of the radial temperature difference. As a result, the output *e.m.f.* is linearly related to the incident radiation heat flux.

For a uniform heat flux incoming radiation, the radial temperature difference is proportional to the heat flux as expressed in Equation 2-43

$$q'' = \frac{4k\delta}{R^2} (T_c - T_p) \quad 2-43$$

where, δ is the thickness of the foil, and R is the active radius of the foil, T_c is the temperature at the center of the foil and T_p is the temperature at the periphery of the foil. For this type of sensor the time constant τ is defined at the disc center ($r=0$) as [16]:

$$\tau_{r=0} = \frac{R^2}{4\alpha} \quad 2-44$$

Notice that the above expression does not include the effect of the thickness of the sensing element. This is because the thickness of the foil is small enough so that the radial heat transfer can be considered one dimensional. With a thickness of 20 μ m, it takes 10s for the sensor to reach 98% of its steady state condition when subjected to a step change heat flux [16].

Gardon gage becomes inaccurate when convection heat transfer is significant. Convection can cause distortion of the temperature profile in the foil from the assumed radial symmetric, parabolic profile of radiation. Therefore, the radius of the sensing disc is often kept small to ensure uniform radial temperature difference when convection heat transfer is significant.

2.2.2 Measurement Based On Temporal Temperature Difference

Heat flux at the surface can also be measured from the transient perspective. One example is slug calorimeter. The measuring concept of slug calorimeter is based on the lumped capacitance assumption that the temperature throughout the sensor body is spatially uniform. The validity of the assumption is determined by Biot number if the main heat transfer form is convection. Biot number is defined as

$$Bi = \frac{hl}{k} \quad 2-45$$

where k is the conductivity of sensing element, l is the characteristic length of the element and h is the heat transfer coefficient at the surface. The assumption of negligible internal resistance is valid when the Biot number is less than 0.1. This implies the sensing element should have a large thermal conductivity. Figure 2-9 shows a slug calorimeter schematic. The sensing element is insulated all around except at the top surface A.

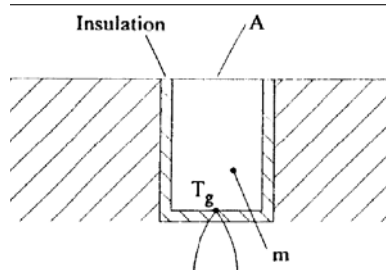


Figure 2-9: Slug calorimeter schematic [29]

Heat flux absorbed at surface A is kept in the sensing element and causes the temperature of the element to increase. The surface heat flux is related to the temperature change of the sensor by:

$$q'' = c_p \frac{m}{S_A} \frac{\partial T}{\partial t} \quad 2-46$$

where m is the mass of the calorimeter, S_A is the area of surface A. According to the type of incoming heat flux, the transient temperature change behaves differently. When the heat flux is mainly due to convection with a uniform heat transfer coefficient, the temperature change can be expressed as:

$$T(t) - T_\infty = (T_i - T_\infty) e^{-t/\tau} \quad 2-47$$

where T_i and T_∞ are the initial and final temperature, τ is the time constant of the sensor which is related to the heat transfer coefficient and the sensing element by:

$$\tau = \frac{mc_p}{hA} \quad 2-48$$

The time constant can be found from the temperature response of the system, which can then be used to quantify h .

If the surface of a semi-infinite body is subject to an incoming heat flux, the surface temperature alone can be used to estimate the heat flux. For short enough times and sufficiently thick material, heat transfer into the body can be assumed as one-dimensional and that the thermal effects do not reach the back surface of the material. Then, Equation 2-29 is reduced to the one-dimensional, semi-infinite solution, which is simple to implement. Cook, et al [32] developed a conversion formula based on uniformly sampled surface temperature data:

$$q''(t_N) = \frac{2\sqrt{k\rho c_p}}{\pi\Delta t} \sum_{j=1}^N \frac{T_j - T_{j-1}}{\sqrt{N-j} + \sqrt{N+1-j}} \quad 2-49$$

where $q''(t_N)$ is the heat flux at time $t_N = N\Delta t$, Δt is the time interval for temperature sampling, N represents the total number of temperature sample, and j is the temperature data index. This conversion is in fact an inverse heat conduction solution to a semi-infinite body. Accurate heat flux estimation using this method requires good knowledge of the material properties and accurate temperature measurements. Due to the nature of this integration method, temperature measurement error at any data point will lead to inaccurate heat flux estimation afterwards. Also, the estimation error damps very slow with time and its magnitude is proportional to the thermal effusivity, and inversely proportional to $1/(\Delta t)^{1/2}$ [17]. Therefore, this method is normally used to measure short period heat fluxes.

2.3 Heat Flux Sensors for Ash Fouling Monitoring

Heat flux sensors used for ash monitoring purpose are designed based on the basic heat flux measurement concepts introduced above. However, the environment in boilers is particularly severe, with high temperatures and corrosive combustion products. Therefore, modifications have to be made on the structure and sensor materials so that the sensor can withstand the condition for

a reasonable period of time. Review studies done by Valero and Cortbs [16] and Arai et al [1] discussed several different sensors developed for ash fouling monitoring during the past few decades [33-36]. The following section will discuss a few commonly used heat flux sensors

One traditional way of heat flux measurement in a boiler is the inserted thermocouple method which uses the water tube wall to produce the temperature gradient and to protect the thermocouples. Two slots are created in the tube wall with their ends located at two different depths as shown in Figure 2-10. Nowadays, special electro erosion technique is used to machine two miniature orifices to house thermocouples [1]. The process enables drilling of curved pathways through the water tube wall as indicated in Figure 2-10.

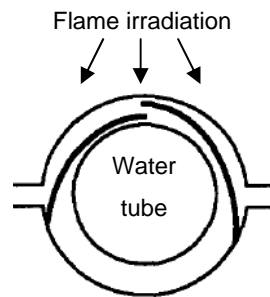


Figure 2-10: Inserted thermocouples [1]

Figure 2-11 illustrates the guarded cylinder sensor developed by the Central Electricity Generating Board [35, 36], based also on this concept.

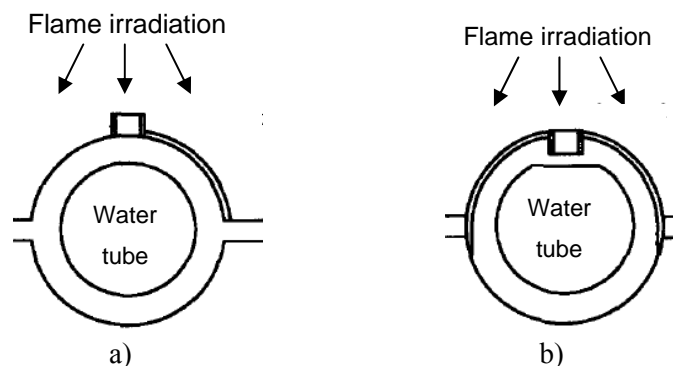


Figure 2-11: Guarded cylinder heat flux sensor, a) surface mounted, b) embedded [1]

The sensing element is a metal cylinder and two thermocouples are fixed at two different locations in the cylinder as shown in Figure 2-12. Temperature difference arises when heat is transferred from the sensor surface to the water tube. A thermal insulator is built around the cylinder to ensure that the heat transfer is one dimensional along the cylinder axis.

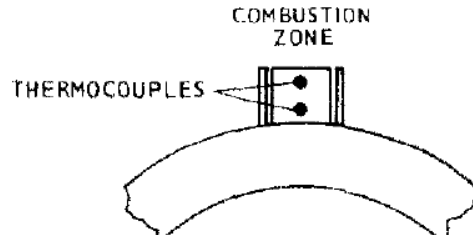


Figure 2-12: Thermocouple locations in the guarded cylinder sensor [35]

The sensors shown in Figure 2-11 a) and b) are essentially the same except the mounting method. The purpose of embedding the sensor in the water tube wall is to reduce the temperature difference between the sensor surface and the normal tube surface. However, little difference in performance was found between the two [1].

Circular foil concept can also be found in ash monitoring sensors. Heat flux sensor using this concept was first introduced by Northover [33] in 1967. The disc type sensor is mounted on the water tube as shown in Figure 2-13.

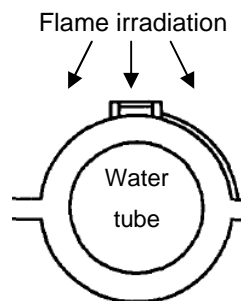


Figure 2-13: Disc type heat flux meter [1]

Figure 2-14 illustrates the structure of the sensor with more details. Although the structure is almost identical to the Gardon gage, the material of the sensor body and sensing disc, and the choice of thermocouple type are different due to the harsh condition the sensor has to withstand.

Disc material used for this sensor is Corronel 230, and the body material is British Driver Harris T2 alloy. To minimize the change of sensitivity with mean disc temperature, the thermocouples used in this sensor are Nickel-chromium and nickel-aluminium thermocouple. The cavity between the disc and the water tube surface is filled with argon and hermetically sealed.

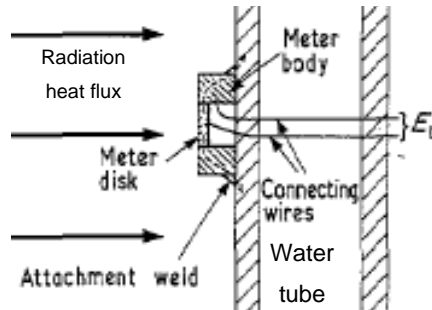


Figure 2-14: Disc type heat flux meter [33]

The heat flux sensors described above are referred to as the “dirty” heat flux sensors in an ash monitoring system. The concept of using “clean” and “dirty” heat flux sensor was first introduced by Chamber et al [11], whereby the surface of the “clean” heat flux sensor is kept clean by an air jet. Unlike the “dirty” sensors, the “clean” sensor is meant to detect the incident radiation heat flux on the water tube under the ash free condition.

However, heat flux sensor that incorporates an air screen was reported as early as 1970, developed by Hoogendoorn, et al [37] to monitor the heat flux in a vertical tube furnace. The structure of the sensor is rather complicate and it utilizes both air and water cooling. The tip of the sensor is shown in Figure 2-15.

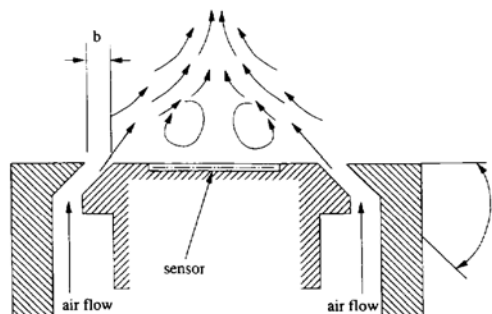


Figure 2-15: Heat flux sensor with an air screen [37]

The sensing element of the sensor comprises a copper disc and body, separated by a mild steel cylinder that served as the thermal resistance. The disc is exposed to the combustion gas, and the body is cooled by water. The temperature difference between the two parts is used as the dependent variable of the sensor. The air screen is used to prevent soot deposit and by turning on and off the air flow, the sensor is able to identify the intensities of radiative and convective heat fluxes separately.

The “clean” heat flux sensor designed by Brajuskovic et al [14, 15] is the basis of the present work. Like the one developed by Hoogendoorn, the sensor integrates the two functions: heat flux measurement and ash prevention into the sensor structure. The structure of this “clean” sensor is shown in Figure 2-16.

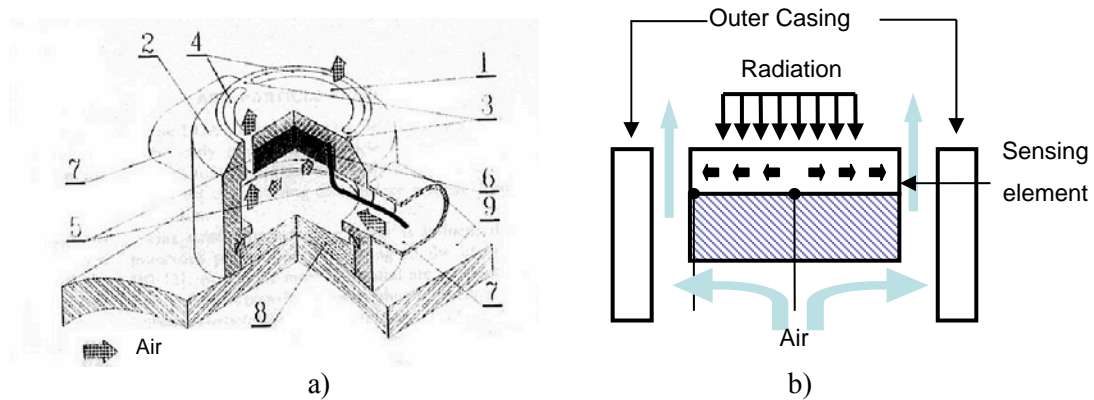


Figure 2-16: a) Structure [14] and b) operation principle of the “clean” heat flux sensor

The sensor is mounted on the water tube crown with its steel air supply pipes wrapped around the water tube. The disc shaped sensing element is connected to the sensor casing by two narrow ribs. The two semicircular gaps between the sensing disc and the casing form an annular channel from which air is blown out. The annular air jet serves three purposes: 1) cool down the sensing element; 2) protect the sensor surface from ash deposit; 3) generate radial temperature difference with the help of the insulation layer underneath the sensing element. The design is essentially another modification of the Gardon gage with both the sensing disc and the casing made of

stainless steel. The diameter of the sensing disc is 1cm and the width of the annulus gap is about 1mm. The thickness of the disc was not specified in the report. Two thermocouples are attached to the center and periphery of the sensing disc bottom to measure the temperatures at these two locations independently.

At steady state, the radiation energy absorbed at the top surface is partially removed from the top surface through convection caused by the annular jet recirculation. The rest of the absorbed energy is forced to conduct radially to the disc circumference, by the insulation layer underneath the disc, where it is removed by the annular air jet. Same as the Gardon gage, this radial heat transfer in the sensing disc creates a radial temperature difference as shown in Figure 2-17, which can be deduced from the temperatures measured by the two thermocouples.

A two-dimension numerical model was created based on a modified cylindrical heat conduction equation to study the heat transfer pattern in the sensing disc:

$$\frac{\partial^2 \Theta}{\partial r^2} + \frac{1}{r} \frac{\partial \Theta}{\partial r} + \frac{\partial^2 \Theta}{\partial z^2} = 0 \quad 2-50$$

where $\Theta(r, z) = T(r, z) - T(0, 0)$, r indicates the radius and z indicates the distance from the top surface of the disc. The boundary conditions used in the analysis were:

At the top surface, $z = 0$, $0 \leq r < R$

$$-k \frac{\partial \Theta(r, z)}{\partial z} = q_a - h_1 \Theta(r, z) \quad 2-51$$

where q_a is the absorbed radiation heat flux, and h_1 is the convection heat transfer coefficient at the top surface.

At the circumference surface, $0 < z < 1$, $r = R$

$$-k \frac{\partial \Theta(r, z)}{\partial r} = h_2 \Theta(r, z) \quad 2-52$$

where h_2 is the convection heat transfer coefficient in the annular channel.

At the bottom surface, $z = 1$, $0 \leq r < R$

$$-k \frac{\partial \Theta(r, z)}{\partial z} = 0$$

2-53

Numerically obtained temperature field under 100 kW/m^2 incident radiation heat flux is shown in Figure 2-17. The volumetric air flow rate in this case is $4.6 \cdot 10^{-3} \text{ m}^3/\text{s}$ and the resulting radial temperature difference is about 12 K.

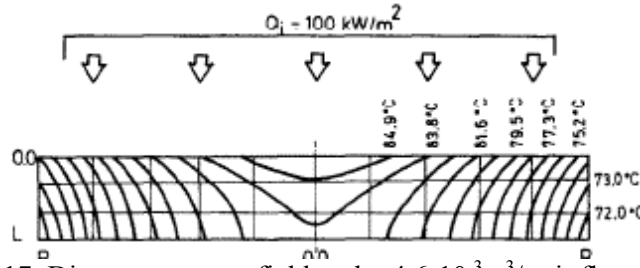


Figure 2-17: Disc temperature field under $4.6 \cdot 10^{-3} \text{ m}^3/\text{s}$ air flow rate [15]

From the temperature field, it can be seen that due to an increase in sensing disc thickness, the heat transfer in the disc is no longer one-dimensional as assumed for Gardon gage. This increase in thickness is considered necessary due to the severe environment in the boiler. The numerical solution gives a linear relationship between the radial temperature and incident radiation heat flux, also confirmed experimentally in the 15 to 100 kW/m^2 range as shown in Figure 2-18.

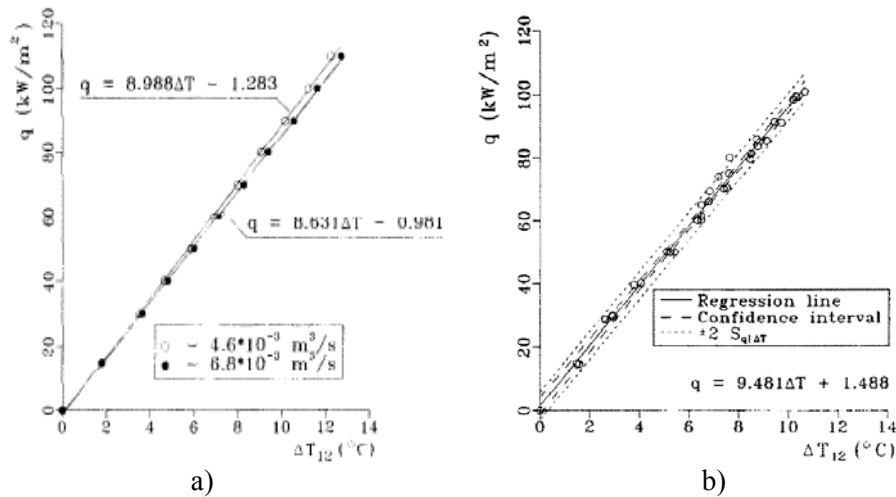


Figure 2-18: Sensor response curve: a) analytical results, b) experimental results [15]

Slight difference in the estimated sensitivity was found between the two sets of results. The ash prevention ability of this sensor was tested in lab scale [14]. The result was satisfactory at high air flow rates. However, the question about long term ability to keep sensor surface clean in the actual boiler was raised in [1]. As shown in Figure 2-18 a), the slope of the plot, which represents the inverse of the sensor sensitivity, decreases with increasing air flow rate (from $4.6 \cdot 10^{-3}$ to $6.8 \cdot 10^{-3} \text{ m}^3/\text{s}$), indicating that the sensitivity increases with increasing air flow rate.

More recently, a new type of “clean” heat flux sensor based on the one-dimensional planar sensor is under development [38-41]. Unlike conventional sensors, the sensing element is a porous disc as shown in Figure 2-19. Two thermocouples are inserted at two different depths inside the disc.

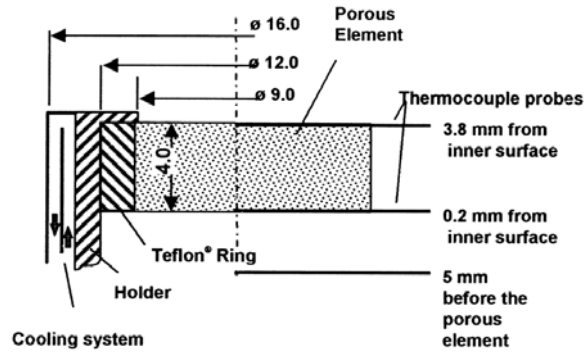


Figure 2-19: Cross section view of the porous media sensor [29]

Air is blown through the porous disc with a pulsating flow rate. At one flow rate, the sensor measures the combined radiation and convection heat flux and at another specially designed flow rate, the boundary layer at the top surface is said to be destroyed and the sensor can measure the radiation heat flux only. Therefore, by combining the results, this sensor is claimed to be able to measure the radiation and convection heat flux separately while keeping the surface of the sensing element clean.

Chapter 3 Sensor Design

The ash monitoring prototype developed consists of one “clean” heat flux sensor and one “dirty” heat flux sensor. The two sensors were made to be installed through the access port on the boiler wall (Figure 3-1). The advantage of using the access port is that sensors can be installed without interrupting the boiler operation.



Figure 3-1: Access port on the boiler wall

Several factors were taken into consideration during the design process: functionality, manufacturing difficulty, assemblage and installation procedure, and configuration flexibility. Details of the design and operation procedures for both “clean” and “dirty” sensors are illustrated in the following section.

3.1 “Clean” Heat Flux Sensor

3.1.1 Sensor Structure

The tip of the new “clean” heat flux sensor adopted the design presented in [14]. The original “clean” sensor was designed to be mounted on a water tube surface as shown in the previous chapter, while the new sensor is to be inserted into the access port. Hence, the belt shaped air supply was replaced by a stainless steel tube, with 20 inches in length, and 0.75 inches in outer diameter, 0.66 inches in inner diameter (Figure 3-2).



Figure 3-2 : Body of the heat flux probe with sensor tip detached

The inner wall at the front end of the tube is threaded to form connection with the outer casing of the sensor tip. A three-way connector is soldered onto the rear end of the tube to form two separate ports for air inlet and thermocouples (Figure 3-3).

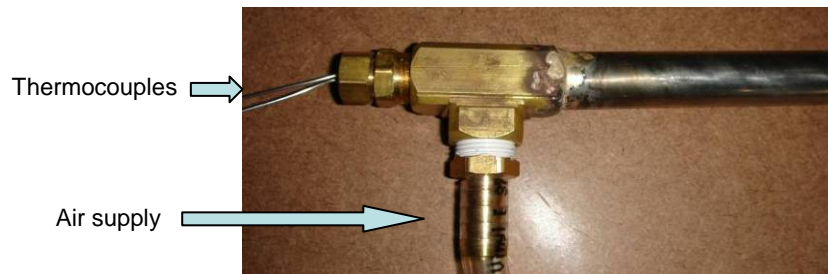


Figure 3-3: Rear end of the “clean” heat flux probe

Unlike the original sensor tip, the new design separates the sensor tip into two components: outer casing (Figure 3-4 a) and sensing element (Figure 3-4 b), both of which are made of stainless steel.

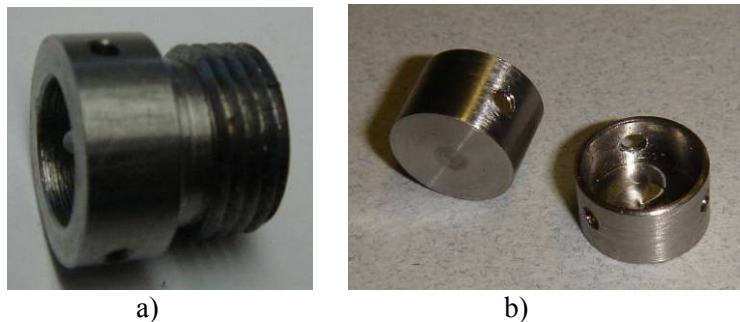


Figure 3-4: Sensor tip components a) outer casing, b) sensing element

The sensor casing has the same outer diameter as the air supply tube. The inner diameter of the casing is a design variable that governs the dimensions of the annular channel. Casings with two different inner diameters near the exit, 12mm and 11mm, were made and tested in the present work. The corresponding widths of the annular gaps are 1mm and 0.5mm. The rear end of the

casing is threaded to form connection with the air supply tube (Figure 3-4 a). The diameter of the cup shaped sensing element is 10 mm (same as the original sensor). The bottom wall of the cup is essentially the sensing disc and the purpose of the cup wall is to hold the insulation material and is referred to as the insulation shell in the context of this thesis. Sensing disc with 2mm thickness was tested in the present work. Although sensor with thinner sensing disc has higher sensitivity as explained earlier, thicker sensing disc is mechanically stronger which is considered necessary given the environment in which the sensor will be deployed. Also, when dealing with unsteady heat fluxes, the sensing disc acts as a low pass filter. The analysis done by Stolyarov [42] showed that sensor with thicker sensing element could filter out more noise contained in the surface heat flux and thus the values of the dependent variables would be more stable. Results from preliminary models also confirmed this conclusion and is shown in Chapter 4.

The height of the insulation shell is 3 mm and the thickness is 0.5 mm. Three threaded holes are drilled on the insulation shell as shown in Figure 3-4 b). The thickness of the insulation shell in the original sensor is only 0.1mm. This is because in the original design, the sensing element was linked to the outer casing by two connecting ribs at its top surface level. The interference of the ribs on the air flow structure was detectable, especially at the near-exit region, which might impair the ash prevention ability of the sensor. In addition, the ribs can cause uneven temperature distribution at the disc bottom surface which becomes noticeable at lower air flow rates ($<4.6 \cdot 10^{-3} \text{ m}^2/\text{s}$) and higher heat flux levels ($>50 \text{ kW/m}^2$) [15]. To reduce the impact of the connecting mechanism on the sensor performance, in the new design, the connection mechanism is moved upstream from the sensor face and is connected to the insulation shell instead of the disc itself. As a result, the wall thickness is increased to allow threaded holes to be made and to ensure adequate strength. The assembled sensor tip is shown in Figure 3-6 where the two components are coaxially connected to each other by three screws.



Figure 3-5: Sensing element connected to casing by three screws

The manufacturing process for each component is relatively simple. Also, separating the entire probe into three component allows easier configuration variation, i.e. change of width of the annular gap was achieved by replacing an outer casing with different inner diameter while keeping other components. The configuration flexibility is desired during this development process.

The insulation material used in the current sensor is mineral wool which has a thermal conductivity of $0.04 \text{ W/(m}\cdot\text{K)}$. Two thermocouples are inserted from the rear end of the air supply tube, passing through the 1 mm thick insulation cover, and are attached to the center and periphery of the sensing disc bottom as shown in Figure 3-6. The thermocouples used in the “clean” heat flux sensor are K type with 1 mm in diameter and grounded junction.

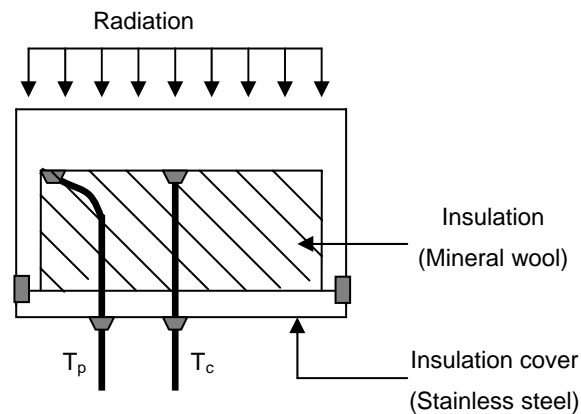


Figure 3-6: “Clean” sensor thermocouple installation

The insulation cover is then soldered onto insulation shell to seal the cavity. The thermocouples are also secured to the insulation cover to avoid detachment of the junctions during handling.

3.1.2 Measurement Concepts

Two different measurement methods were tested on the new “clean” heat flux sensor. The first one is the radial temperature difference (RTD) method employed in the original sensor. The second method is proposed in the present study which is based on the amplitude of the disc temperature oscillation generated by a varying air flow rate. It has been shown in the previous chapter that the sensitivity of a heat flux sensor is generally determined by the geometry and material properties of the sensing element. However, the distinct way the “clean” heat flux sensor operates introduces another factor: air flow rate. Results from the previous study have shown a strong relationship between the overall temperature of the sensing element and the air flow rate. From the heat balance perspective, this is caused by the convective heat transfer coefficient variation when the air flow rate is changed. Using Equation 2-26 and 2-6, the radiation and convection heat transfer at the sensing element can be expressed as:

$$q_{rad} = \sigma \epsilon A_{top} (T_{env}^4 - T_{top}^4) \approx \sigma \epsilon A_{top} T_{env}^4 \quad 3-1$$

$$q_{conv} = h_{top} A_{top} (T_{top} - T_f) + h_{cir} A_{cir} (T_{cir} - T_f) \quad 3-2$$

where *cir* denotes the circumference surface of the sensing element, *top* denotes the top surface of the sensing element and *f* denotes the air flow. The above expressions ignore the radiation received at the circumference surface and assumed constant air temperature. When the conduction heat transfer through the bottom surface of the sensing disc can be ignored, the change of the sensing disc temperature can be expressed as:

$$mc_p \frac{\partial T}{\partial t} = q_{conv} + q_{rad} \quad 3-3$$

At thermal equilibrium, the radiation energy absorbed by the sensing element is equal to the energy removed through convection and therefore, the overall temperature of the sensing element remains constant.

$$q_{conv} = -q_{rad} \quad 3-4$$

$$\frac{\partial T}{\partial t} = \frac{q_{conv} + q_{rad}}{mc_p} = 0 \quad 3-5$$

At the instant of the air flow rate change, the convective heat transfer coefficients h_{top} and h_{cir} are changed while the surface temperatures of the sensing element remain the same. The system is then no longer in thermal equilibrium.

$$q_{conv} \neq -q_{rad} \quad 3-6$$

$$\frac{\partial T}{\partial t} = \frac{q_{conv} + q_{rad}}{mc_p} \neq 0 \quad 3-7$$

The overall temperature of the sensing element starts to change over time until new equilibrium is reached. Under a constant radiation level, the temperature of the sensing element at thermal equilibrium is governed by the air flow rate.

For the original heat flux sensor, previous numerical study has shown that under a 100kW/m^2 incident radiation heat flux, 50% increase in air flow rate led to a 23K temperature drop at the center of the sensing disc bottom, which is 90% greater than the RTD at that radiation level. Hence, ideally, utilizing this temperature difference as the dependent variable of the sensor could increase the sensitivity of the sensor without varying the structure of the sensing element. However, generating this temperature difference with a single “clean” sensor means the flow rate has to be changed continuously between two different levels. In practice, time required to reach the two equilibrium temperatures is relatively long, which indicates very low sampling rate since the temperature amplitude value is only available every half period. Therefore, the air flow is controlled to oscillate between two flow rates with a certain period. Earlier in the project, air flow

rate oscillation with square wave form (Equation 3-8) was employed while later tests employed sinusoidal air flow rate as shown in Equation 3-9 in order to generate smoother change in air flow rate and hence sensor temperature.

$$\begin{cases} \dot{m}(t) = \dot{m}_1, \text{ when } (2i)(P/2) < t < (2i+1)(P/2) \\ \dot{m}(t) = \dot{m}_2, \text{ when } (2i+1)(P/2) < t < 2(i+1)(P/2) \end{cases} \quad i=1,2,3,\dots,N \quad 3-8$$

where P is the period of the oscillation cycle, \dot{m}_1 and \dot{m}_2 are two different air flow rates.

$$\dot{m}(t) = \dot{m}_0 + \dot{m}_A \sin(\omega t) \quad 3-9$$

where ω is related to the period of oscillation as

$$\omega = \frac{2\pi}{P}, \quad 3-10$$

and \dot{m}_0 and \dot{m}_A can be expressed in terms of \dot{m}_1 and \dot{m}_2 as:

$$\dot{m}_0 = (\dot{m}_1 + \dot{m}_2) / 2 \quad 3-11$$

$$\dot{m}_A = |\dot{m}_1 - \dot{m}_2| / 2 \quad 3-12$$

For the new method, the temperature oscillation at the center of the disc bottom (T_c) is recorded, and the amplitude of the T_c oscillation (A_c) is extracted to serve as the new dependent variable.

As mentioned earlier, sensors with two different channel sizes were tested in the present work. For the sensor with 1mm annular channel, the maximum and minimum air flow rates used were 7.9 g/s and 2 g/s. However, it was realized later in the project that the air flow rate available in the power station was lower. Therefore, in order to maintain the exit velocity of the annular jet under lower air flow rate, sensor with 0.5mm channel was made and tested. The corresponding air flow rates were decided so that the maximum and minimum volumetric average velocities, as defined in Equation 2-10, were approximately the same as the ones in the 1mm channel case. The maximum and minimum air flow rates for the 0.5mm channel were 3.8 g/s and 0.95 g/s (Table 3-1).

Table 3-1: Air flow rates for the two sensors

	V (SLM)	U _m (m/s)	Re(U _m)
0.5mm channel	48	48.5	7071
	190	192.0	28282
1mm channel	100	48.2	14061
	400	192.9	56243

In order to gain some preliminary understanding of the relationship between the performance of the proposed oscillation method and various sensor parameters, the analysis of the semi-infinite solid body under a sinusoidal surface heat flux described in Chapter 2 is applied. Although the conditions are not the same, i.e. the actual problem is two dimensional even under the axial-symmetric assumption and the boundary conditions of the sensor are more complicated, the analysis can still provide an idea of the relationship between the A_c and various parameters. Under the assumption that the sensing disc is semi-infinite and the total heat flux received at the top surface of the sensor is a stable sinusoidal function of time, at distance δ from the top surface, the temperature oscillation can be expressed as:

$$T_{ac}(x, t) = \frac{q''_0}{2} \frac{e^{-\delta/\mu}}{\varepsilon\sqrt{\omega}} \cos\left[\frac{\delta}{\mu} - \omega t + \frac{\pi}{4}\right] \quad 3-13$$

Here δ can be treated as the thickness of the sensing disc. The amplitude of the temperature oscillation at distance δ from the top surface can be expressed in terms of the amplitude of the surface heat flux as:

$$A_c = \frac{q''_0}{2} \frac{e^{-\delta/\mu}}{\varepsilon\sqrt{\omega}} \quad 3-14$$

Since the measured quantity is not the amplitude of the heat flux oscillation but the surface incident radiation, the relationship between the incident radiation heat flux and the amplitude of the heat flux oscillation is needed to bridge the two. Through the results of the preliminary numerical simulations models as will be shown in Chapter 4, a few key parameters were identified although the actual relationship was not quantified. It was found that the amplitude of

heat flux oscillation q''_o is affected by the air flow rates, flow oscillation period, and surface radiation absorptivity. The results also showed that A_c is indeed inversely proportional to the thickness and thermal diffusivity and effusivity of the sensing element. Therefore, by combining the analytical and numerical analysis, the A_c can be related to the incident radiation as:

$$A_c = K(\alpha, \dot{m}_1, \dot{m}_2, \omega) \cdot q''_{inc} \frac{e^{-\delta/\mu}}{\varepsilon\sqrt{\omega}} \quad 3-15$$

where K is a function of surface emissivity of the sensing element α , maximum and minimum air flow rates \dot{m}_1 and \dot{m}_2 , and the frequency of the air flow oscillation ω . The four controlling parameters in the bracket are, the percentage of radiation heat flux absorbed, α , the convection heat transfer coefficients determined by \dot{m}_1 and \dot{m}_2 , and the duration of the heating and cooling process cycle ω which controls the total amount of heat that enters or leaves the system each cycle. The sensitivity of the new method can then be related to these parameters as:

$$X_{A_c} = \frac{dA_c}{dq''_{inc}} = K(\alpha, \dot{m}_1, \dot{m}_2, \omega) \frac{e^{-\delta/\mu}}{\varepsilon\sqrt{\omega}} \quad 3-16$$

The above expression gives an estimate of the relationship between the sensitivity of the sensor and various parameters when using the A_c as the new dependent variable. However, the exact value of the sensitivity can only be estimated numerically and experimentally. Same as the RTD method, the sensitivity of the oscillation method will be constant if all the parameters in Equation 3-16 are independent of the incident radiation heat flux which is hardly the case in reality. Inconsistency in the sensitivity is expected, especially at high heat flux levels when the temperature of the “clean” heat flux sensor is elevated.

3.2 “Dirty” Heat Flux Sensor

Although not the major scope of the present study, a “dirty” sensor was designed to provide a direct indication of the incident radiation heat flux generated by the radiation source. The “dirty”

heat flux sensor prototype adopts the concept of the one dimensional planar sensor described in Chapter 2. The sensor is made of stainless steel with two holes drilled into it for thermocouple installation (Figure 3-8). One thermocouple is inserted through the hole and is soldered near the top surface, while the other one is fixed into the shallow hole at the bottom surface. The two holes are located 180 deg apart. The axial distance between the two thermocouples is approximately 4mm.



Figure 3-7: Tip of the “dirty” heat flux sensor a) top view, b) bottom view

Similar to the design of the “clean” heat flux sensor, the end of the “dirty” heat flux sensor tip was threaded to form a connection with the steel sensor probe stem. The assembled “dirty” heat flux sensor is shown in Figure 3-9.



Figure 3-8: Assembled “dirty” heat flux sensor

Figure 3-10 illustrates the internal structure at the front end of the “dirty” sensor probe. The probe body for the “dirty” sensor consists of two concentric steel tubes. Water comes in from the inner tube, impinges on the bottom surface of the sensing element to remove the heat absorbed by the

sensing element at the top surface then exits the tube through the annular duct between the outer and inner tubes. The temperature difference between the top and bottom surfaces created by this axial heat transfer is captured by the two thermocouples (type K, grounded junction, 1.5 mm in diameter). In order to ensure one dimensional heat transfer, the circumference surface of the sensing element needs to be insulated during operation.

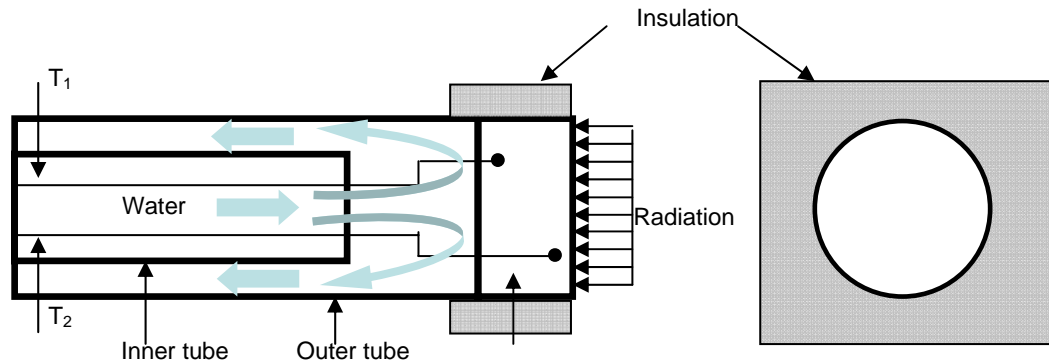


Figure 3-9: Structure of the “dirty” heat flux sensor

The rear end of the “dirty” probe is shown in Figure 3-10. A T-shape connector was attached to the inner tube to separate the thermocouple outlet and water inlet. A hole was drilled on the wall of the outer tube as the water outlet.

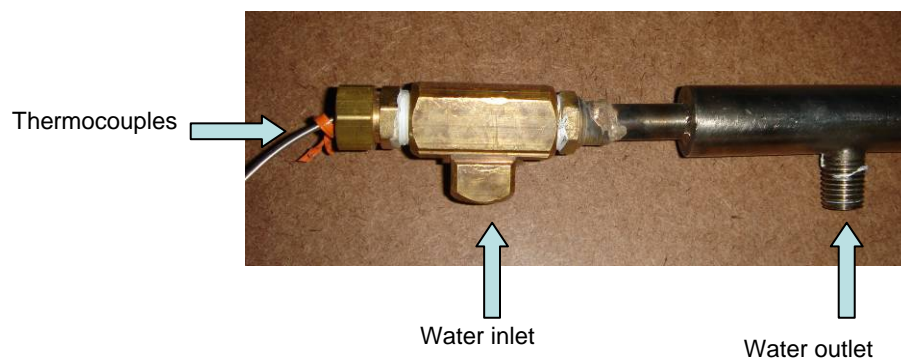


Figure 3-10: Rear end of the “dirty” sensor probe

Although this design might not be the best option for ash fouling monitoring since the shape and the temperature of its exposed surface are different from those of the water tubes in the boiler (sensor surface: flat, lower temperature, water tube surface: semicircular, higher temperature), the

measurement can still be used as a reference during the experiment and provide a rough assessment of the ash fouling condition during the *in-situ* test. Because the dirty sensor is based on the spatial temperature difference concept, the conversion process is also straightforward. A linear relationship between the temperature difference and the incident radiation heat flux is assumed, and the heat flux can be expressed as:

$$q''_{inc}(i) = \frac{1}{X_{Dir}} dT_{Dir}(i) + C_{Dir} \quad 3-17$$

where X_{Dir} is the sensitivity for the “dirty” sensor and C_{Dir} is a constant. The “dirty” heat flux sensor is supposedly to be calibrated based on the received heat flux. Ideally, this can be done by simply adding the radiation absorptivity of the sensor surface into Equation 3-18 to get

$$q''_a(i) = \alpha \left(\frac{1}{X_{Dir}} dT_{Dir}(i) + C_{Dir} \right) \quad 3-18$$

However, the actual radiation absorptivity of the sensor was not known and as will be shown in Chapter 6, the surface of the sensing element experienced significant change through the experiment which indicates that the radiation absorptivity could change over time. This can be visually observed as darkening of the surface after it has been exposed to heat.

3.3 Data Processing Procedures

During the operation, the dependent variables of the sensor are to be converted to heat fluxes using functions with experimentally estimated parameters. When using the RTD method the dependent variable can be obtained at every data acquisition point by simply calculating the difference between T_c and T_p :

$$RTD(i) = T_c(i) - T_p(i) \quad 3-19$$

The surface incident radiation (steady or unsteady) is estimated directly through a linear equation:

$$q''_{inc}(i) = \frac{1}{X_{RTD}} RTD(i) + C_{RTD} \quad 3-20$$

where X_{RTD} is the sensitivity coefficient and C_{RTD} is a constant. However, when using the oscillation method, the “clean” heat flux sensor becomes a temporal temperature difference based sensor and difficulties were realized when attempting to apply the new method in practice. Unlike the RTD method, additional effort is required to extract the dependent variable (amplitude of the T_c oscillation) from the temperature data in an on-line basis. Moreover, the task becomes more challenging when dealing with the T_c oscillation distorted by unsteady heat fluxes. To resolve the issues, three different data processing procedures were developed over the course of study and explained in the following section. These procedures were created under the assumption that the temperature data is uniformly sampled. The first procedure was created when realizing that under a stable incident radiation, the amplitude of the temperature oscillation is essentially the peak to peak temperature difference, which can be represented by the local maximum values of the half period temperature difference (HPTD). Therefore, the amplitude of the temperature oscillation can be estimated based on the discrete temperature data as

$$A_c(j) = \max |T_{jn+i} - T_{(j-1/2)n+i}| \quad 3-21$$

$$j = 1, 2, \dots, M, \quad i = 1, 2, 3, \dots, n/2$$

where M is the number of peak to peak values and n is the number of temperature readings per cycle. The incident radiation heat flux can then be estimated in the same manner as the RTD method:

$$q''_{inc}(j) = \frac{1}{X_{A_c}} A_c(j) + C_{A_c} \quad 3-22$$

where X_{A_c} is the sensitivity and C_{A_c} is a constant. However, a significant weakness of this method is that the results become unstable when the sensor is experiencing an unsteady incident radiation heat flux as will be shown in later chapters. As described in Chapter 2, the absolute value of T_c

can be decomposed into three components according to Equation 2-36: temperature of the air jet T_{air} , time-independent temperature rise above the air temperature T_{dc} , and T_{ac} , the temperature oscillation caused by the varying air flow. However, when the incident radiation is unstable, Equation 2-37 becomes

$$T_c(t) = T_{air} + T_{dc}(x, t) + T_{ac}(x, t) \quad 3-23$$

in which the T_{dc} term also becomes time dependent and therefore distorts the temperature oscillation and cripples the half period temperature difference method. To resolve this issue, another data processing procedure was created. The concept of this method is similar to that employed in Equation 2-49 where the surface heat flux on a semi-infinite solid is estimated through integration of the rate of surface temperature change. However, since the sensor is under a periodical convection heat flux, instead of calculating the rate of temperature change between two adjacent temperature readings, the method calculates the difference of two temperature readings that are one period apart (OPTD):

$$dT_{lp}(i) = T_{jn+i} - T_{(j-1)n+i} \quad 3-24$$

$$j = 1, 2, \dots, M, \quad i = 1, 2, 3, \dots, n$$

where lp represents one oscillation period. The incident radiation heat flux can then be estimated by dT_{lp} using the following expression.

$$q''_{inc}(N) = \sum_{i=1}^N C_{lp} \frac{dT_{lp}(i)}{P} + q''_{initial} \quad 3-25$$

$$i = 1, 2, 3, \dots, N$$

where C_{lp} is a constant that is to be estimated experimentally and P is the oscillation period, and the estimation is based on $q''_{initial}$ provided by the half period temperature difference procedure before the heat flux starts to change. The main problem of this method is that once an error occurs in the temperature measurement, all the heat flux estimations afterwards are biased on since they all track the changes only. Because the sensor is intended to monitor the boiler for a long period

of time, the procedure cannot be used independently but only as a secondary procedure that assists the half period temperature difference method to deal with the unstable incident radiation situation. A simple conversion code was created (Appendix C) by combining these two methods and uses the rate of change of the one period temperature difference as the indicator to determine which procedure to switch to. The third method is essentially an improvement of the first one. As will be shown in later chapters, this method alone is able to provide reasonable estimations under both steady and unsteady incident radiation heat fluxes. The method is named central temperature difference (CTD) procedure in the present work and the formula of the method is shown in Equation 3-26:

$$A_c(j) = \max \left| \frac{(T_{(j-1)n+i} + T_{jn+i})}{2} - T_{(j-1/2)n+i} \right| \quad 3-26$$

$$j = 1, 2, \dots, M, \quad i = 1, 2, 3, \dots, n/2$$

The heat flux estimation is then obtained through Equation 3-22. It is important to note that both the second and third methods require the temperature history one period before the estimation point, while the first method requires the temperature history half period before the estimation point. Assisted by the experimental results, the working principles of these three methods are further discussed in Chapter 6.

Chapter 4 Numerical Model and Results

Gambit and FLUENT package was used for all the numerical simulations in this project. The package is widely used in industry and academic for solving fluid flow and heat transfer problems. The structure and grids are generated in Gambit, and the problem is then solved in FLUENT. Only the “clean” heat flux sensor was studied numerically in the present work. Numerical analysis played two roles in different stages of this project. Preliminary results demonstrated the relationship derived analytically between the dependent variables and various parameters of the sensor. They also proved the feasibility of the proposed oscillation method and helped to identify the data processing problems at the earlier stage of the study. Later models followed more closely to the actual structure of the “clean” heat flux sensor prototype and the flow configuration employed in the experiment. The purpose of these simulations was to help understand the flow and heat transfer pattern of the “clean” sensor and to estimate the sensitivities of the sensor under different configurations and measurement method, as well as their consistency at higher heat flux levels that are beyond the experiment calibration range. Under high level heat fluxes, the temperature of the sensing disc is expected to rise accordingly which would lead to change in thermal properties the disc material. As shown previously, the sensitivity of a heat flux sensor is directly related to the thermal properties of the sensor material. Therefore, it is necessary to evaluate the consistency of the sensitivities under boiler heat flux levels. Preliminary simulations were done on a PC with Centrino Duo CPU, while later ones were solved using High Performance Computing Virtual Laboratory (HPCVL) and a desktop workstation equipped with icore 7 CPU.

4.1 Physical Models

This section discusses the governing equations and models that are employed in FLUENT to solve the fluid flow and heat transfer problems.

4.1.1 Turbulence Model

Given the Reynolds numbers calculated in Chapter 3 for the cases tested in the present study, the air flow is considered fully turbulent. As mentioned in Chapter 2, the instantaneous velocity, pressure of a turbulence flow can be represented as

$$\begin{aligned} u_i &= \bar{u}_i + u_i' \\ p &= \bar{p} + p' \end{aligned} \quad 4-1$$

The continuity and momentum equations can then be expressed in terms of the time-averaged values as Reynolds-averaged Navier-Stokes (RANS) equations:

$$\frac{\partial \rho}{\partial t} + \frac{\partial}{\partial x_i}(\rho u_i) = 0 \quad 4-2$$

$$\frac{\partial}{\partial t}(\rho u_i) + \frac{\partial}{\partial x_j}(\rho u_i u_j) = -\frac{\partial p}{\partial x_i} + \frac{\partial}{\partial x_j} \left[\mu \frac{\partial u_i}{\partial x_j} + \frac{\partial u_j}{\partial x_i} - \frac{2}{3} \delta_{ij} \frac{\partial u_l}{\partial x_l} \right] + \frac{\partial}{\partial x_j}(-\overline{\rho u_i' u_j'}) \quad 4-3$$

The additional information for the Reynolds stresses term $-\overline{\rho u_i' u_j'}$ is needed to solve Equation 3-4. Boussinesq hypothesis and Reynolds Stress Transport Models (RSM) are the two modeling methods commonly used when applying Reynolds-Averaged approach to solve the Reynolds stresses term. With Boussinesq hypothesis, the Reynolds stresses are related to the mean velocity gradients by:

$$(-\overline{\rho u_i' u_j'}) = \mu_t \left(\frac{\partial u_i}{\partial x_j} + \frac{\partial u_j}{\partial x_i} \right) - \frac{2}{3} \delta_{ij} \left(\rho k + \mu_t \frac{\partial u_k}{\partial x_k} \right) \quad 4-4$$

where μ_t is the turbulent viscosity and k is the turbulence kinetic energy, δ_{ij} is the Kronecker delta term [43]. The advantage of this approach is the relatively low computational cost. However, the isotropic turbulence viscosity assumption made in this approach is not always true and hence the

result can be inaccurate in some cases. Although the critical Reynolds number for an annular jet was not found in the literatures, Vanierschot, et al [24] mentioned in their report that at $Re=6000$ the flow is turbulent. As shown in Chapter 3, the lowest Reynolds number in the cases studied in the present work is 7071. Therefore, the flow was regarded as turbulent in all cases. In the present study, $k-\varepsilon$ turbulence model, which utilizes the Boussinesq hypothesis, was used for all the simulations. $k-\varepsilon$ model is perhaps the most widely used and validated turbulence model [43], in which the turbulence viscosity is defined as:

$$\mu_t = \rho C_\mu \frac{k^2}{\varepsilon} \quad 4-5$$

where ε is the rate of dissipation of turbulent kinetic energy and C_μ is a dimensionless constant. However, the performance of standard $k-\varepsilon$ model does not perform well when dealing with weak shear layers, and the spreading rate of axial-symmetric jets in stagnant surroundings is severely over-predicted. The model also has problems in swirling flows and flows in highly curved boundary layers and diverging passages [43]. The modeled “clean” heat flux sensor can be treated as an annular jet channel. The convective heat transfer at the top surface of the sensing element is driven by the strong recirculation at the center of the annular jet. Therefore, standard $k-\varepsilon$ model is not considered the most appropriate turbulence model in this case. Another turbulence model available in FLUENT is the realizable $k-\varepsilon$ model which is modified based on the standard $k-\varepsilon$ model. Compared with standard $k-\varepsilon$ model, the realizable $k-\varepsilon$ model can more accurately predicts the spreading rate of both planar and round jets. It is also likely to provide better performance for flows involving rotation, boundary layers under strong adverse pressure gradients, separation and recirculation [25]. Hence, the realizable $k-\varepsilon$ model was considered adequate for the flow situation involved with the “clean” heat flux sensor and was used in all the simulations. The two transport equations for realizable model are:

$$\frac{\partial}{\partial t}(\rho k) + \frac{\partial}{\partial x_i}(\rho k u_i) = \frac{\partial}{\partial x_j} \left[\left(\mu + \frac{\mu_t}{\sigma_k} \right) \frac{\partial k}{\partial x_j} \right] + G_k - \rho \varepsilon - Y_M \quad 4-6$$

$$\frac{\partial}{\partial t}(\rho\varepsilon) + \frac{\partial}{\partial x_i}(\rho\varepsilon u_i) = \frac{\partial}{\partial x_j} \left[\left(\mu + \frac{\mu_t}{\sigma_\varepsilon} \right) \frac{\partial \varepsilon}{\partial x_j} \right] - \rho C_2 \frac{\varepsilon^2}{k + \sqrt{\nu \varepsilon}} \quad 4-7$$

where G_k represents the generation of turbulence kinetic energy due to the mean velocity gradients, Y_M represents the contribution of the fluctuation dilatation in compressible turbulence to the overall dissipation rate, and C_2 is a constant. G_k and Y_M are calculated as:

$$G_k = -\overline{\rho u'_i u'_j} \frac{\partial u_j}{\partial x_i} \quad 4-8$$

$$Y_M = 2\rho\varepsilon M_t^2 \quad 4-9$$

where M_t is the turbulent Mach number defined as:

$$M_t = \sqrt{\frac{k}{a^2}} \quad 4-10$$

4.1.2 Wall Functions

To successfully predict the surface convection in the current problem, heat and mass transfer at the near wall region need to be resolved with reasonable accuracy. Two treatment approaches are available in FLUENT to deal with the interaction between walls and fluid flow: wall-functions and near-wall model. When the boundary layer at the wall is turbulent, it can be divided into three layers: viscous sub-layer, buffer layer and the turbulence core. For the near-wall model, turbulence models are modified to resolve the entire boundary layer with a mesh all the way to the wall. However, this approach requires high mesh density near the wall which leads to significant increase in computation time. When the wall-function approach is employed, semi-empirical formulas are used to bridge the viscous affected region between the wall and the fully-turbulent region. This approach substantially saves computational resources, because the viscosity-affected region does not need to be resolved. Among the available wall functions in FLUENT, the non-equilibrium wall function was considered more appropriate given the flow

situation involved in the annular jet of the “clean” heat flux sensor. The non-equilibrium wall function is reported to provide better prediction of wall shear and heat transfer in complex flows involving separations, reattachment, and impingement where the mean flow and turbulence are subjected to severe pressure gradients and change rapidly [25].

4.1.3 Heat Transfer

All three forms of heat transfer: convection, conduction and radiation, are considered important at the sensing element. During the simulation, heat transfer is solved simultaneously with the fluid flow. The general energy equation in FLUENT has the following form:

$$\frac{\partial}{\partial t}(\rho E) + \nabla \cdot (\vec{v}(\rho E + p)) = \nabla \cdot (k_{eff} \nabla T - \sum_j h_j \vec{J}_j + (\vec{\tau}_{eff} \cdot \vec{v})) + S_h \quad 4-11$$

where $k_{eff} = k + k_t$ is the effective conductivity. k_t is the turbulent thermal conductivity which is defined according to the turbulence model applied, and \vec{J}_j is the diffusion flux of species j . $(\tau_{ij})_{eff}$ is the stress tensor that determines the viscous heating. In preliminary models, viscous heating terms was not considered but was included in later ones due to the relatively high flow velocity encountered at upper flow rates. For the sensor with 1mm annular channel, the Mach number of the air flow in the channel can reach 0.7 when the air flow rate is 7.9g/s. Viscous heating is considered important when the Brinkman number, as defined in Chapter 2, is greater than 1. The result from the final model has shown that for the sensor with 1mm annular channel, 7.9g/s air flow rate and under a 56kW/m² incident radiation heat flux, the Brinkman number in the channel is approximately 1.2. Although there is no chemical reaction or heat generation involved in this problem, heat generation term S_h takes into account the radiation heat source. The energy term E is defined as:

$$E = h - \frac{p}{\rho} + \frac{v^2}{2} \quad 4-12$$

The sensible enthalpy h for ideal gas compressible flow is defined as:

$$h = \sum_j Y_j h_j \quad 4-13$$

where Y_j is the mass fraction of species j . Because only air was involved in the simulation in this case, the sensible enthalpy was essential the enthalpy of air. When using realizable k - ε model, the energy equation becomes

$$\frac{\partial}{\partial t}(\rho E) + \frac{\partial}{\partial x_i}[u_i(\rho E + p)] = \frac{\partial}{\partial x_i}(k_{eff} \frac{\partial T}{\partial x_j} + u_i(\tau_{ij})_{eff}) + S_h \quad 4-14$$

The stress tensor $(\tau_{ij})_{eff}$ is defined as:

$$(\tau_{ij})_{eff} = \mu_{eff} \left(\frac{\partial u_j}{\partial x_i} + \frac{\partial u_i}{\partial x_j} \right) - \frac{2}{3} \mu_{eff} \frac{\partial u_k}{\partial x_k} \delta_{ij} \quad 4-15$$

The effective thermal conductivity is defined as:

$$k_{eff} = k + \frac{c_p \mu_t}{Pr_t} \quad 4-16$$

where Pr_t is the turbulence Prandtl number.

When dealing with conduction, the energy equation is simplified to the following form in the solid region due to the absence of fluid or solid motion. The general equation becomes the Fourier's heat conduction equation:

$$\frac{\partial}{\partial t}(\rho h) = \nabla \cdot (k \nabla T) + S_h \quad 4-17$$

where ρ and k are the density and thermal conductivity of the solids.

Because of the unique form of radiation heat transfer, additional models are needed to resolve the problem. Five different radiation models are available in FLUENT: Discrete Transfer Radiation Model (DTRM), P-1 Radiation Model, Rosseland Radiation Model, Surface to Surface (S2S) Radiation Model and Discrete Ordinates (DO) Radiation Model. The current model attempts to simulate the situation in the boiler where the radiation comes mainly from the fireball and hot flue

gas, hence, DTRM, P-1 and DO radiation models were considered. However, the radiation heat flux on the sensor surface is controlled by the backflow pressure at the pressure outlets, and within the modeled region, air is considered transparent and therefore the optical thickness $a \cdot L$ (where a is the absorption coefficient of air, and L is the length scale for the domain) is essentially 0. Among the remaining candidates, only DTRM and the DO model are considered appropriate for optically thin cases ($a \cdot L < 1$). However, a critical limitation of DTRM model is that it is not compatible with parallel processing. Since all the simulations are done on multiple processors, DO radiation model appears to be the best choice for resolving the radiation heat transfer in this problem. DO radiation model solves the radiative transfer equation for a finite number of discrete solid angles, each associated with a vector direction “ s ” fixed in the global Cartesian system [25]. In DO model, the incident radiation on grey diffuse walls, as which the surfaces of the heat flux sensor are defined, is calculated as:

$$q''_{inc} = \int_{\vec{s}\vec{n}} I_{inc} \vec{s} \cdot \vec{n} d\Omega \quad 4-18$$

where I is the incident radiation intensity \vec{s} is the directional vector, \vec{n} is the refractive index of the medium next to the wall, and Ω is the solid angle.

4.2 Model Setup

4.2.1 Layout and Boundary Conditions

Based on the geometry of the “clean” heat flux sensor, the modeled domain was assumed to be axi-symmetrical. Although under this assumption the connecting screws that link the sensing element and the outer casing were ignored in the model and their impact on the flow field downstream, local and overall heat transfer pattern would not be accounted for, the assumption was considered necessary since taking them into account would require three dimensional modeling, which would be too time consuming given the time frame of the project. The model

also ignored the influence of the rising hot gas in the power plant boiler. However, the impact of rising hot gas was considered negligible since the annular jet is expected to have much greater velocity than that of the rising flow in the boiler and therefore dominates the heat transfer near sensing element. As mentioned in [14], the flux gas velocity in the furnace varies between 5 and 7m/s which is much smaller than the exit velocity of the annular jet which varies between 48 to 192m/s. Figure 4-1 is the layout of the preliminary models, and Figure 4-2 and 4-3 are of the later models with 1mm and 0.5mm annular channel respectively. For all the models, the sensing element was treated as a stationary two layer solid phase with the additional 0.5mm thick insulation shell added in later models. The thickness of the steel disc is 2mm and the thickness of the insulation layer is 3mm. The steel insulation cover at the bottom of the sensing element was ignored in all cases. The cover is behind the insulation layer and is only connected to the sensing element around the edge of the insulation shell, it was considered to have little influence on the overall heat transfer as well as the temperature of the sensing disc.

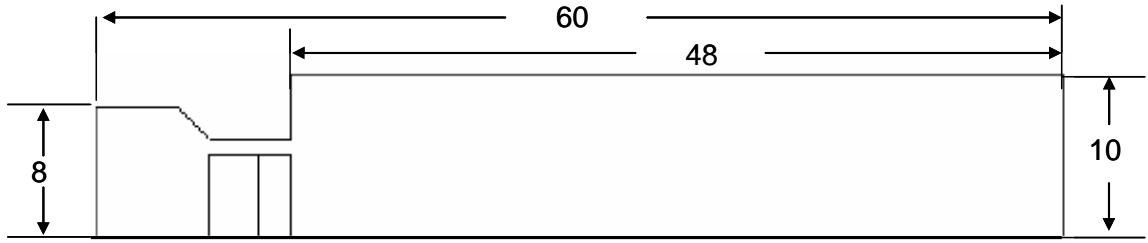


Figure 4-1: Layout for preliminary models (all units in mm)

The overall dimensions for preliminary models are shown in Figure 4-1. The two later models had similar dimensions except at the flow inlet and the addition of insulation shell. The diameter of the air inlet was reduced to 6 mm in later models according to the actual “clean” sensor prototype. The boundary conditions for the models are shown in Figure 4-2. The only change made in the later models was to change the inlet boundary from “velocity inlet” to “mass flow inlet” as the air was assumed incompressible in preliminary models and compressible in later ones. Layout for the sensor with 0.5 mm annular channel is shown in Figure 4-3. The only

difference is the geometry of the inner wall of the outer casing.

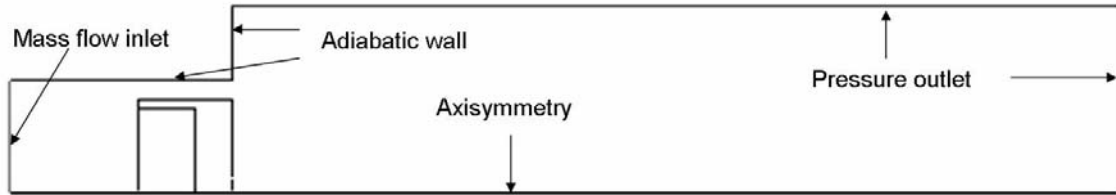


Figure 4-2: Layout and boundary conditions for final model (1mm channel)



Figure 4-3: Layout for final model (0.5 mm channel)

User defined functions (UDFs) were used to specify the boundary condition at the air inlet when simulating the oscillation method. Square wave form air flow oscillation was applied in the preliminary models and sinusoidal wave form was applied in the final models. For the final steady state simulations, the air inlet boundary was specified in terms of mass flow rate (g/s), and for the final transient simulations, the air inlet boundary was specified in terms of mass flux ($\text{kg/m}^2\text{s}$). The mass flow rate in the experiment was measured in terms of standard liter per minute (SLM). Table 4-1 lists the corresponding mass flow rate in terms of (g/s) and also mass flux values that are specified in the UDFs (Appendix A).

Table 4-1: Air inlet mass flow rates

Mass flow rate (SLM)	Mass flow rate (g/s)	Mass flux ($\text{kg/m}^2\text{s}$)
48	0.95	8.42
100	2	17.55
190	3.8	33.34
400	7.9	70.18

The walls that separate the two solid blocks and the solid and gas phases were treated as coupled

walls which allow heat exchange between the two sides of the walls. The incident radiation heat flux at the top surface of the sensing element was controlled by the back flow temperature (BFT) of the pressure outlets. For the unsteady heat flux cases tested in the preliminary models, UDFs were applied to control the BFT. In the final models, the sensor was tested under six constant BFTs which along with the corresponding incident radiation heat flux values are listed in Table 4-2.

Table 4-2: BFT and corresponding incident radiation heat flux

BFT (K)	q''_{inc} (kW/m ²)
800	19.4
1000	56.7
1200	117.6
1400	217.8
1600	371.6
1700	473.6

The maximum heat flux level was decided according to the information provided in [1]. In the preliminary models, the total hemispherical absorptivity of the sensor surface was set to one, because it was assumed that the sensor surface would be covered by high absorptivity coating. However, it was later realized that given the condition in the boiler, it was difficult for any type of coating to adhere to the surface permanently. Therefore grey diffuse surface with a total hemispherical absorptivity of 0.4 was used for all the walls of the sensing element in final simulations. The value was also used in the numerical analysis conducted by Afgan, et al [15].

4.2.2 Grid Setup

Relatively coarser mesh was used in the preliminary simulations as their purpose was only to provide initial assessment of performance of the two measurement methods and to evaluate the feasibility of the oscillation method. A total of 13520 cells were used in the preliminary models. Figure 4-4 shows the grids near and within the sensing element.

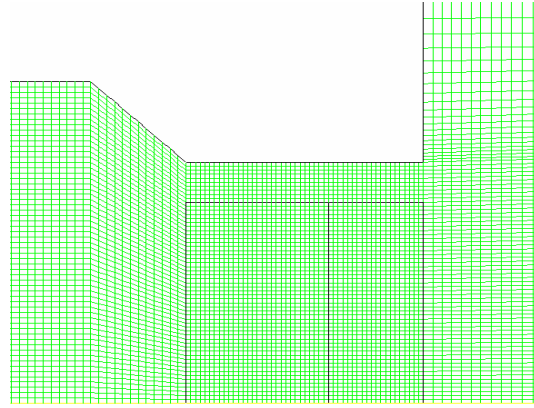


Figure 4-4: Grid within and near the sensor (preliminary model)

The simple geometry of the model allowed structured grid with quadric cells to be applied to the entire domain. Since the focus was on the heat transfer inside and around the sensing element, denser grid was applied at this region. The mesh density was then gradually decreased near the air inlet and outlet. The final models had much high overall mesh density than the preliminary model since the purpose of these models was to provide a more accurate analysis of the heat transfer and fluid flow of the system and to assess the sensitivities of the two methods under various conditions. The final models contain 110200 cells while models with 39600 cells and 61950 cells were made for grid sensitivity study purpose. Figure 4-5 shows the grid near and within the sensor for the final model.

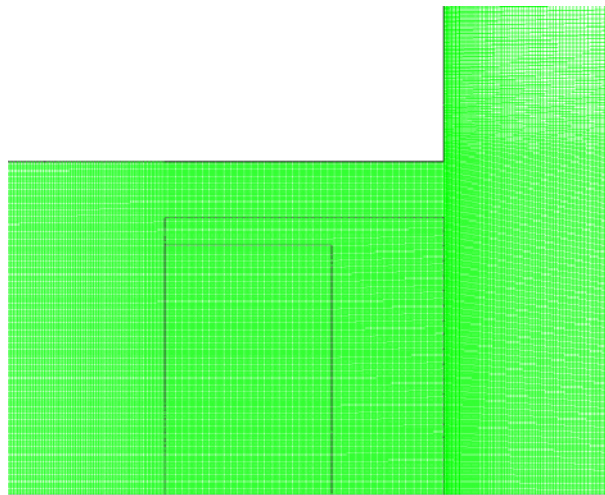


Figure 4-5: Grid within and near the sensor (final model)

4.2.3 Material Properties

In preliminary models, air was assumed incompressible with constant thermal properties. In the final models, air was treated as compressible flow with its density set to follow the ideal gas law. The thermal conductivity and heat capacity of air were approximated by two polynomial functions of temperature based on the values listed in [19]:

$$k = 7 \cdot 10^{-5} T + 0.0074 \text{ (W / m} \cdot \text{K)} \quad 4-19$$

$$c_p = 3 \cdot 10^{-4} T^2 - 0.1027T + 1011.56 \text{ (J / kg} \cdot \text{K)} \quad 4-20$$

Sutherland viscosity law with three coefficients was adopted to define the viscosity of air:

$$\mu = \mu_0 \left(\frac{T}{T_0} \right)^{3/2} \frac{T_0 + S}{T + S} \quad 4-21$$

where $\mu_0 = 1.716 \cdot 10^{-5} \text{ kg/m} \cdot \text{s}$ is the reference viscosity, $T_0 = 273.11 \text{ K}$ is the reference temperature, $S = 110.56 \text{ K}$ is the Sutherland constant. The material properties of the sensing element were set based on stainless steel 302 given in [19]. The density was set as constant 8030 kg/m^3 . The thermal conductivity and heat capacity were defined by two polynomial functions of temperature:

$$k = 2 \cdot 10^{-6} T^2 + 0.0111T + 12.74 \text{ (W / m} \cdot \text{K)} \quad 4-22$$

$$c_p = -2 \cdot 10^{-7} T^3 + 3 \cdot 10^{-4} T^2 + 0.058T + 457.4 \text{ (J / kg} \cdot \text{K)} \quad 4-23$$

As mentioned previously, the insulation material used in the actual sensor was mineral wool. Its density, thermal conductivity and heat capacity were set at constant values as listed in Table 4-3 [44].

Table 4-3: Material properties of mineral wool

$\rho(\text{kg/m}^3)$	$k \text{ (W/mK)}$	$c_p(\text{J/kgK})$
150	0.04	890

4.2.4 Numerical Setup

Two numerical methods are offered in FLUENT: pressure-based solver and density-based solver. Although pressure-based solver was designed mainly for low speed incompressible flows and density-based solver is for high speed compressible flows, both of them have been reformulated and are capable of solving a wide range of flow conditions. In the present work, although simulations were run as compressible flow in all cases, since flow was always subsonic the pressure-based solver was used.

In terms of pressure-velocity coupling, there are four different algorithms in FLUENT: SIMPLE, SIMPLEC, PISO and Coupled. The first three use segregated algorithm and Coupled uses coupled solver. In the final models, both steady state and transient simulations, Coupled approach was used. Compared with the segregated approaches, it solves the momentum and pressure-based continuity equations together and is more robust to implement.

The governing equations for transported quantities are discretized using a control volume based technique. In the final models, for steady and transient simulations, second order upwind biased scheme was applied to the spatial discretization. The face value ϕ_f is calculated using

$$\phi_{f,SOU} = \phi + \nabla \phi \cdot \vec{r} \quad 4-24$$

where ϕ and $\nabla \phi$ are the cell-centered value and its gradient in the upstream cell, and \vec{r} is the displacement vector from the upstream cell centroid to the face centroid. Compared with the first-order discretization, the second order scheme produces more accurate results but generally yields poorer convergence. For transient simulations, the governing equations also need to be discretized in time. Temporal discretization involves the integration of every time in the differential equations over a time step Δt . First order implicit scheme (Equation 4-25) was used for temporal discretization for the transient simulations.

$$\frac{\phi^{n+1} - \phi^n}{\Delta t} = F(\phi^{n+1}) \quad 4-25$$

where ϕ is the scalar quantity, and n and $n+1$ represent the value at the current time level and the value at the next time level. The advantage of the fully implicit scheme is that it is unconditionally stable with respect to the time step size. Given the nonlinearity associated with the problem, it is difficult to obtain a fully converged solution. For the steady state simulations in the final model, the solutions were considered to be converged when the net heat transfer rate at the sensing element became less than 1% of the heat transfer rate at the top surface of the sensor, which generally would require 90000 iterations. For transient simulations, the time step was set at 0.01 second and the maximum number of iterations per time step was set at 40.

4.3 Numerical Results

The results of the preliminary models were used as the initial assessment of the performance of the system under steady and unsteady radiation heat flux heat fluxes and different sensor configurations. The results of these tests are shown in Appendix A. The numerical models built after the experiment gives more realistic estimations and the results are shown in this section.

Both steady and unsteady state simulations were conducted under six constant incident radiation heat flux levels. The purposes of the steady state simulations were to study the air flow pattern and the heat transfer at the sensing element, and also to evaluate the consistency of the sensitivities for the RTD method under the maximum and minimum air flow rates for each sensor channel. The oscillation method was studied using transient simulations.

Grid Sensitivity Test

Models of the sensor with 1mm annular channel were tested under 56kW/m^2 incident radiation heat flux using three different mesh densities. The results, including the values of T_c , T_p , RTD and the A_c are listed in Table 4-4.

Table 4-4: Grid sensitivity test results

Number of grids	Coarse (39600)		Medium (61950)		Fine (110200)	
Flow rate (g/s)	2	7.9	2	7.9	2	7.9
T_c (K)	316.5	305.5	313.5	304.75	311.17	303.75
T_p (K)	313.25	302.75	310.5	302	308.42	301.03
RTD (K)	3.25	2.75	3	2.75	2.75	2.72
A_c (K)	9.8		7.8		6.5	

In accordance to the results shown in Table 4-3, all the variables decrease as the mesh density becomes higher. However, the rate of change becomes less as the total number of cells increases, indicating a diminishing effect of the mesh density increase. Figure 4-6 to 4-9 illustrate the profiles of the velocity magnitude for the flow in the annular channel and after it exits the channel in these cases. In Figure 4-6 and 4-7, x/H represents the ratio between the distance from the bottom of the sensing element and the axial length of the sensing element. In Figure 4-8 and 4-9, x/D_i represents the ratio between the distance from the exit of the annular channel and the diameter of the sensing disc.

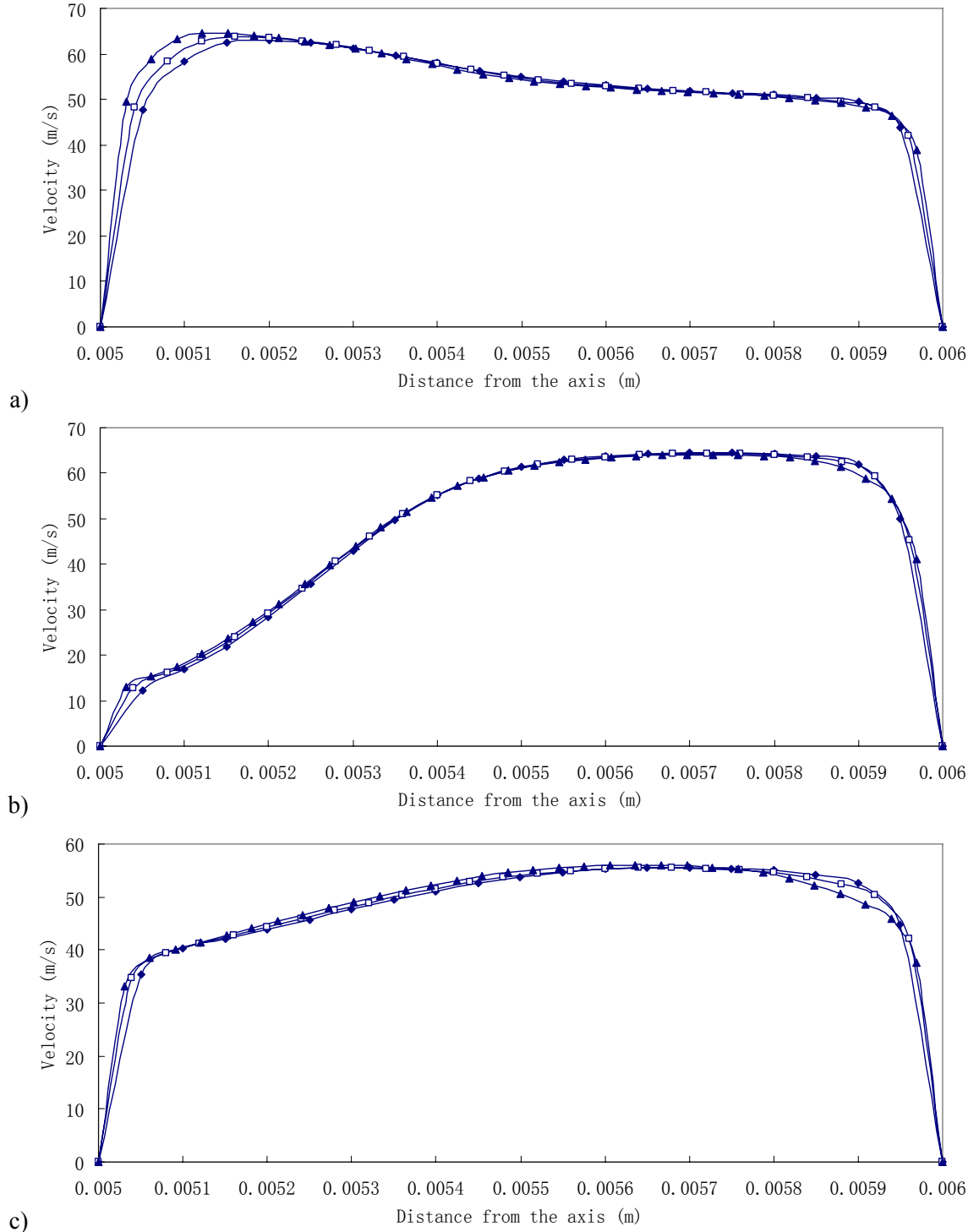
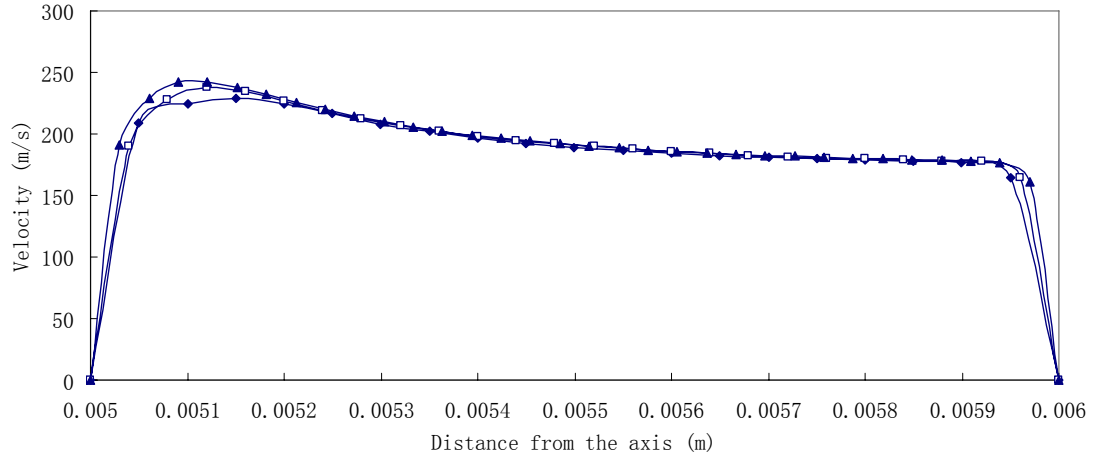
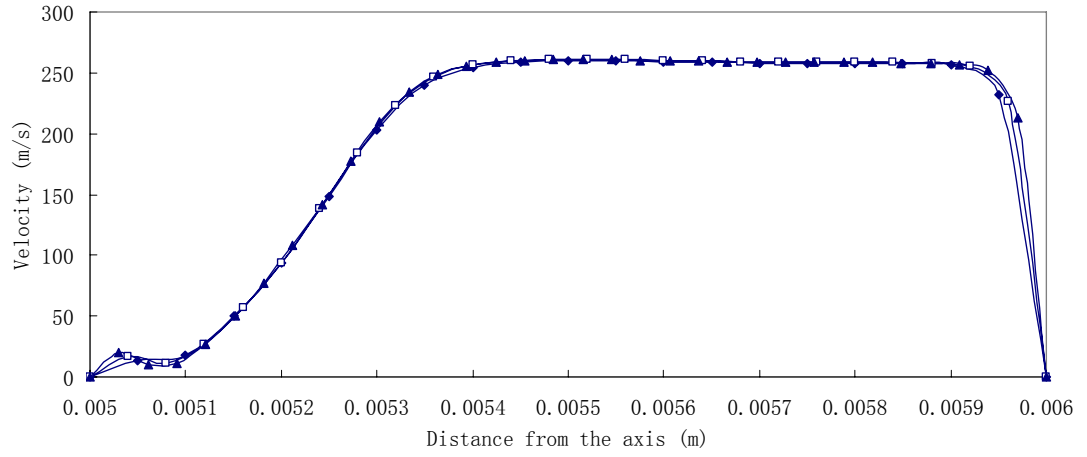


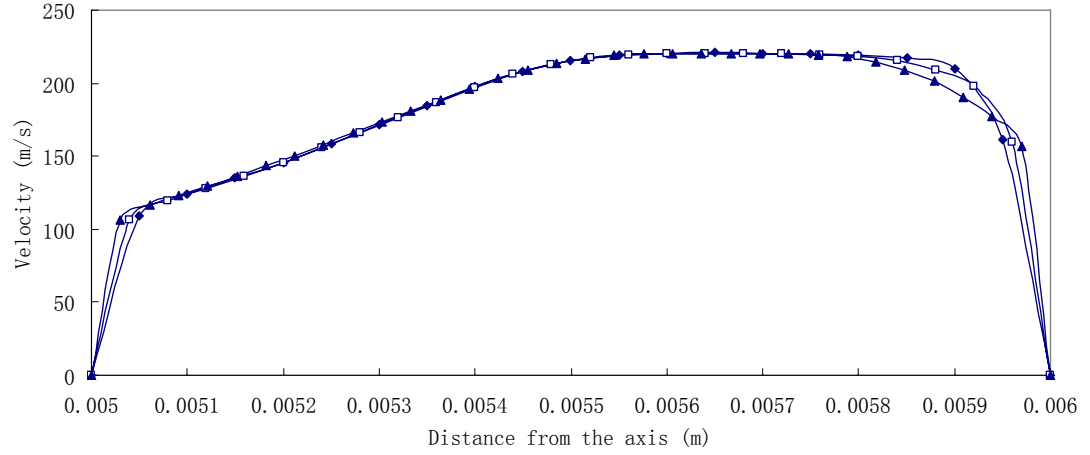
Figure 4-6: Velocity profile in the annular channel, $\dot{m}=2\text{g/s}$, $\text{Re}=14061$, \blacklozenge Coarse, \square Medium, \blacktriangle Fine, location: a) $x/H=0$, b) $x/H=0.3$, c) $x/H=1$



a)



b)



c)

Figure 4-7: Velocity profile in the annular channel, $\dot{m}=7.9\text{g/s}$, $\text{Re}=56243$, \blacklozenge Coarse, \square Medium, \blacktriangle Fine, location: a) $x/H=0$, b) $x/H=0.3$, c) $x/H=1$

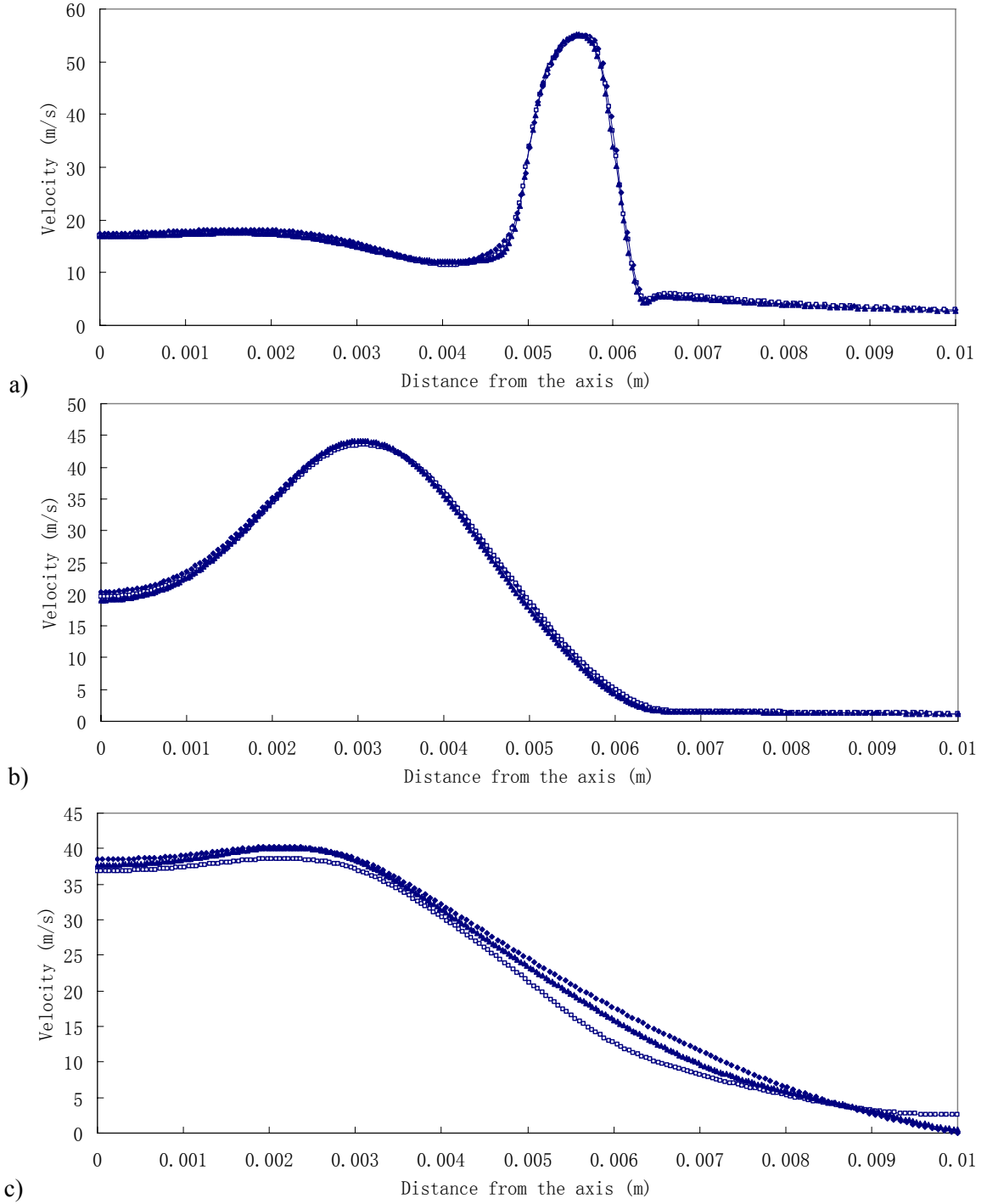


Figure 4-8: Velocity profile of the annular jet, $\dot{m}=2\text{g/s}$, $\text{Re}=14061$, \blacklozenge Coarse, \square Medium, \blacktriangle Fine, location: a) $x/D_i=0.1$, b) $x/D_i=1$, c) $x/D_i=4$

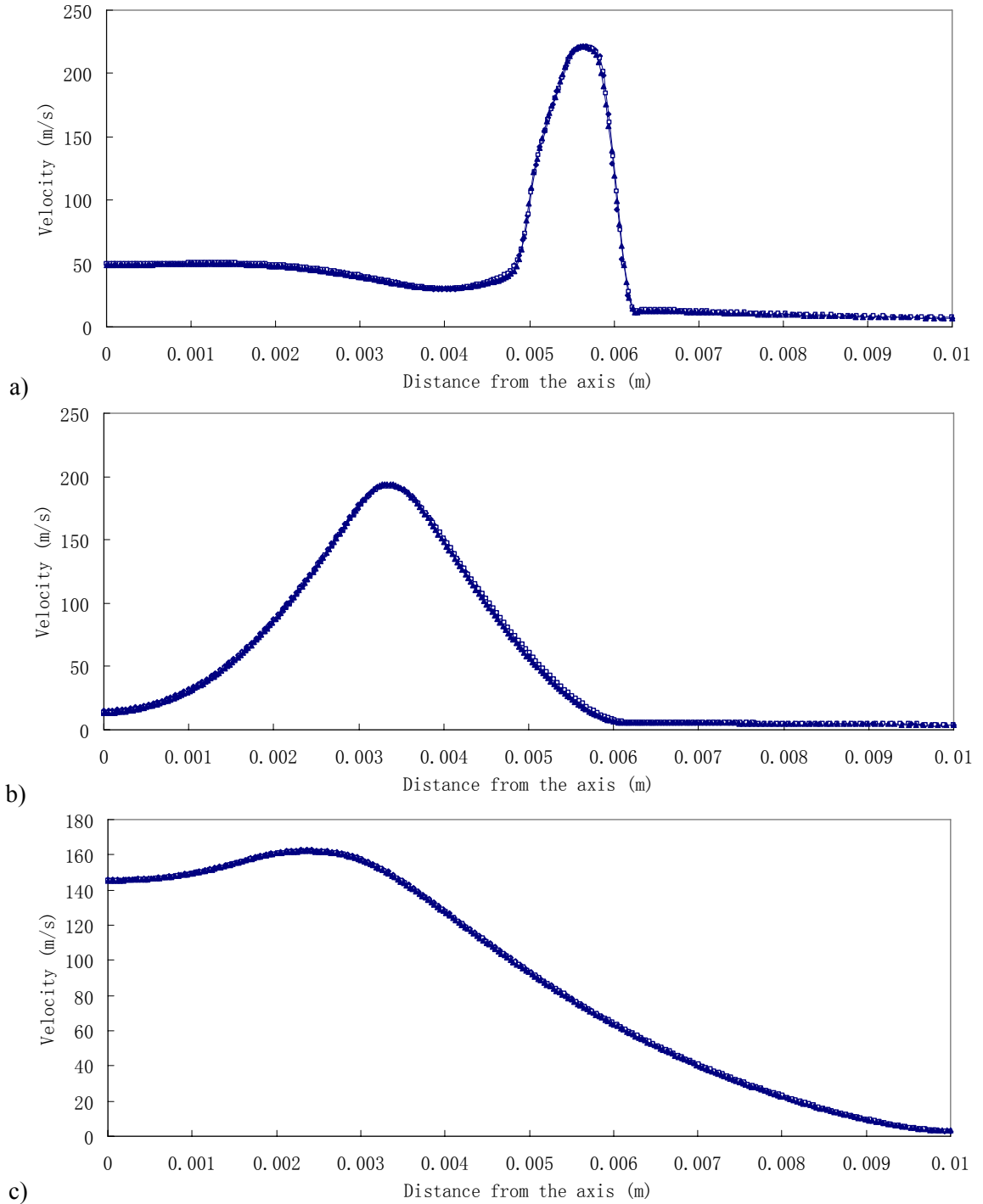


Figure 4-9: Velocity profile of the annular jet, $\dot{m}=7.9\text{g/s}$, $\text{Re}=56243$, \blacklozenge Coarse, \square Medium, \blacktriangle Fine, location: a) $x/D_i=0.1$, b) $x/D_i=1$, c) $x/D_i=4$

No significant difference in the pattern is observed among these four groups of results, which indicates that the flow pattern was relatively consistent as the mesh density changes. Therefore

the model with 110200 cells was considered adequate for the purpose of the study and models with even higher mesh density would require too much computation time and with no significant improvement in results.

Steady State Results (1mm channel)

Air flow conditions at two locations were considered important in the present study: flow in the annular channel and flow near the top surface of the sensor. Figure 4-10 shows the path line of the air flow in the annular channel and Figure 4-11 shows the path line of the air flow adjacent to the top surface of the sensor.

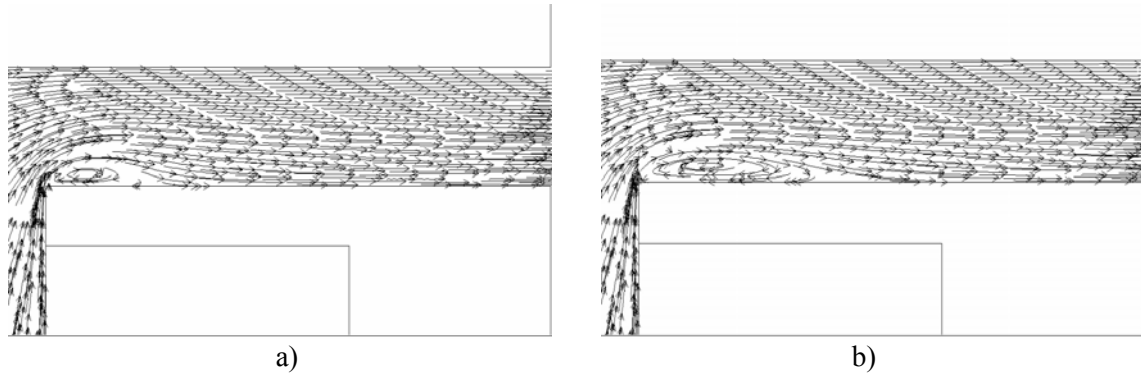


Figure 4-10: Path line in the annular channel, a) $\dot{m}=2$ g/s, $Re=14061$, b) $\dot{m}=7.9$ g/s, $Re=56242$

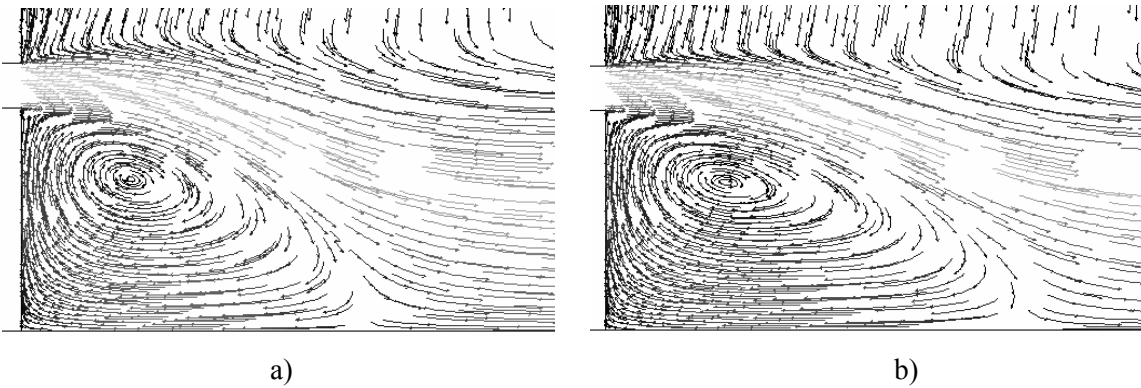


Figure 4-11: Center recirculation zone, a) $\dot{m}=2$ g/s, $Re=14061$, b) $\dot{m}=7.9$ g/s, $Re=56242$

As shown in Figure 4-10, air flow is forced into the annular channel when it approaches the bottom surface of the sensor. This sudden decrease in flow area generates large velocity gradient near the inlet of the annular channel. At the channel inlet, flow acceleration is further prompted

by the recirculation bubble, which virtually reduces the width of the channel at the inlet. It can also be seen that the size of the recirculation bubble increases with the air flow rate. When the air flow exits the annular channel, it forms large recirculation zone in front of the sensing element, named central recirculation zone (CRZ) by Vanierschot [24]. As shown in Figure 4-11, the air flow forms an annular jet with its front drawn towards the center axis by the subatmospheric pressure field at the CRZ. The axial length of the CRZ also increases with the air flow rate. The axial length of the CRZ was often related to the outer diameter of the annular nozzle. Several authors have studied experimentally the relationship between the size of the CRZ and the geometry of the nozzle. Ko and Chan [45] reported a CRZ length of $0.5D_o$ using an annular nozzle with D_o/D_i ratio of 2.2 and U_m of 50m/s. Vanierschot [24] recorded a CRZ length of $0.56D_o$ using an annular nozzle with D_o/D_i ratio of 1.67 and Re of 7500. For the sensor with 1mm channel, the D_o/D_i ratio is 1.2, and for the sensor with 0.5mm channel, as will be shown next, the D_o/D_i ratio is 1.1. Based on the numerical results, at 2 g/s ($Re \approx 14000$) air flow rate, the axial length of the CRZ is about $0.63D_o$ (0.76cm) and at 7.9 g/s ($Re \approx 56000$) air flow rate, its axial length increases to approximately $0.83D_o$ (1cm). This information was important to the experimental analysis because it provided a quantitative indication of the flow field adjacent to the sensing element which helped to realize the potential impact of the sapphire window on the heat transfer at the sensing element when the sensor-to-window distance became small. More will be discussed in Chapter 5. The variations of total heat flux at the top surface along the radius of the sensing element at the two tested air flow rates are illustrated in Figure 4-12.

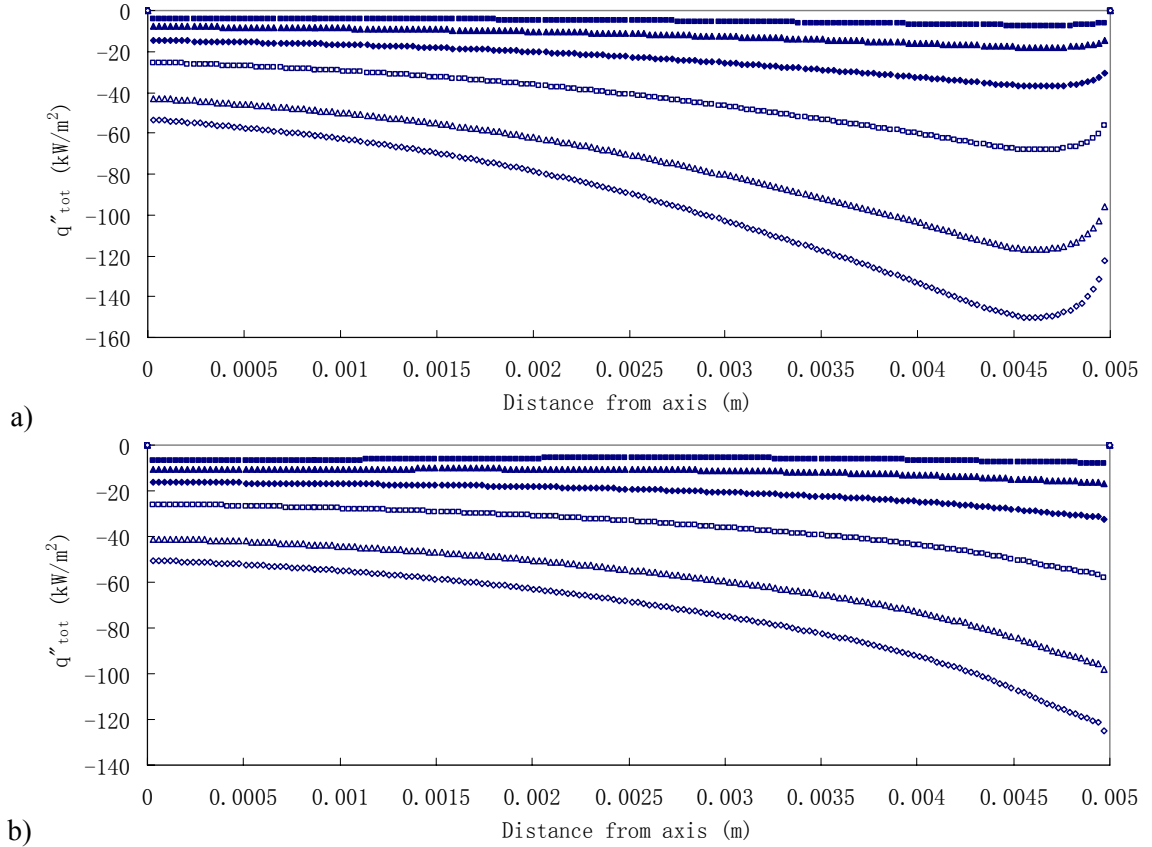
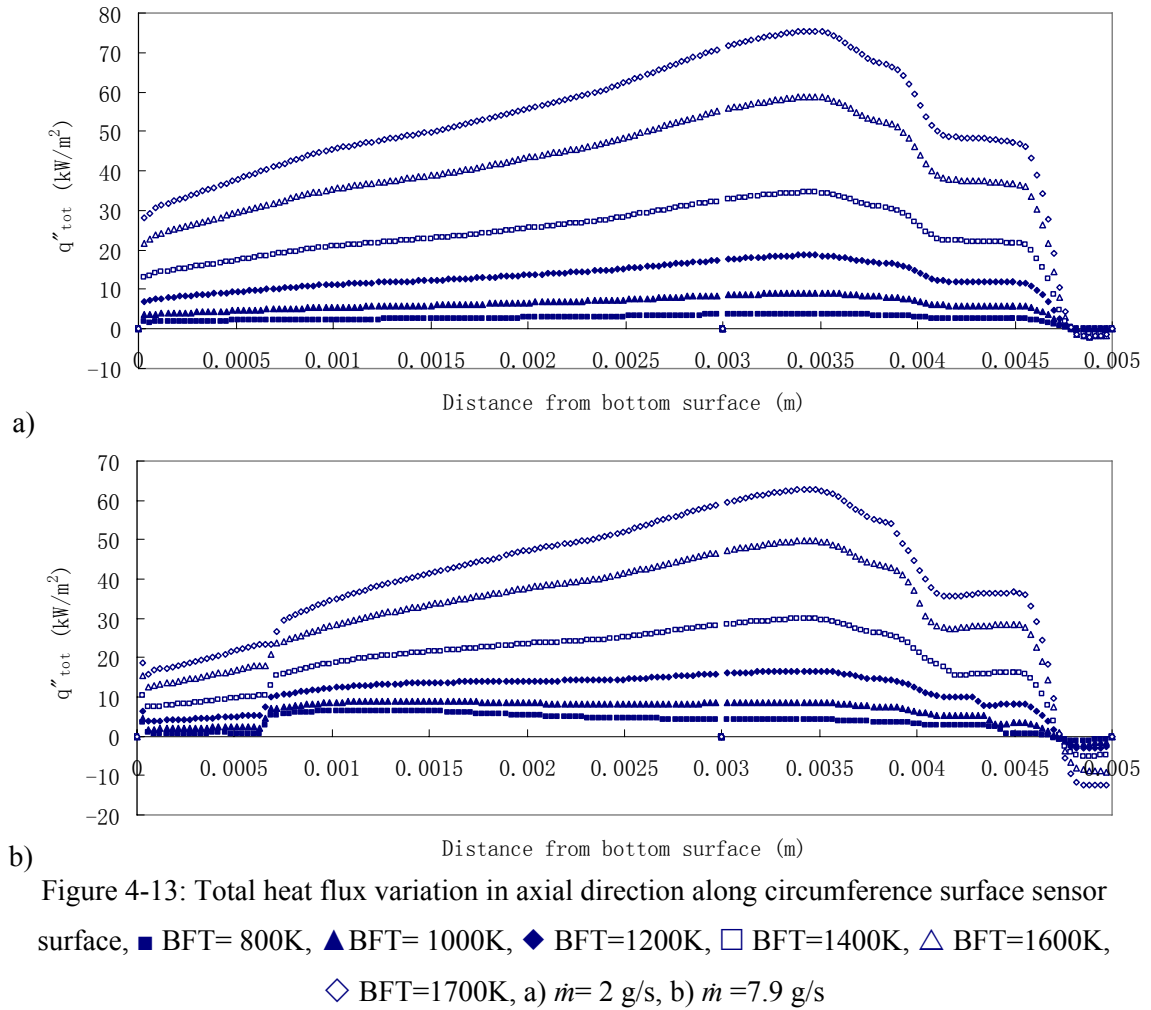


Figure 4-12: Total heat flux variation along the radius of the top sensor surface, ■ BFT= 800K, ▲ BFT= 1000K, ◆ BFT=1200K, □ BFT=1400K, △ BFT=1600K, ◇ BFT=1700K, a) $\dot{m} = 2$ g/s, b) $\dot{m} = 7.9$ g/s

The total heat fluxes are negative in these two plots, indicating that heat is transferred into the sensing element. As expected, the magnitude of the overall heat flux increases with the BFT. The shape of the heat transfer profile is fairly consistent over the range of heat flux levels tested. For the 2 g/s case, the magnitude of the total heat flux increases from the center to about 0.3mm away from the edge, then starts to decrease. For the 7.9 g/s case, the magnitude of the total heat flux increases consistently from the center to the circumference. Since the radiation heat transfer is almost constant along the radius, the plots shown above can also be seen as an indication of the convection heat transfer at the top surface. According to the plots, heat removed through convection is stronger at the center and weaker near the edge. However, the inflection seen near the edge of the sensing in the 2 g/s cases is not observed in the 7.9 g/s cases. This indicates that

the air flow rate change not only affects the magnitude of the convection heat transfer but also slightly alters its pattern. The variations of the total heat flux at the circumference surface in the axial direction are shown in Figure 4-13.



The values of the total heat flux are positive in these two plots, indicating the heat is removed from the sensing element at the circumference surface. As expected, the magnitude of the total heat flux also increases with the BFT and their profiles also remain fairly consistent over the tested heat flux range. In both cases, the magnitude of the total heat flux increases steadily for the first 3.5mm from the bottom of insulation layer. It then starts to decrease and even becomes negative near the top surface of the sensing element. This decrease in magnitude is caused by the increase in the amount of radiation heat flux absorbed by the circumference surface near the exit

of the channel. Deep in the annular channel the radiation heat flux is very weak because the view factor is small. However, near the channel exit, the circumference surface has more exposure to the radiation source: the top pressure outlet boundary. Although the convection heat transfer coefficient in the annular channel should increase with the air flow rate, the magnitude of the heat flux is actually lower in the 7.9 g/s cases. This is because of the stronger cooling effect of higher air flow rate reduces the amount of heat received at the top surface which leads to less amount of heat leaving the circumference surface following the conservation of energy. The sudden jumps can be seen in Figure 4-13 b) at about 0.0007m from the bottom surface. This is likely caused by the large recirculation bubble at the inlet of the annular channel under the high air flow rate which pushes the flow reattachment point further downstream and hence creates a jump in total heat flux. The circumference surface in the model was represented by two connected line. The shared point of these two lines caused the breaking points shown in the plots at 0.003m from the bottom surface. Figure 4-14 illustrates the temperature variations in the radial direction at the bottom surface of the sensing disc.

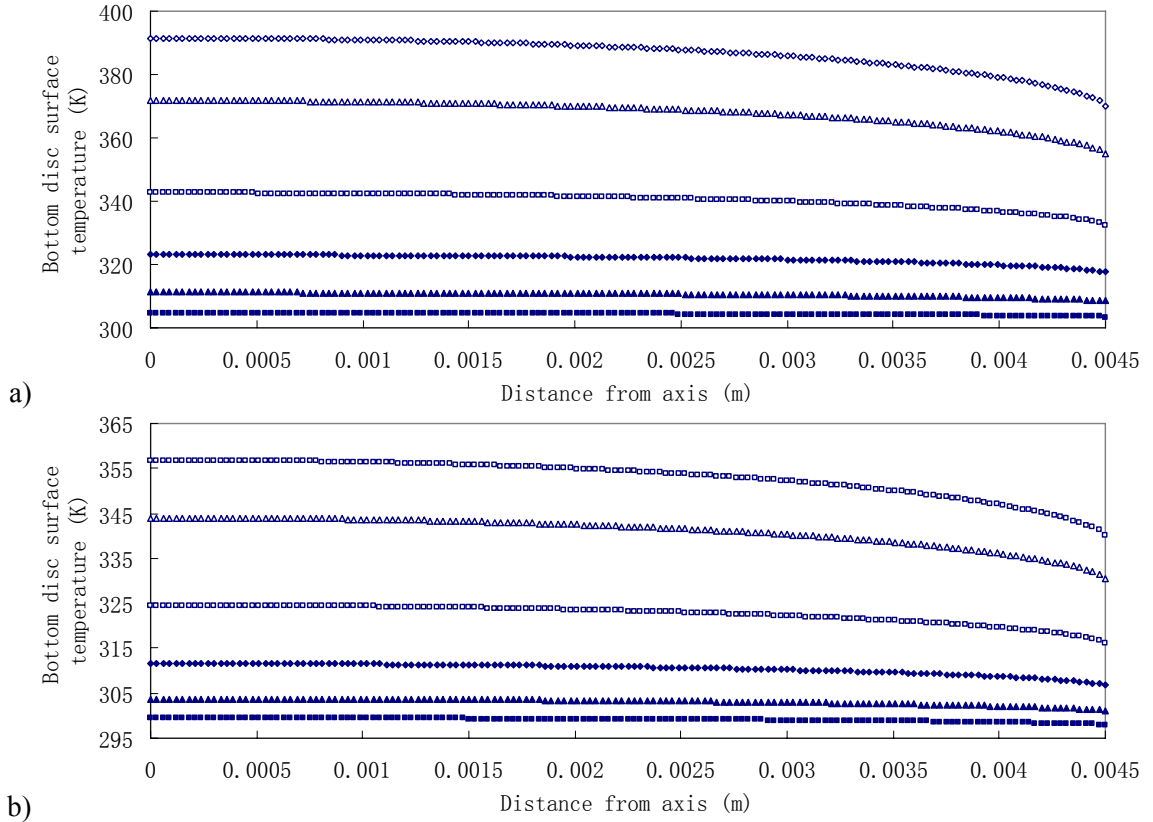


Figure 4-14: Temperature variation in radial direction at the bottom surface of the sensing element, ■ BFT= 800K, ▲ BFT= 1000K, ◆ BFT=1200K, □ BFT=1400K, △ BFT=1600K, ◇ BFT=1700K, a) $\dot{m}= 2$ g/s, b) $\dot{m}=7.9$ g/s

Despite the difference in the heat flux profiles the temperature profiles under the two air flow rates remain very similar and differ only in magnitude. The overall temperature of the sensor is always lower at the higher air flow rate, indicating a stronger overall convection cooling effect. In both cases, temperature decreases consistently from the center to the periphery of the disc bottom surface. The temperature gradient is smaller near the center and rises near the periphery. The differences between the temperatures at two ends of the plots are regarded as the RTD for each case and the results are plotted against the incident radiation heat fluxes as shown in Figure 4-15. Linear approximation is applied to the two sets of results to find out the sensitivity of the RTD method under each air flow rate.

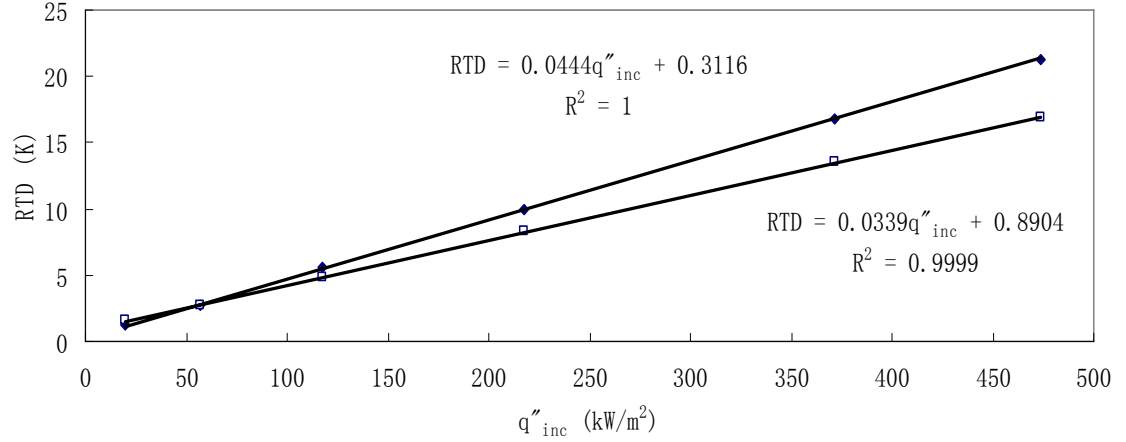


Figure 4-15: Sensitivity for RTD method (1mm channel), $\blacklozenge \dot{m}=2\text{g/s}$, $\square \dot{m}=7.9\text{g/s}$

According to the linear equations shown above, when the air flow rate is 2 g/s the relationship between the incident radiation heat flux and the RTD can be expressed as:

$$q''_{inc} = 22.52RTD - 7.02 \quad 4-26$$

$$X_{RTD} = 0.0444, \frac{1}{X_{RTD}} = 22.52$$

When the air flow rate is 7.9 g/s, the relationship becomes

$$q''_{inc} = 29.5RTD - 26.27 \quad 4-27$$

$$X_{RTD} = 0.0339, \frac{1}{X_{RTD}} = 29.5$$

In both cases, the numerical results showed a strong linearity between the incident radiation heat flux and RTD and the sensitivity of the RTD method decreases with increasing air flow rate.

Steady State Results (0.5mm channel)

For the sensor with 0.5mm channel, the path line of the air flow in the annular channel is shown in Figure 4-16 and the path line of the air flow near the top surface of the sensor is shown in Figure 4-17.

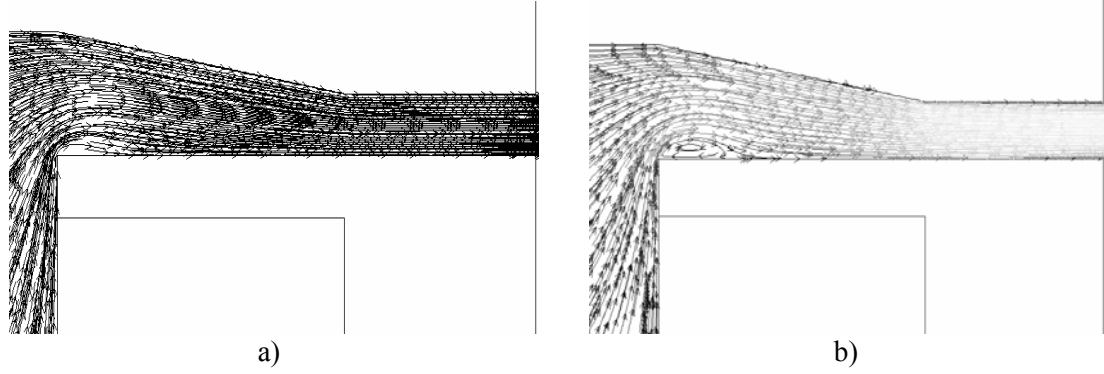


Figure 4-16: Path line in the annular channel a) $\dot{m}=0.95$ g/s, $Re=7071$, b) $\dot{m}=3.8$ g/s, $Re=28282$

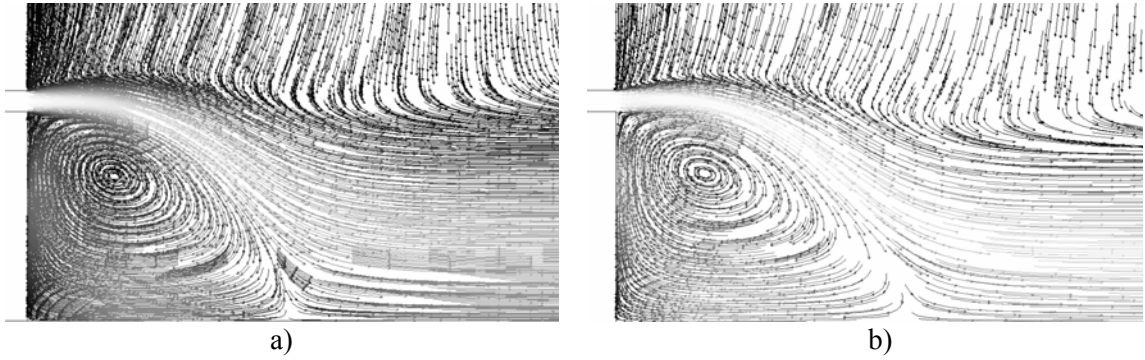
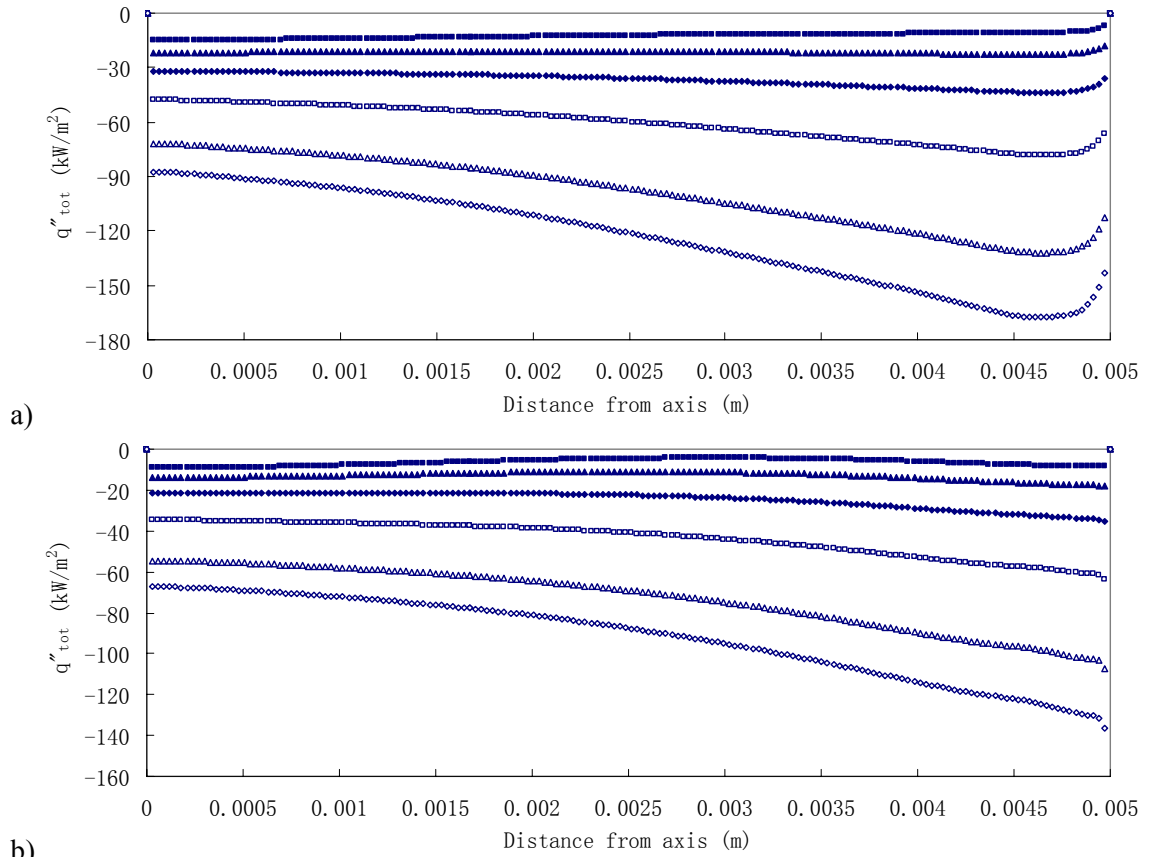


Figure 4-17: Center recirculation zone, a) $\dot{m}=0.95$ g/s, $Re=7071$, b) $\dot{m}=3.8$ g/s, $Re=28282$

Same as in the 1 mm channel case, the size of the recirculation bubble is slightly increased at higher flow rate. But comparing with the recirculation bubble shown in Figure 4-10, the ones in the 0.5 mm channel are smaller since the air flow rate was effectively halved while the inlet of the annular channel was remained at the same size. Also, the inner wall of the casing is tilted towards the sensing element, which prompted the flow reattachment in the channel. The overall air flow pattern in front of the sensing element resembles the ones shown in Figure 4-11. However the annular jet is bent more rapidly towards the center axis and hence the axial lengths of the CRZs become smaller. Based on the numerical results, at 0.95 g/s ($Re \approx 7000$) air flow rate, the axial length of the CRZ is about $0.45 D_o$ (0.5cm) and at 3.8 g/s ($Re \approx 28000$) air flow rate, its axial length increases to approximately $0.55 D_o$ (0.6cm).

The variations of total heat flux at the top surface along the radius of the sensing element in this sensor configuration are shown in Figure 4-18, and Figure 4-19 illustrate the variation of the total heat flux at the circumference surface in the axial direction.



b) Figure 4-18: Total heat flux variation along the radius of the top sensor surface, ■ BFT= 800K, ▲ BFT= 1000K, ◆ BFT=1200K, □ BFT=1400K, △ BFT=1600K, ◇ BFT=1700K, a) $\dot{m}= 0.95$ g/s, b) $\dot{m}=3.8$ g/s

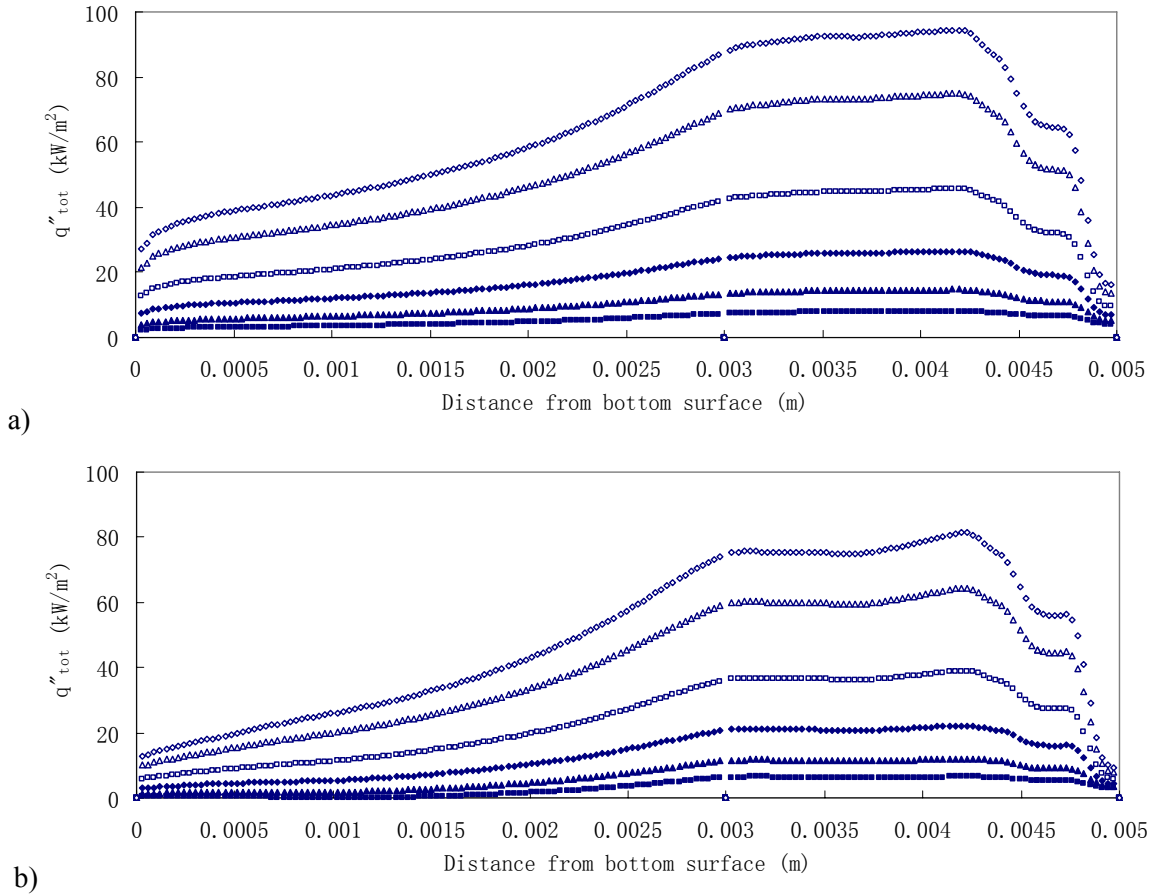


Figure 4-19: Total heat flux variation in axial direction along circumference surface sensor surface, ■ BFT= 800K, ▲ BFT= 1000K, ◆ BFT=1200K, □ BFT=1400K, △ BFT=1600K, ◇ BFT=1700K, a) $\dot{m}=0.95$ g/s, b) $\dot{m}=3.8$ g/s

Comparing with the 1mm channel cases, under both higher and low air flow rates, the magnitudes of the heat fluxes at the top and circumference surfaces are greater, indicating weaker convection at the top surface of the sensing element compared with the counterparts in the 1mm channel case. Same as in the 1mm channel case, the magnitude of the heat flux is lower in the 3.8 g/s cases than in the 0.95g/s case due to the stronger cooling effect at the top surface at higher flow rate which leads to less amount of heat leaving the circumference surface according to the conservation of energy. The overall heat transfer patterns at the top and circumference are similar to those of the 1mm channel case. The profiles of the heat flux variation remain consistent and the magnitudes increase with the BFT. The air flow rate also has a similar influence on the heat transfer pattern.

Under the lower air flow rate, 0.95 g/s, the inflection can be seen in the heat flux profiles at the top surface, especially at higher BFT. Under the higher air flow rate, 3.8 g/s, the heat flux decreases consistently from the center to the edge of the element, same as in the 7.9 g/s case shown earlier. The heat flux profile of the circumference surface under 3.8 g/s did not show the sudden jumps found in the 7.9 g/s case near the inlet of the annular channel. It is possibly due to the smaller recirculation bubble at the channel inlet as shown in Figure 4-16 b), which leads to smoother air flow and hence convection heat transfer profile near the channel inlet. On the other hand, the influence of radiation also appears near the exit of the channel. However, decrease in total heat flux only happens at about 0.75 mm upstream of the channel exit while in the 1mm channel case the distance is about 1.5mm. This is because the smaller annular gap blocks more radiation from coming into the channel than in the 1mm channel case. The resulting temperature variations in radial direction at the bottom surface of the sensing element are shown in Figure 4-20.

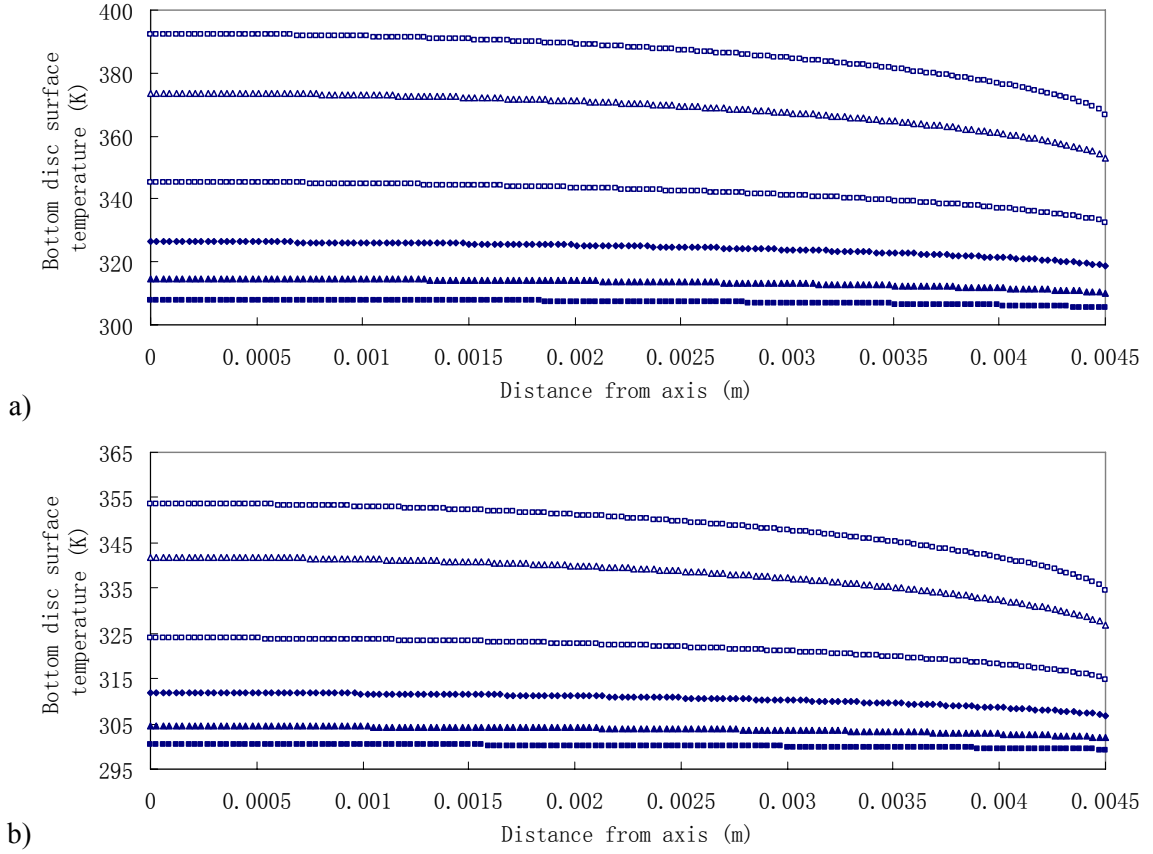


Figure 4-20: Temperature variation in radial direction at the bottom surface of the sensing element, ■ BFT= 800K, ▲ BFT= 1000K, ◆ BFT=1200K, □ BFT=1400K, △ BFT=1600K, ◇ BFT=1700K, a) $\dot{m}= 0.95$ g/s, b) $\dot{m}=3.8$ g/s

Although the air flow rate was halved, the overall temperature of the sensing disc did not change much. The temperature profiles also have the same shapes as the ones in the 1mm channel case. The temperature decreases consistently from the center to the periphery of the bottom surface of the sensing disc and its gradient is low at the center and gradually increases near the periphery. The plots of the RTD against the incident radiation heat fluxes in this case and their corresponding linear approximation functions are shown in Figure 4-21.

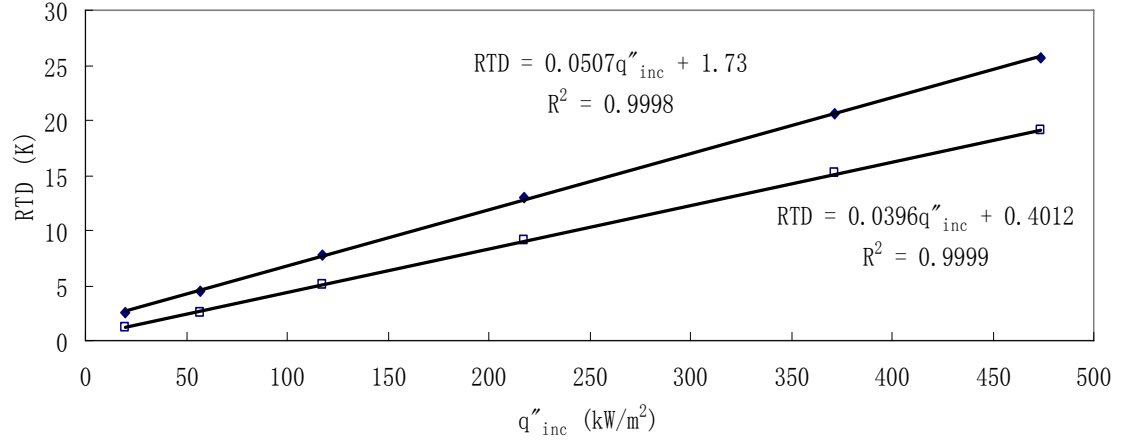


Figure 4-21: Sensitivity for RTD method (0.5mm channel), $\blacklozenge \dot{m}=0.95$ g/s, $\square \dot{m}=3.8$ g/s

According to the linear equations shown above when the air flow rate is 0.95 g/s the relationship between the incident radiation heat flux and the RTD can be expressed as:

$$q''_{inc} = 19.72RTD - 34.1 \quad 4-28$$

$$X_{RTD} = 0.0507, \frac{1}{X_{RTD}} = 19.72$$

When the air flow rate is 3.8 g/s, the relationship becomes

$$q''_{inc} = 25.25RTD - 10.13 \quad 4-29$$

$$X_{RTD} = 0.0396, \frac{1}{X_{RTD}} = 25.25$$

Similar to the 1mm channel case, the numerical results showed linear relationships between the incident radiation heat fluxes and the RTD under the two air flow rates, and again, the sensitivity of the RTD method decreases with increasing air flow rate.

Transient Simulation Results (1mm channel)

The behavior of the “clean” heat flux sensor under oscillating air flow rates was studied using unsteady state simulations. The time variations of surface heat fluxes and sensor temperature (T_c) were obtained. The data recording interval for the simulations is 0.5 second, matching the data acquisition parameter in the experiment. The results shown in this section were obtained under

1000K BFT which produces an incident radiation heat flux of 56.7 kW/m^2 at the sensor surface. As mentioned previously, sinusoidal air flow rate with 80 seconds oscillation period was used in these final models. Figure 4-22 illustrates the mass flow rate oscillation in kg/s.

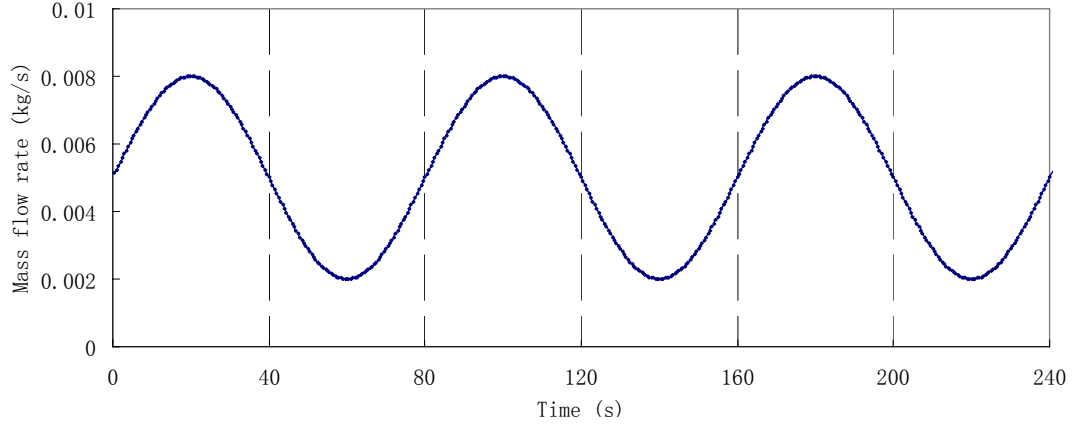


Figure 4-22: Air flow rate oscillation (1mm channel)

As shown above, the mass flow rate oscillates sinusoidally between 2 and 7.9g/s and the starting point is the mean mass flow rate. At its initial state, the simulation domain, including the sensing element, is in thermal equilibrium with uniform temperature at 300K. Therefore, the results from each unsteady state simulation in fact illustrate the behaviors of the variables under a step change heat flux. As will be shown in the following plots, the results in the first half period are affected by the initial sudden heat flux increase and hence appear to behave differently.

Due to the existence of the insulation layer, the heat transfer at the bottom surface of the sensing element was considered relatively insignificant and was not recorded in the simulation. However, it was later realized that there was in fact a fair amount of heat transferred through the bottom surface. Since the heat flux transferred through the bottom surface of the sensing element was not recorded, change in internal energy is roughly estimated based on the T_c recorded (Equation 4-30).

$$\Delta E_{net}(t) = [(\rho V c_p)_{in} + (\rho V c_p)_{st}] [T_c(t) - T_c(0)] \quad 4-30$$

where ρ is the density V is the volume, *in* denotes the insulation material and *st* denotes steel, the temperature of the sensing element is approximated by T_c . The oscillation of the net internal

change and T_c are shown in Figure 4-23.

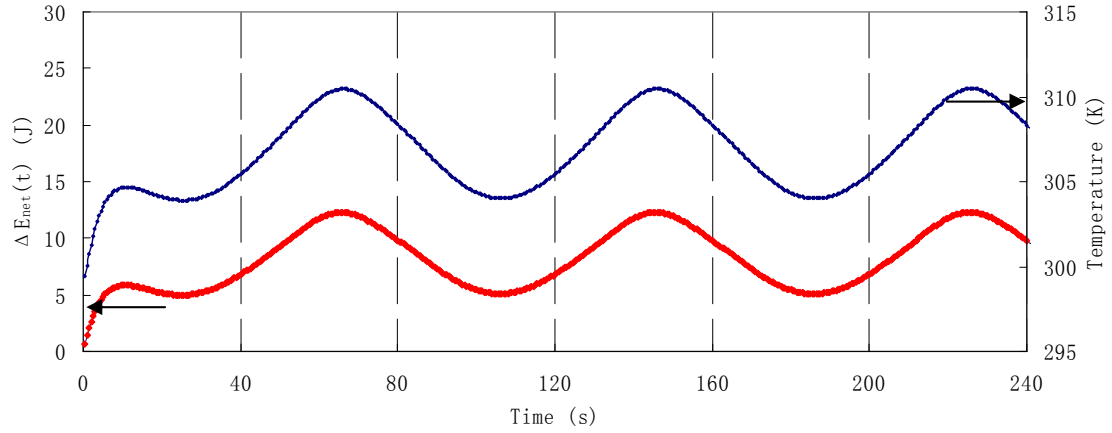


Figure 4-23: Estimated net internal energy and the corresponding T_c oscillation (1mm channel),
 ◆ Net internal energy change, ■ T_c

The change of internal energy starts at 0 indicating that the system is in equilibrium initially. The sudden increase in internal energy at the first 10 seconds of the simulation is caused by the net heat influx when the sensor is subjected to the sudden radiation heat flux. The corresponding T_c oscillation shown in Figure 4-23 appears to have stabilized within the first half period. This indicates that the response time of the T_{dc} component is relatively short compared with the 80 seconds oscillation period. The lag between the T_c oscillation and the oscillation of air flow rate is approximately 6 seconds. The heat transfer rate at the bottom surface can then be estimated using Equation 4-31

$$\frac{d\Delta E_{net}(t)}{dt} = q'_{tot-top}(t) - q'_{tot-cir}(t) - q'_{tot-bot}(t) \quad 4-31$$

$$q'_{tot-bot} = q'_{tot-top} - q'_{tot-cir} - \frac{d\Delta E_{net}}{dt}$$

$$(q'_{tot-surf} = q''_{tot-surf} A_{surf})$$

where $tot-surf$ denotes the total heat flux or heat transfer rate at the corresponding surface. The minus sign in Equation 4-31 indicates the heat is considered to be removed at the circumference and bottom surface and absorbed at the top surface. The oscillations of the total heat transfer rate

at the top, circumference (recorded from the simulation) and the bottom surfaces (calculated through Equation 4-31) as well as the rate of the internal energy change ($d\Delta E_{int}/dt$) are shown in Figure 4-24.

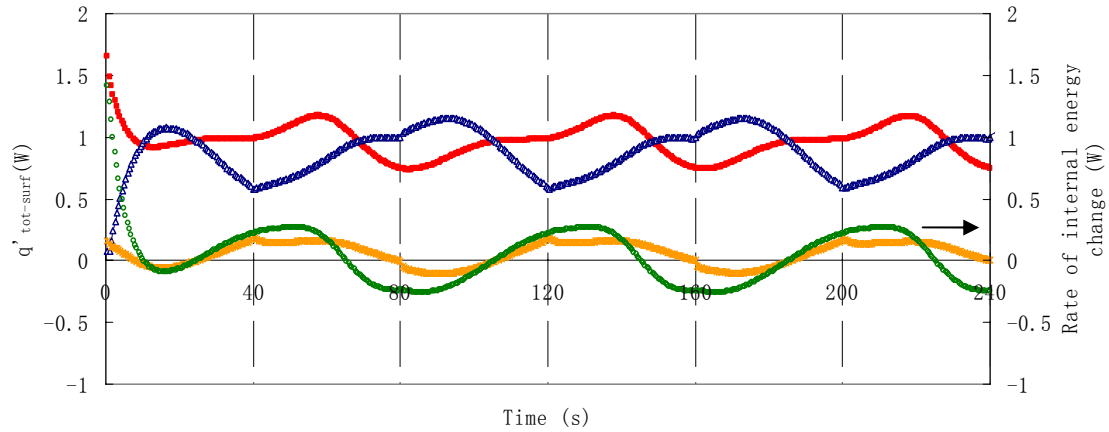


Figure 4-24: Oscillation of the total heat transfer rate oscillation at the top, circumference and bottom surfaces and rate of internal energy change (1mm channel),

$$\blacksquare q'_{top}, \triangle q'_{cir}, * q'_{bot}, \circ d\Delta E_{int}/dt$$

As shown above, the overall magnitude of the heat transfer rate at the bottom surface is smaller than those at the top and circumference surfaces. The heat transfer rate through the bottom surface appears to oscillate about 0W, which indicates that the bottom surface is cooled at lower air flow rate and heated at higher air flow rate. The change of heat flux at the top surface is relatively smooth while abrupt changes in the oscillation of heat transfer rate at the circumference surface can be seen every half period when the air flow rate reaches its mean value. The exact cause of these changes is unclear but is likely related to the variation in energy calculation in FLUENT as the flow velocity changes. The issue reflects the drawbacks of using an existing modeling tool that it is difficult to find out the source that leads to the unusual results. The estimated rate of internal energy change is rather smooth despite the abrupt changes shown in the oscillation of heat transfer rate at the circumference surface. The A_c at each incident radiation heat flux level is summarized in Figure 4-25. Same as the RTD method, linear approximation is

applied to estimate the sensitivities of the oscillation method with this sensor configuration.

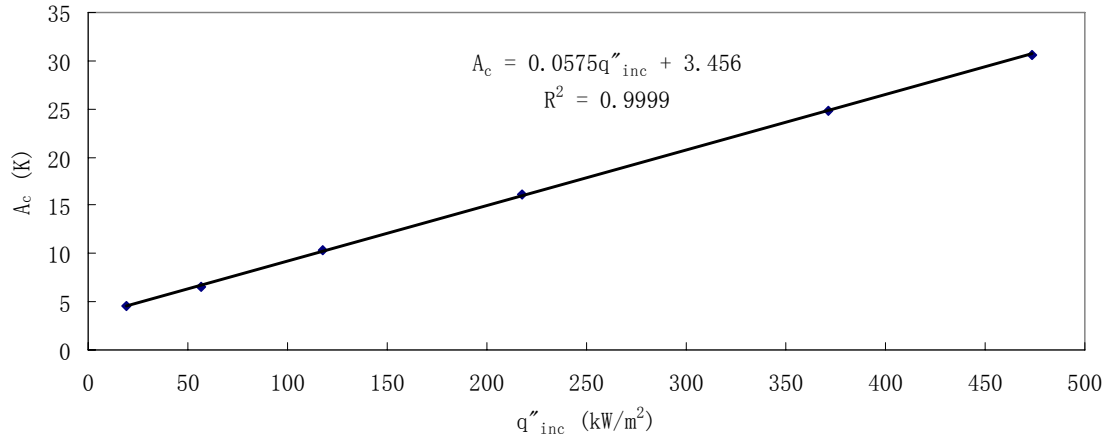


Figure 4-25: Sensitivity of the oscillation method (1mm channel)

The sensitivity appears to be consistent over the tested heat flux range. According to the linear equations shown in the above plots, the incident radiation heat flux can be expressed in terms of the A_c as:

$$q''_{inc} = 17.39A_c - 60.1 \quad 4-32$$

$$X_{A_c} = 0.0575, \frac{1}{X_{A_c}} = 17.39$$

The large constant in Equation 4-32 indicates that the amplitude of the temperature oscillation is not 0 at ambient environment. This is because the temperature of air surrounds the sensing element changes with the air flow rate as a result of considering the compressibility of the air.

Transient Simulation Results (0.5mm channel)

The results of the 0.5mm channel case obtained also under 1000K BFT are shown in this section.

Figure 4-26 illustrates the mass flow rate oscillation in this case.

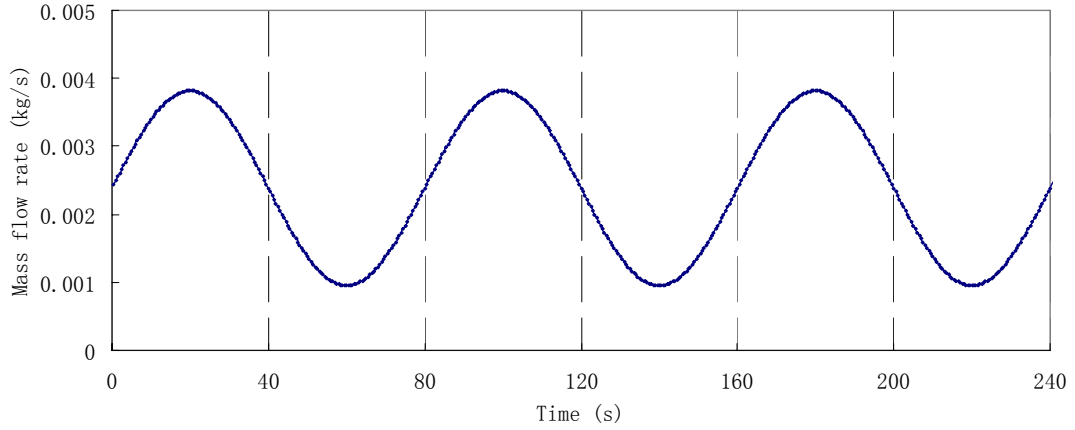


Figure 4-26: Air flow rate oscillation (0.5 mm channel)

As shown above, the mass flow rate oscillates sinusoidally between 0.95 and 3.8g/s and the starting point is also the mean mass flow rate. Again, using Equation 4-30, the net internal energy change is estimated and shown in Figure 4-27 along with the recorded T_c oscillation.

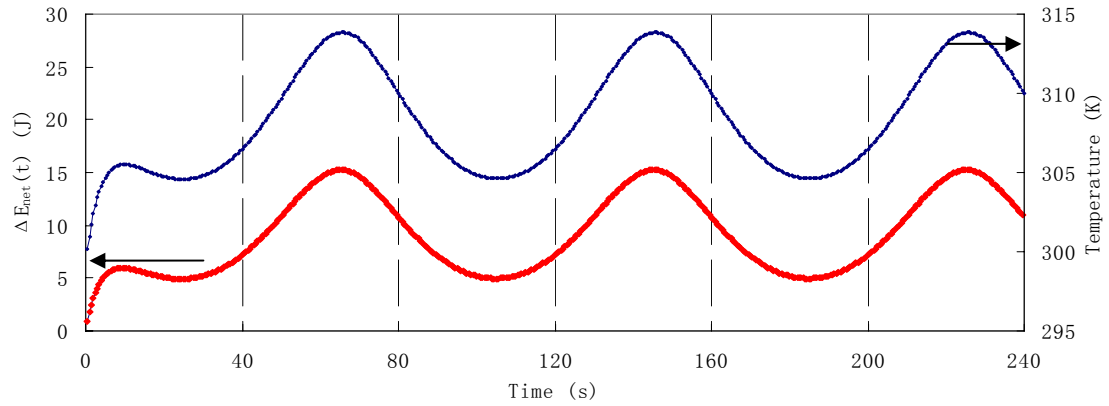


Figure 4-27: Estimated net internal energy and the corresponding T_c oscillation (0.5 mm channel),
 ◆ Net internal energy change, ■ T_c

Compared with the 1mm channel case, the amplitude of the T_c oscillation is greater which leads to a larger internal energy change oscillation. The shape of the T_c oscillation curve differs slightly from that of the 1mm channel case with its bottoms more rounded and tips sharper. The lag between the T_c oscillation and the air flow oscillation is about 5.5 seconds. Again, using Equation 4-31, the change of the total heat transfer rate at the bottom surface is estimated and

plotted in Figure 4-28 along with the values recorded at top and circumference surfaces and the rate of the net internal energy change.

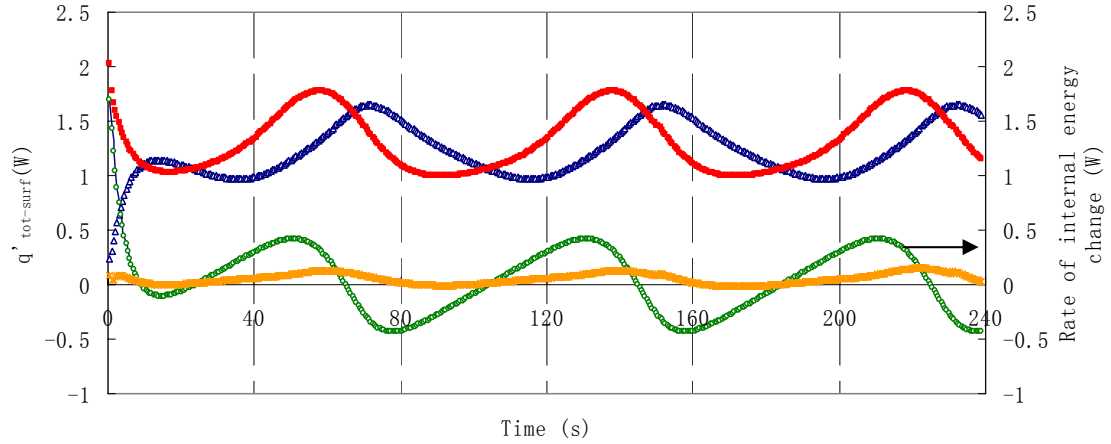


Figure 4-28: Total heat flux oscillation at the top and circumference surfaces (0.5 mm channel),

$$\blacksquare q'_{top}, \triangle q'_{cir}, * q'_{bot}, \circ d\Delta E_{net}/dt$$

The shapes of the heat transfer rate curves in this case are quite different from the ones shown earlier and no abrupt change can be seen in the oscillation curve of the heat transfer rate at the circumference surface. Similar to the 1mm channel case, the magnitude of the heat transfer rate at the bottom surface is smaller than those at the top and circumference surfaces and its value oscillates mainly above 0 as the air flow rate varies indicating the surface is being cooled most of the time. The A_c at each heat flux level is summarized in Figure 4-29 and the sensitivity of the oscillation method with this sensor configuration is again estimated by the linear approximation equation shown in the plot.

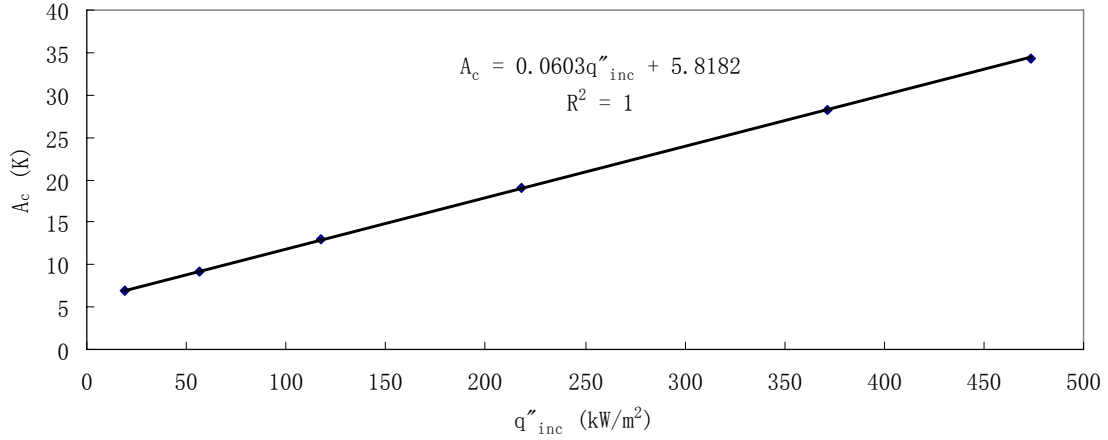


Figure 4-29: Sensitivity of the oscillation method (0.5 mm channel)

According to the linear equations shown above, the incident radiation heat flux can be expressed in terms of the A_c as:

$$q''_{inc} = 16.58A_c - 96.49 \quad 4-33$$

$$X_{A_c} = 0.0603, \frac{1}{X_{A_c}} = 16.58$$

Compared with the result of the sensor with 1mm channel, the sensitivity of the oscillation method is higher in this case. It also appears to be consistent over the tested heat flux range. Based on the numerical results, with the flow configurations used in the tests, the sensitivity of the amplitude method is always greater than that of the RTD method. However, in terms of consistency, both method appear to be unaffected by the change in the thermal properties of the sensing disc as a result of elevated incident radiation heat flux.

Chapter 5 Experimental Study and Results

The main objective of the experimental analysis was to test the two measurement methods of the “clean” heat sensor and estimate their actual sensitivities under various flow conditions. The data processing procedures described in Chapter 3 were applied to the raw experimental results obtained under steady and unsteady incident radiation heat fluxes. The relationship between the “dirty” heat flux sensor and the incident radiation heat flux was also estimated.

5.1 Apparatus and Setup

As described in Chapter 3, the “clean” sensor operates with air and the “dirty” sensor operates with water. Tap water was used as the water supply for the “dirty” sensor. Figure 5-1 illustrates the overall layout of the experiment.

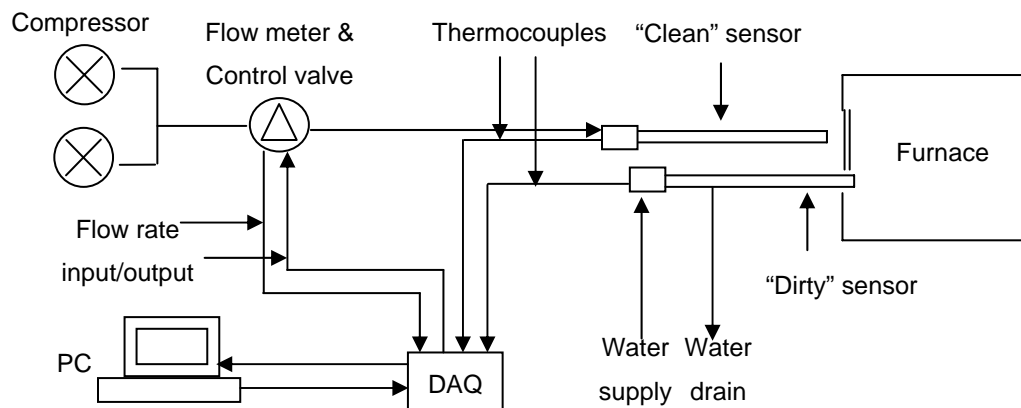


Figure 5-1: Layout of the experiment setup

The air flow rate is controlled by the computer through the data acquisition board (Measurement Computing Corp, model USB 2614-4AO). Simultaneously, the board also transfers the temperature readings from the thermocouples of the two sensors and the mass flow rate data from the flow meter to the computer. The air supply was provided by two air compressors connected in parallel to reach the air flow rate required in the experiment. The maximum pressure for each compressor is 135 psi and the maximum volume flow rates are 6.5 SCFM (3.7g/s) and 5.5 SCFM

(3.1g/s) at 40 psi and 90 psi respectively. The two air supply lines were connected to a buffer tank that was placed prior to the flow meter to further stabilize the air pressure. The air flow into the “clean” sensor was measured and controlled by an Omega FMA 5500 mass flow meter, which has a maximum allowable air flow rate of 500SLM (9.9g/s). The flow rate was controlled by the motorized valve incorporated within the flow meter which was remotely operated by the data acquisition board with a 0 to 5 VDC analog signal. The closed loop control circuit of the flow meter continuously compared the mass flow output with the set flow rate and the valve was adjusted to correct the deviations from the set flow rate. The output and input voltages are a linear representation of 0 to 100% of the full scale mass flow rate. The response time to set point changes is 5 seconds within 2% of the final flow over 25% to 100% of full scale. During the tests, the “clean” and “dirty” heat flux probes were held together in tandem (Figure 5-2 a) by two aluminum brackets (Figure 5-2 b).

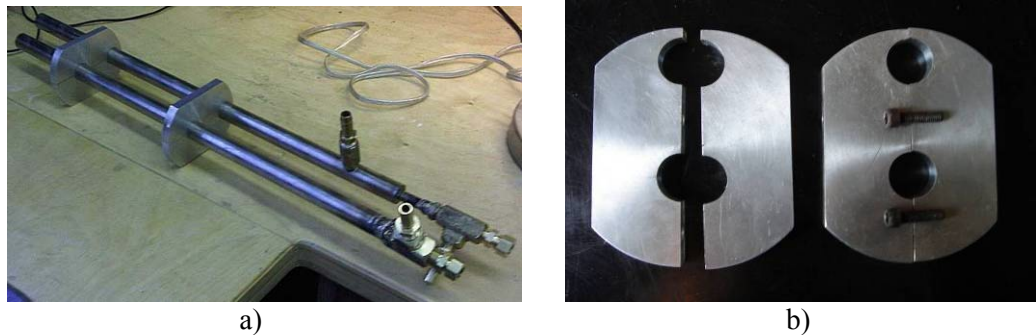


Figure 5-2: Two heat flux probes a) held together by b) two aluminum brackets

To calibrate heat flux sensors that are to be used in high temperature conditions, it is preferred to have a well controlled radiation source with a heat flux range that is similar to the one in the supposed operation environment. However, lab scale testing often can not reach the heat flux levels in industrial boilers. The sensor is usually calibrated under a lower heat flux range and operates by extrapolation and the sensitivity is often assumed to be the same in the operation heat flux range. In terms of selecting the calibration device and procedure, there is currently no international standard [46]. Several laboratories and manufactures have attempted different

techniques. National institute of standard and technology (NIST) employs a spherical blackbody furnace approach, as shown in Figure 5-3.

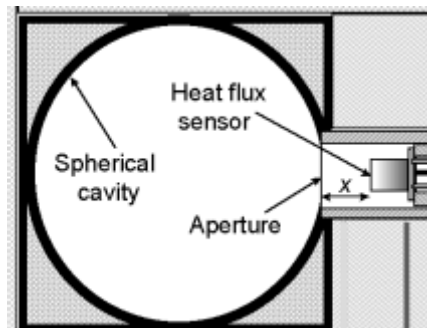


Figure 5-3: Spherical blackbody furnace [47]

The radiation emitted from the aperture could simulate a blackbody radiation source given the size of the aperture is relatively small compared with the volume of the spherical cavity. The effective emissivity of this type of radiation source is determined by the emissivity of the cavity surface and the angle of the aperture as shown in Figure 5-4.

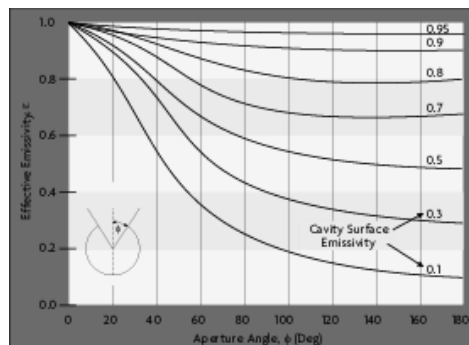


Figure 5-4: Effective emissivity of spherical cavities [48]

The effective emissivity of the radiation source approaches 1 as the surface emissivity increases and the aperture angle decreases. The producer of the Gardon gage Vatel Corporation employs a dual-cavity black body made of a double ended graphite tube with a center partition. The temperature of the body is measured using a NIST-traceable pyrometer at one end, and the gauge being calibrated is inserted from the other end. By adding a graphite extension at each end of the dual-cavity black body cavity, Murthy, et al [49] managed to calibrate the Schmidt-Boelter heat

flux sensor up to 100kW/m^2 with a black body temperature of roughly 2700K . The apparent difference between the resulting incident radiation heat flux and the ones shown in Table 4-2 is due to the small view factor between the radiation source and the sensor surface in their experiment which drastically limited the radiation heat flux received by the sensor. More recently, Filtz, et al [50] tested a vacuum black body cavity in an attempt to reduce the calibration uncertainties for heat flux densities lower than 20kW/m^2 . For the Gardon gage, thermal balance calibration method, with which the absorbed heat flux is estimated based on the temperature change and the mass flow rate of the coolant-water, was experimented by Ballestrin, et al [47, 52]. The radiation heat flux in their experiment was generated by passing electric current through a graphite plate which was also monitored by a pyrometer. The maximum heat flux reached was 100kW/m^2 . The water flow rate was measured by an electromagnetic flow meter.

However, these calibration techniques were all designed for the traditional heat flux sensor. Calibration of the “clean” heat flux sensor could be more challenging because of the interference on the heat source by the air jet. Afgan, et al [15], employed a 1kW halogen light as the radiation heat source. By using two converging lenses for radiation concentration, the maximum incident radiation heat flux achieved was reported to be 105kW/m^2 . Although the experiment setup might be more complicated, it successfully avoided the impact of the air jet on the radiation source. The radiation source used for calibrating the porous media type “clean” heat flux sensor was a black body radiator made of electrical-heated cylindrical sodium heat pipe [52]. However, no air jet blocking mechanism was mentioned in the paper, possibly because the low air velocity associated with the porous media sensor had little impact on the radiation source. In the present study, an Advance Kiln & Supplies high temperature front-load furnace (model AKL-1297) was used as the radiation source. The furnace has a rectangular cavity with a dimension of $31\text{cm.}(L) \times 23\text{cm.}(W) \times 18\text{cm.}(H)$ (Figure 5-5). The heating elements are embedded in the bottom and side surfaces of the cavity. The temperature limit of the furnace is 1100°C . The inner

walls of the furnace are made of fire clay which has a surface emissivity ranging from 0.56 to 0.85, depending on the source of information.



Figure 5-5: Rectangular cavity of the AKL-1297 furnace

The door of the furnace was modified so that the incident radiation heat flux can be approximated by using the chart in Figure 5-4 and also to create the supporting structure of the sensor tandem. A hole 3 inches in diameter was drilled on the furnace door, and an aluminum ring was attached on the outer surface of the furnace door as shown in Figure 5-6 a). The end of the hole was covered by a 1-inch thick insulation board as shown in Figure 5-6 b). Two circular openings aligned with the two heat flux probes were made on the insulation cover to allow radiation transmission.



a)



b)

Figure 5-6: Furnace door modification, a) outside view, b) inside view

To prevent the impact of the air jet from the “clean” heat flux sensor on the radiation source, while allowing maximum amount of the radiation heat flux to be received by the sensor, an

aluminum plate (Figure 5-7) was added at the front of the probe tandem. The plate had two circular openings that were also aligned with the two probes. The smaller opening, having a slightly larger diameter than the probe, could allow the “dirty” heat flux sensor to pass through. The plate could then be secured onto the “dirty” probe by the screws on the two sides of the plate (Figure 5-7 b). A sapphire disc was placed into larger opening, and was secured by a steel spring (Figure 5-7 b, c).

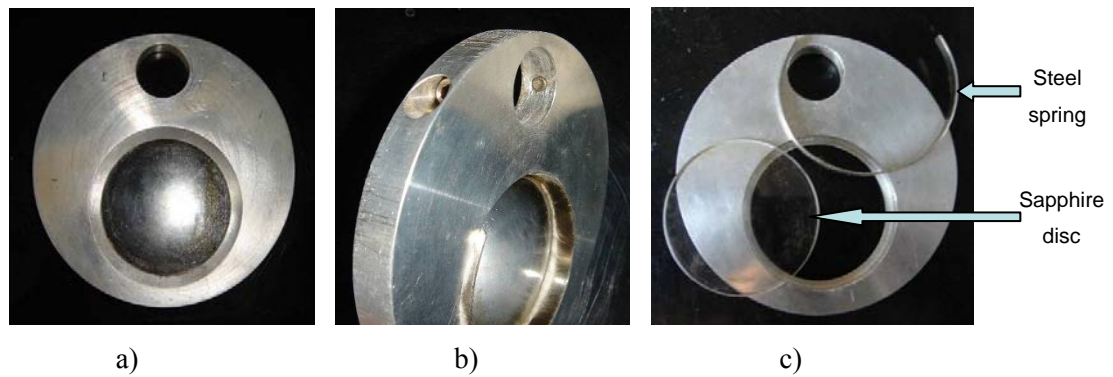


Figure 5-7: Front plate, a) front view, b) side view, c) disassembled

The sapphire window has a relatively high and flat transmissivity within a wide wavelength range (from 0.2 μm to 5 μm) as shown in Figure 5-8. Therefore, while the window can block the air jet, the majority of the radiation can still pass through and the calculation of the transmitted radiation is relatively simple.

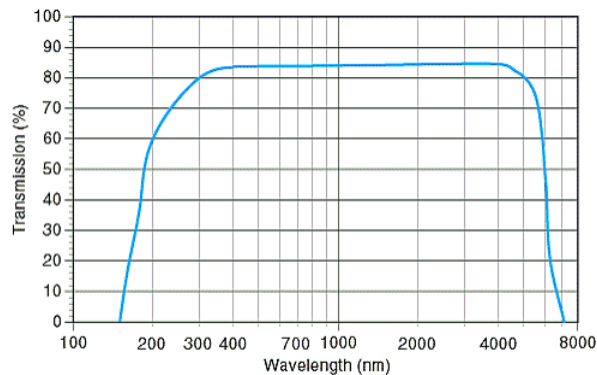


Figure 5-8: Spectral transmissivity of sapphire window [53]

An aluminum pipe was secured on the furnace door by the mounting device to provide support for the probe tandem. The probe tandem was inserted into the aluminum pipe until the front plate reached the insulation cover and the two openings were aligned with the ones on the cover. Figure 5-9 shows the position of the two heat flux sensors when the tandem was ready for testing.



Figure 5-9: Testing position of the sensors, a) outside view, b) inside view

The front surface of the “dirty” heat flux sensor was exposed directly to the radiation source and its circumference surface was surrounded by the insulation layer. The “clean” heat flux sensor was placed behind the sapphire window at a certain distance. The view factor between the sapphire disc and the “clean” sensor surface was estimated based on this distance and the sizes of the two surfaces.

5.2 Incident Radiation Estimation

As described in Chapter 2, several factors need to be considered when estimating the incident radiation heat flux on a surface: emissivity of the radiation source, transmissivity of the medium, and view factor. A few assumptions were made when estimating these factors in the experiment.

1) Although the shape of current radiation cavity is rectangular, the relationship between the effective emissivity, the aperture angle, and the surface emissivity of the cavity was assumed to be the same as that of a spherical cavity illustrated in Figure 5-4. As shown in Figure 5-4, the effective emissivity approaches one when the aperture angle decreases regardless of the

emissivity of the cavity surface. Therefore based on the parameter of the radiation source, its effective emissivity was assumed to be 0.9.

2) The incident radiation was estimated based only on the radiation transmitted through the sapphire window. Radiation emitted from the window and surroundings, and radiation reflection within the secondary cavity (the cavity formed by the aluminum pipe, front plate and aluminum brackets) were ignored. The transmissivity of the disc was assumed to be constant at 0.85 from 0.2 μ m to 5 μ m, and 0 at other wavelengths. Therefore, by using Equation 2-24 and 2-26, the percentage of radiation energy that passed through the sapphire disc was estimated.

3) The view factor between radiation source and the top surface of the “clean” heat flux sensor was assumed to be the same as the view factor between the sapphire window and the top sensor surface. Therefore, the view factor calculation was simplified to a parallel coaxial disc problem as illustrated in Figure 5-10.

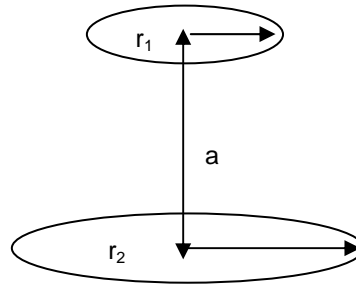


Figure 5-10: Disc to parallel coaxial disc of unequal radius

The view factor calculation shown in Equation 2-25 can then be replaced by Equation 5-1 to 5-3 [54].

$$F_{1 \rightarrow 2} = \frac{1}{2} \left\{ X - \left[X^2 - 4 \left(\frac{R_2}{R_1} \right)^2 \right]^{1/2} \right\} \quad 5-1$$

where R_1 and R_2 are calculated as:

$$R_1 = \frac{r_1}{a}, \quad R_2 = \frac{r_2}{a} \quad 5-2$$

where r_1 and r_2 are the radius of the two discs and a is the distance between the two parallel discs.

X is related to R_1 and R_2 by

$$X = 1 + \frac{(1 + R_2^2)}{R_1^2} \quad 5-3$$

Since the dimensions of the sapphire window and the sensing element were unchanged, the view factor was controlled by the sensor-to-window distance. Therefore, by using Equation 5-1 to 5-3, the view factors in each test were calculated and are shown in Table 5-1.

Table 5-1: Estimated view factors for each test

Test	Sensor-to-window distance (cm)	View Factor
T1	4.5	0.279
T2&4	2.5	0.495
T3&5	1.5	0.729

For the sensor with 1mm annular channel, it was tested at three different sensor-to-window distances: 4.5cm, 2.5cm, and 1.5cm (T1, T2, T3). For sensor with 0.5 mm annular channel, the sensor was tested at two different sensor-to-window distances: 2.5cm and 1.5cm (T4 and T5). Although smaller sensor-to-window distance would lead to higher incident radiation heat flux on the “clean” heat flux sensor, it has been shown in the numerical results that the axial length of the CRZ could be as long as 1cm. It is reasonable to believe that if the “clean” sensor was placed too close to the sapphire window, the air flow near the top sensor surface would likely be affected by the sapphire window. Hence the heat transfer at the top surface of the sensor would be significantly modified by the window. Therefore, the smallest sensor-to-window distance used in the experiment was 1.5cm. In each test, the sensor was tested at eight set temperatures, from 1000F to 1700F with 100F interval. In Table 5-2, the set temperatures in Fahrenheit and Kelvin are shown along with the percentages of the radiation transmitted through the sapphire window at each set temperature calculated by using Equation 2-26 and the spectral transmissivity provided in Figure 5-8.

Table 5-2: Estimated percentage transmitted radiation at each testing temperature

T(F)	T(K)	% Transmitted
1000	811	49.13%
1100	866	53.86%
1200	922	58.13%
1300	977	61.99%
1400	1033	65.45%
1500	1089	68.55%
1600	1144	71.33%
1700	1200	73.82%

By using Equation 2-28, which takes into account the view factors, the percentage transmitted radiation and the effective emissivity of the radiation source, the incident radiation heat fluxes at for each test at different set temperatures were calculated and are shown in Table 5-3.

Table 5-3: Estimated incident radiation heat flux for the “clean” sensor

T(F)	$q''_{inc} \text{ (kW/m}^2\text{)}$			
	Radiation source	T1	T2&4	T3&5
1000	22.08	3.02	5.36	7.90
1100	28.70	4.31	7.66	11.29
1200	36.88	5.97	10.61	15.63
1300	46.49	8.05	14.29	21.06
1400	58.11	10.60	18.82	27.74
1500	71.77	13.69	24.31	35.83
1600	87.40	17.38	30.87	45.50
1700	105.82	21.74	38.62	56.92

Although at the maximum test temperature, the furnace could produce roughly 106kW/m² of radiation heat flux, the amount received by the “clean” heat flux sensor was only slightly over half the value. Therefore, the calibration heat flux range for the “clean” sensor was in fact much lower compared with the heat flux in the boiler. For the “dirty” heat flux sensor, the sensor surface was exposed directly to the furnace cavity. Therefore, the view factor was essentially one and all the radiation heat flux produced was transmitted onto the sensor surface. Therefore the

incident radiation heat flux on the “dirty” heat flux sensor at the set temperatures is basically the heat flux of the radiation source listed in Table 5-3.

5.3 Experimental Results

The experimental results shown in are mostly from T2 and T4. The experiment codes consist of two parts, the primary part indicates the test number and air flow pattern, while the secondary part indicates the condition of the radiation source. Table 5-4 lists the configurations and codes of the calibration experiments conducted.

Table 5-4: Configurations of the experiments and the corresponding codes

Experiment code		Air flow rate pattern	Furnace temperature (F)	Annular channel width (mm)	Lower/upper air flow rate (g/s)	View factor
Primary	Secondary					
T1-c	1000 to 1700	constant	1000-1700	1	2/7.9	0.279
T1-s	1000 to 1700	sinusoidal	1000-1700			
T2-c	1000 to 1700	constant	1000-1700	1	2/7.9	0.495
T2-s	1000 to 1700	sinusoidal	1000-1700			
T3-c	1000 to 1700	constant	1000-1700	1	2/7.9	0.729
T3-s	1000 to 1700	sinusoidal	1000-1700			
T4-c	1000 to 1700	constant	1000-1700	0.5	0.95/3.8	0.495
T4-s	1000 to 1700	sinusoidal	1000-1700			
T4-s	heating		Heating			
T4-s	cooling		Cooling			
T5-c	1000 to 1700	constant	1000-1700	0.5	0.95/3.8	0.729
T5-s	1000 to 1700	sinusoidal	1000-1700			

For each channel size and flow configuration, one set of results, including air flow rate, “dirty” sensor temperature difference, the “clean” sensor temperatures, T_c , T_p and RTD (only in constant air flow cases), are presented. The sensitivities of the sensors when operating under the RTD method and the oscillation method are concluded based on collective test results. The two air flow rates used for the 1mm channel were 2 g/s and 7.9 g/s, while for 0.5mm channel they were 0.95 g/s and 3.8 g/s. The RTD method was tested under these four air flow rates with the

corresponding channel. These four air flow rates were also the maximum and minimum values for the oscillating air flow rates. In all five tests shown here, the flow oscillation period used was 80 seconds.

5.3.1 Steady Radiation Heat Flux

For the RTD method, the results shown below are from T2 and T4, both under 1700F furnace temperature and with the same sensor-to-window distance. Therefore, the estimated incident radiation heat fluxes were the same, at 38.62 kW/m^2 . The results of the oscillating method shown here were also obtained from these two cases.

Constant Air Flow Rate (1mm channel)

Figure 5-11 shows the air flow rate signals recorded when the flow rate was set at 2 g/s and 7.9 g/s respectively.

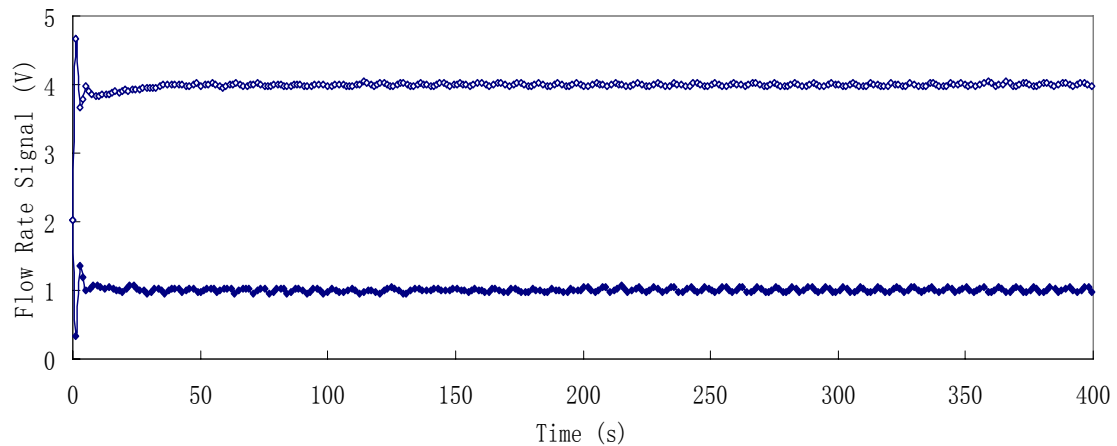


Figure 5-11: Air flow rate signals (T2-c-1700), $\blacklozenge \dot{m}=2\text{g/s}$, $\square \dot{m}=7.9\text{g/s}$

As shown above, the air flow rate signals stay at 1V and 4V respectively when the air flow rate is 2 g/s and 7.9 g/s. Noticeable jumps can be observed at the beginning of the plots of the signal and then quickly stabilizes towards the set air flow rate. However, small fluctuations can be seen throughout the testing period which might have partially contributed to the temperature

fluctuations at the “clean” heat flux sensor as will be shown later. Figure 5-12 illustrates the “dirty” sensor temperature differences during these two tests.

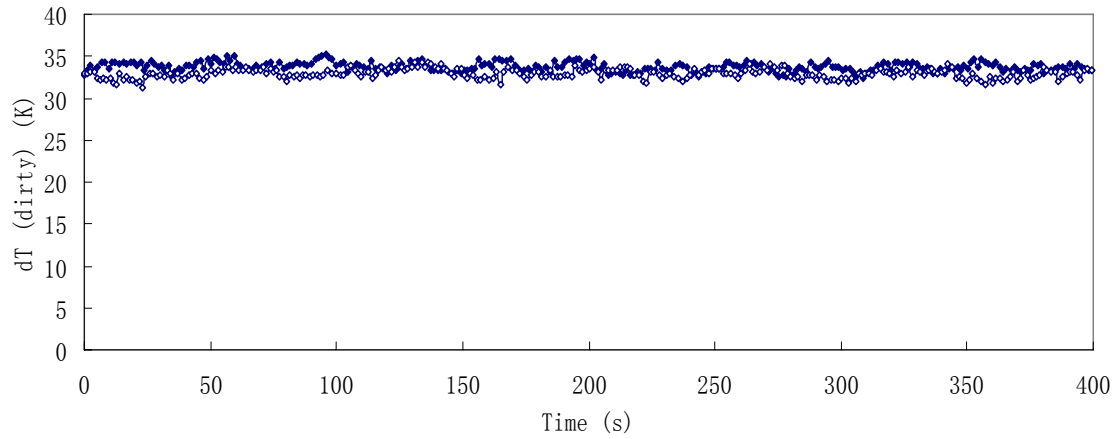


Figure 5-12: “Dirty” sensor temperature difference (T2-c-1700), $\blacklozenge \dot{m}=2\text{g/s}$, $\square \dot{m}=7.9\text{g/s}$

In these two cases, the “dirty” sensor temperature differences were relatively stable with an average of 33.8K for the 2 g/s case and 32.9 K for the 7.9 g/s case. Some fluctuations can be seen from the data collected. Figure 5-13 are the temperature data recorded at the center (T_c) and the periphery (T_p) of the bottom surface of the sensing disc when the air flow rate was 2 g/s and 7.9 g/s.

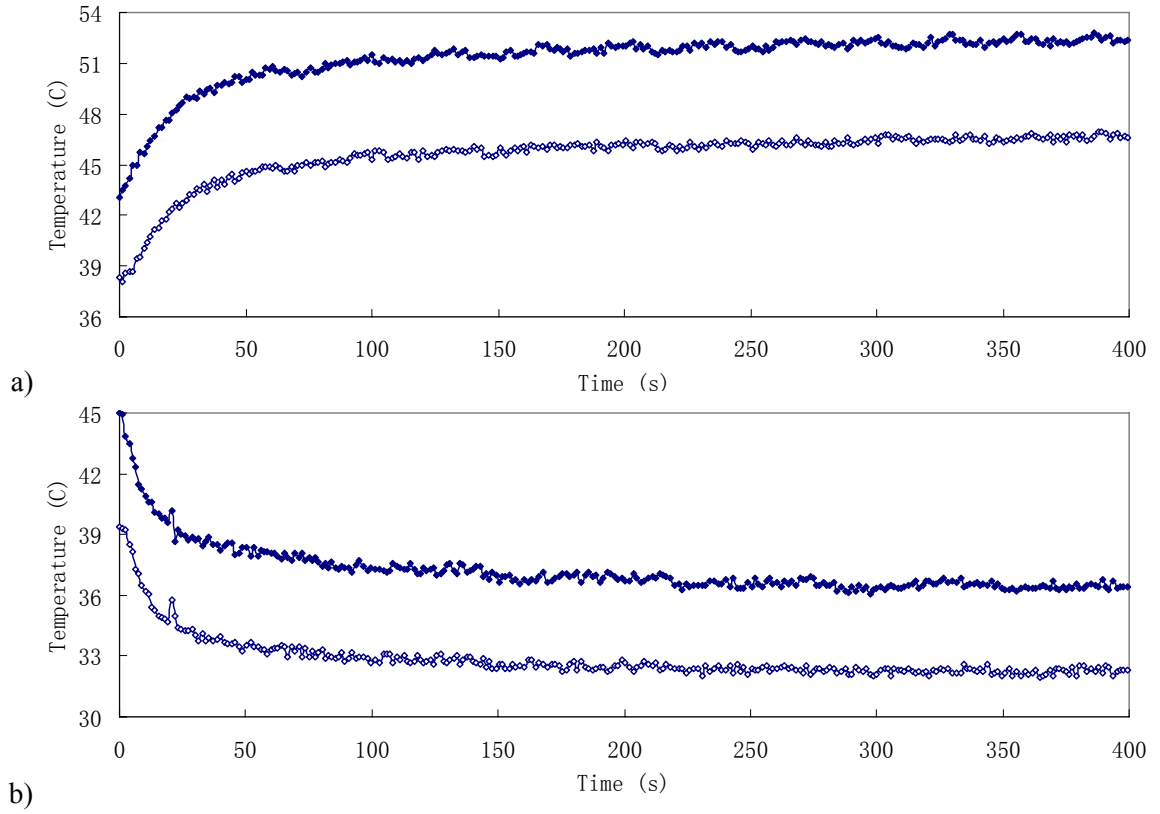


Figure 5-13: Center and periphery temperatures (T2-c-1700), $\blacksquare T_c$, $\diamond T_p$, a) $\dot{m}=2\text{ g/s}$, b) $\dot{m}=7.9\text{ g/s}$

As shown in these two figures, the temperature changes are relatively significant at the beginning of the tests. This is because the on-hold air flow rate, which is the set air flow rate between tests, was maintained at 4 g/s. Therefore, all tests started with a sudden change in air flow rate as shown earlier, which broke the thermal balance at the sensing element and the sensor temperatures began to deviate from their initial values that represented the energy state of the sensing element under the on-hold flow rate. In the two cases, the temperatures increased or decreased exponentially during the first 200 seconds of the test and then appeared to stabilize afterwards. The resulting RTDs under these two air flow rates are shown in Figure 5-14. The average RTD value for the 2 g/s case was 5.76K and 4.2K for the 7.9 g/s case.

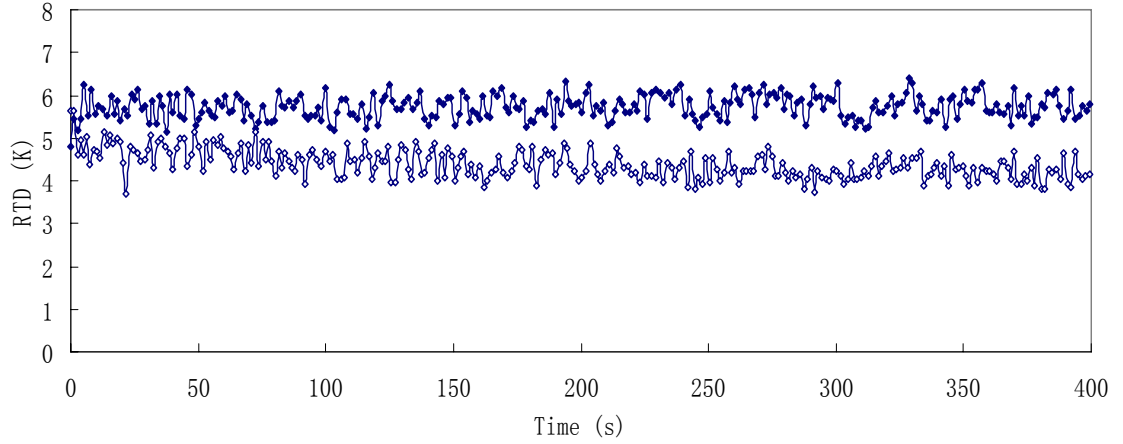


Figure 5-14: RTD (T2-c-1700), $\blacklozenge \dot{m}=2\text{g/s}$, $\blacksquare \dot{m}=7.9\text{g/s}$

Although T_c and T_p exhibit exponential changes during first half of the tests, the RTD values are relatively stable. The initial values of the two cases are almost the same, but the gap widens when the air flow rate is changed. Throughout the process, fluctuations are noticeable which are directly resulted from the fluctuations of T_c and T_p . The temperature fluctuation was likely caused by the automatic air flow rate adjustment and the error in the data acquisition. The magnitude of the fluctuations in the RTD values is as high as 1K for both cases. To find out the sensitivities of the RTD method under these two configurations, the results from T1, T2 and T3 were combined and are plotted in Figure 5-15. Linear approximation is applied to each case and the slope of which is regarded as an approximation of the sensitivity.

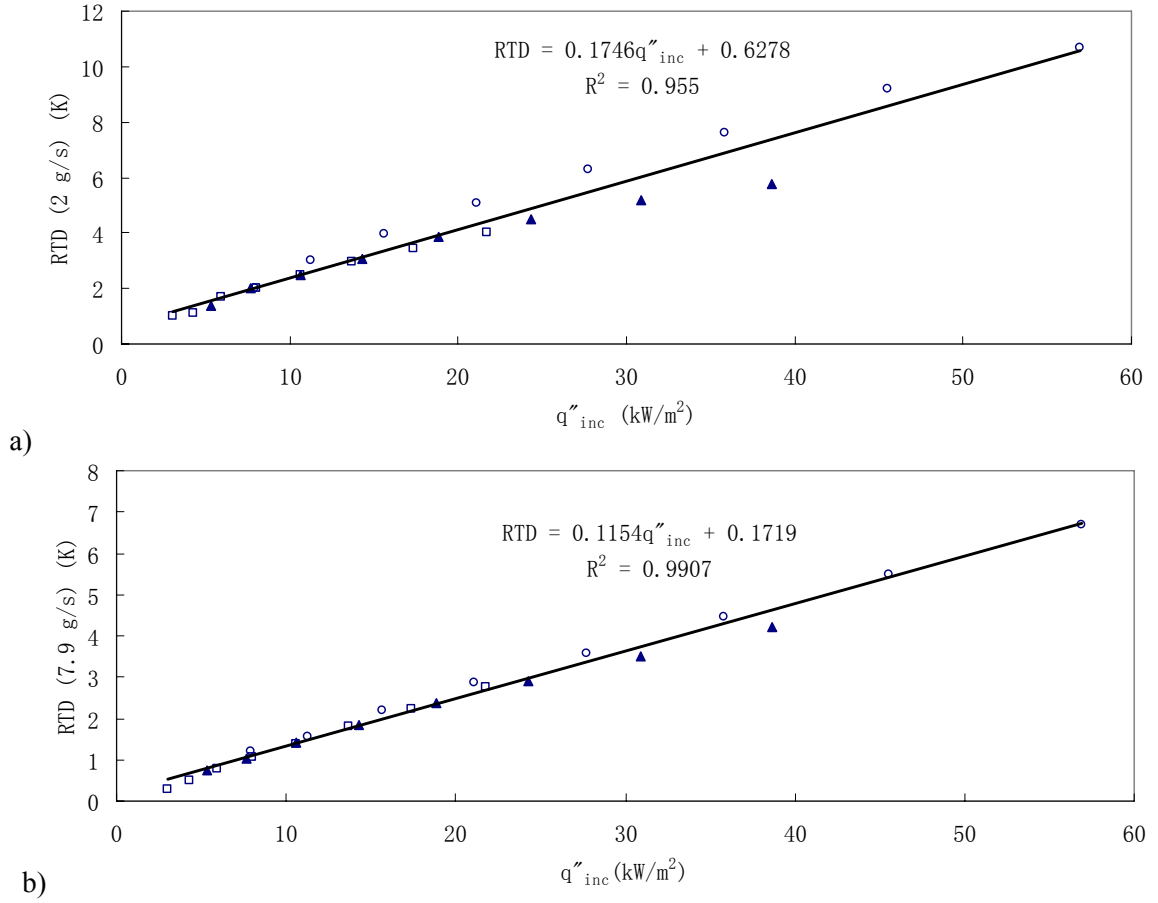


Figure 5-15: Sensitivity for the RTD method, \square T1-c, \blacktriangle T2-c, \circ T3-c, a) $\dot{m}=2\text{g/s}$, b) $\dot{m}=7.9\text{ g/s}$

According to the linear equations shown above, when the air flow rate is 2 g/s, the relationship between the incident radiation heat flux and the RTD can be expressed as:

$$q''_{inc} = 5.73RTD - 3.6 \quad 5-4$$

$$X_{RTD} = 0.1746 \frac{1}{X_{RTD}} = 5.73$$

When the air flow rate is 7.9 g/s, the equation becomes:

$$q''_{inc} = 8.67RTD - 1.49 \quad 5-5$$

$$X_{RTD} = 0.1154 \frac{1}{X_{RTD}} = 8.67$$

Constant Air Flow Rate (0.5mm channel)

As mentioned previously, the air flow rate was decreased accordingly for the sensor with 0.5 mm channel. However, the on-hold air flow rate was maintained at 4 g/s. Figure 5-16 shows the air flow rate signals recorded when the flow rate was set at 0.95 g/s and 2 g/s respectively.

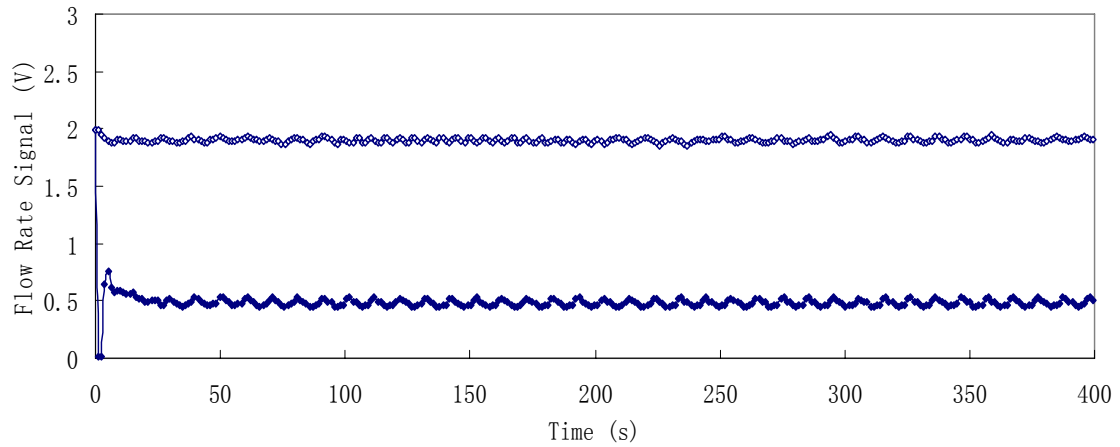


Figure 5-16: Air flow rate signals (T4-c-1700), $\blacklozenge \dot{m}=0.95\text{g/s}$, $\square \dot{m}=3.8\text{g/s}$

Similar jump in air flow rate shown in Figure 5-11 can be seen in Figure 5-16 when the flow rate was change from 4 g/s to 0.95 g/s. The transition is much smoother for the 3.8 g/s case since the difference between the two flow rates is small. Again, small fluctuations in air flow rate can be observed throughout the process. Figure 5-17 shows the "dirty" sensor temperature differences during the tests.

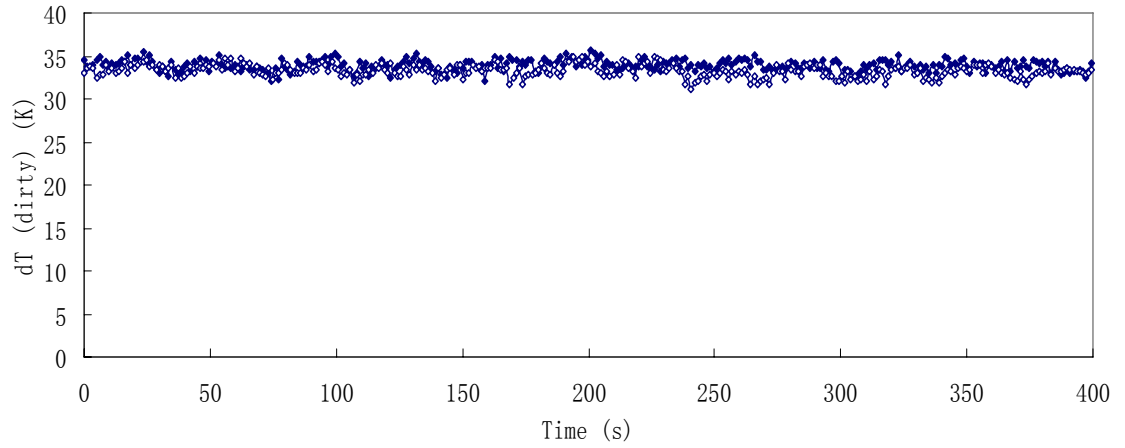


Figure 5-17: “Dirty” sensor temperature difference (T4-c-1700), \blacklozenge $\dot{m}=0.95\text{g/s}$, \blacksquare $\dot{m}=3.8\text{g/s}$

In these two cases, the average “dirty” sensor temperature differences were 33.9K for 0.95 g/s case and 33.3 K for 3.8 g/s case. The fluctuations appeared in “dirty” sensor temperature difference plots resemble the ones from T2, and the average values from these two tests are also very close to the ones shown earlier, which indicates that impact of the air flow on the radiation source was effectively prevented if not completely eliminated. Figure 5-18 shows the results of T_c and T_p when the air flow rate was 0.95 g/s and 3.8 g/s.

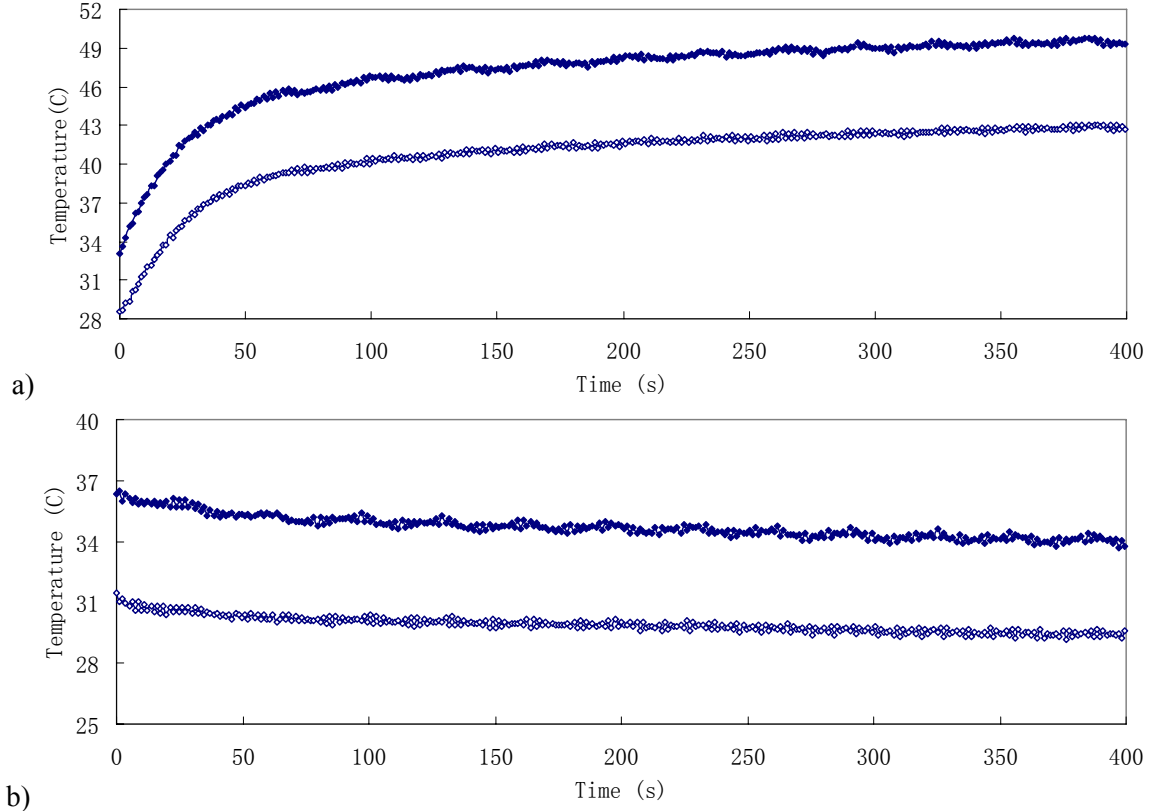


Figure 5-18: Center and periphery temperatures (T4-c-1700), $\blacksquare T_c$, $\diamond T_p$, a) $\dot{m}=0.95\text{g/s}$,
b) $\dot{m}=3.8\text{ g/s}$

As expected, T_c and T_p increased exponentially at the beginning of the test. However, they didn't seem to reach the steady state temperature until the last 50 seconds of the test. The situation is the similar for the 3.8 g/s case in which the temperature changes are much less as the difference between the set flow rate and on-hold flow rate is small. The resulting RTD values under these two air flow rates are shown in Figure 5-19. The average value for 0.95 g/s case was 6.63K and 4.66 K for 3.8 g/s case. Again, the RTD plots are relatively stable although a relatively steep increase can be seen for the first 20 seconds of the 0.95 g/s case as a result of the large flow rate change. Fluctuations with similar magnitude can also be found in these two cases. The results of the RTDs from T4 and T5 are combined and plotted in Figure 5-20.

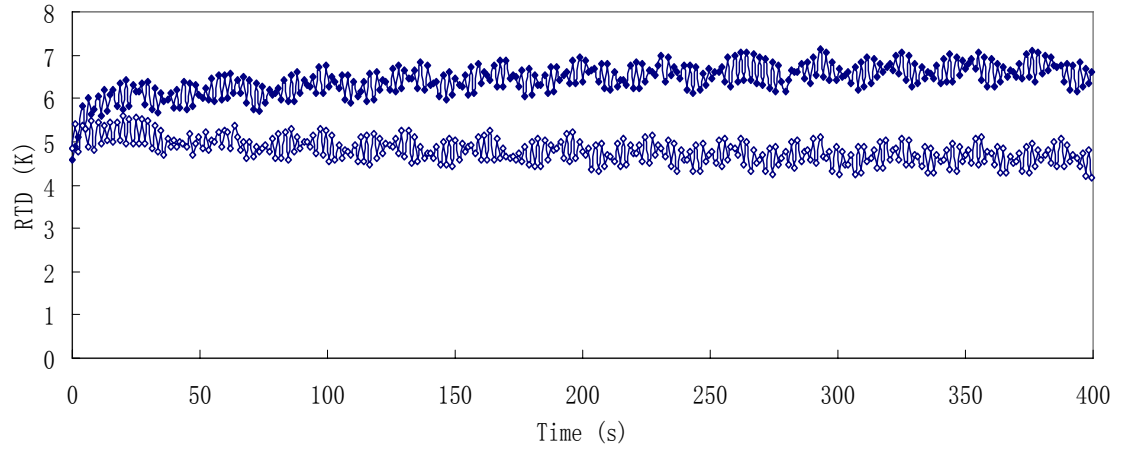
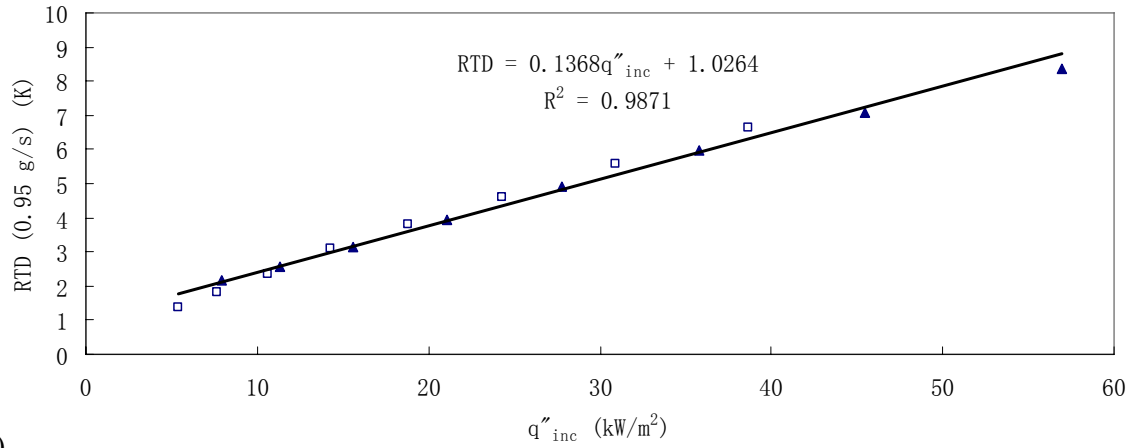
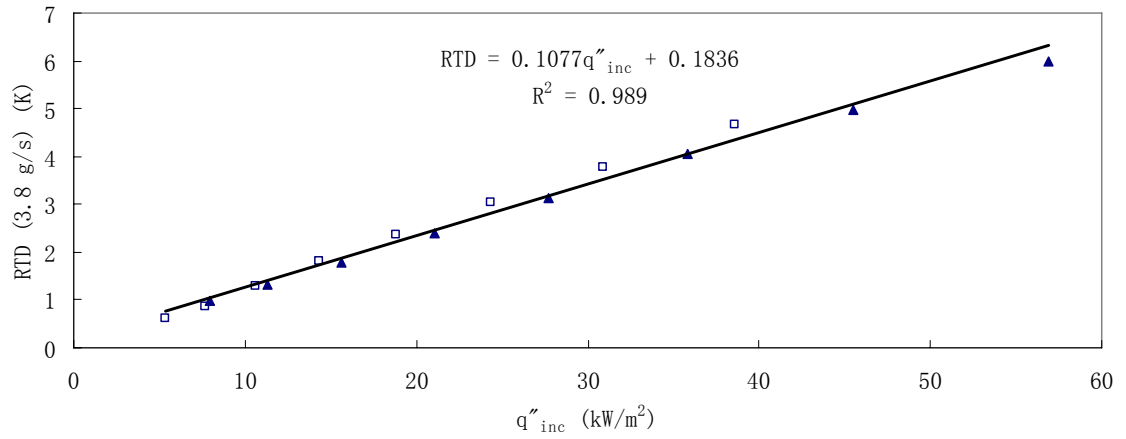


Figure 5-19: RTD (T4-c-1700), $\blacklozenge \dot{m}=0.95\text{g/s}$, $\square \dot{m}=3.8\text{g/s}$



a)



b)

Figure 5-20: Sensitivity for the RTD method, \square T4-c, \blacktriangle T5-c, a) $\dot{m}=0.95\text{g/s}$, b) $\dot{m}=3.8\text{g/s}$

Again, linear approximation is applied to estimate the sensitivities under these two configurations. According to the linear approximations, when the air flow rate is 0.95 g/s, the relationship between the incident radiation heat flux and the RTD can be expressed as:

$$q''_{inc} = 7.31RTD - 7.5 \quad 5-6$$

$$X_{RTD} = 0.1368, \frac{1}{X_{RTD}} = 7.31$$

When the air flow rate is 3.8 g/s, the conversion equation becomes:

$$q''_{inc} = 9.29RTD - 1.7 \quad 5-7$$

$$X_{RTD} = 0.1077, \frac{1}{X_{RTD}} = 9.29$$

Among these four configurations, the sensor sensitivity is highest when the air flow rate is 2 g/s (1mm channel), and the sensitivity is lowest when the air flow rate is 3.8 g/s (0.5mm channel). For sensor with the same channel size, the sensitivity of the RTD method decreases with increasing air flow rate. The trend agrees with the numerical results shown in Chapter 4 but contradicts the results in the original study. One possible reason is that in the original sensor design, the air was supplied through two tubes wrapped around the water tube of the boiler; while in the present design, the sensor tip was attached to a straight air supply tube. This change in air inlet condition might have led to difference in the flow pattern of the annular jet, and in turn, the response of convection heat transfer configuration to the change in air flow rate. However, this premise was left to be proved in future studies as it was considered beyond the scope of this project.

Oscillating Air Flow Rate (1mm channel)

As mentioned in previous chapters, over the course study, the air flow oscillation pattern was changed from square wave form to sinusoidal wave form because the later one generated more accurate flow oscillations (no sudden jumps for the controller) and consequently smoother

temperature oscillation curves. All the later tests were conducted using the sinusoidal wave form. According to the analysis in Chapter 3, and the numerical results shown in Chapter 4, the disc temperature should oscillate between the upper and lower steady state temperatures which are essentially the sensor temperatures under maximum and minimum air flow rates. Also, the amplitude of the temperature oscillation should increase with the period of the air flow oscillation. To prove this experimentally and also to determine the oscillation period to be used in later experiments, air flow oscillations with different periods were applied to find out the response of the actual sensor to the flow oscillation period change. The tests were conducted using the sensor with 1mm channel and the maximum and minimum constant air flow rate were 7.9 g/s and 2 g/s. The three oscillation periods tested were: 40s, 80s and 200s. The resulting T_c oscillation and its upper and lower steady state temperatures are shown in Figure 5-21.

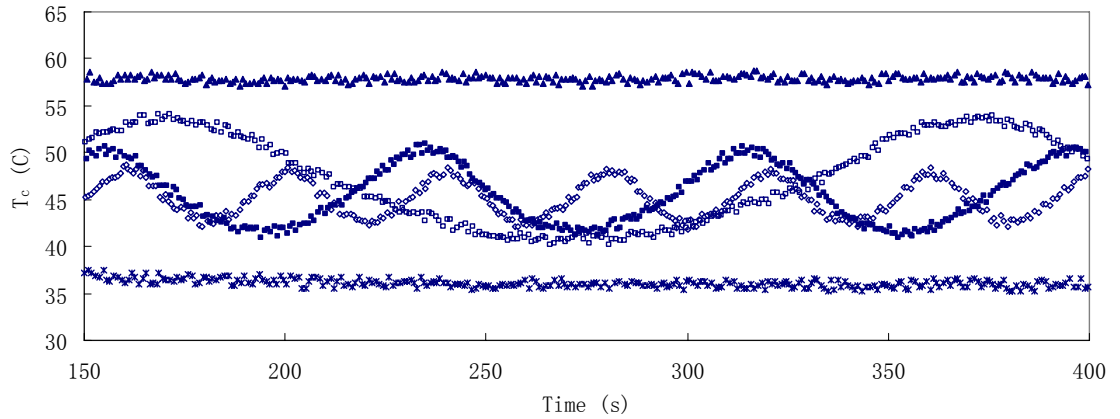


Figure 5-21: Effect of flow oscillation period on T_c oscillation, \diamond P=40s, \blacksquare P=80s, \square P=200s, \blacktriangle T_c at $\dot{m}=2$ g/s, $*$ T_c at $\dot{m}=7.9$ g/s

When the period was increased from 40 seconds to 80 seconds, the A_c was increased by 58%. The amplitude at 200-second oscillation period is double that of 40-second period. The response of A_c can be roughly related to the upper and lower steady state temperatures, T_1 , T_2 using Equation 5-8

$$A_c \approx (T_1 - T_2)(1 - \exp^{-0.06P}) \quad 5-8$$

where P is the period of the oscillation. Although higher sensitivity can be achieved by increasing the air flow oscillation period, longer oscillation period also means fewer temperature amplitude

readings per unit of time and slower tracking of external heat flux variations. As a compromise, the oscillation period was set at 80 seconds for all the later tests. Figure 5-22 is the recorded signal for the oscillating air flow rate with 1mm channel.

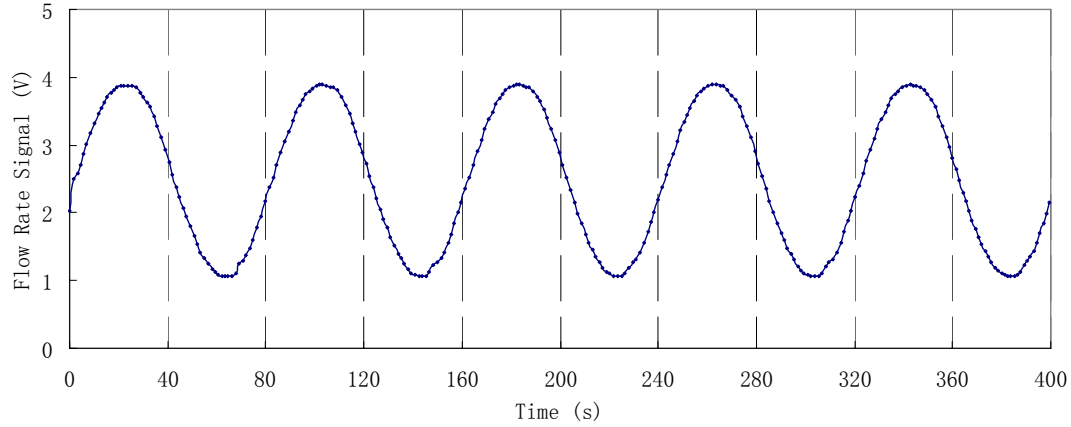


Figure 5-22: Air flow rate signal (T2-s-1700)

In this case, the starting air flow rate is 5 g/s, thus the difference between the on-hold air flow rate (still 4 g/s) and the starting air flow rate is relatively small. As a result, no significant jump of air flow rate was observed. As shown in the plot, the air flow rate follows closely to the set sinusoidal function through out the process. Interestingly, unlike the signals of constant flow cases, no noticeable flow rate fluctuation is shown in the oscillating flow cases. Figure 5-23 shows the "dirty" sensor temperature difference during this test. In this case, the average "dirty" sensor temperature difference is 31.6K. The result of T_c oscillation is shown in Figure 5-24.

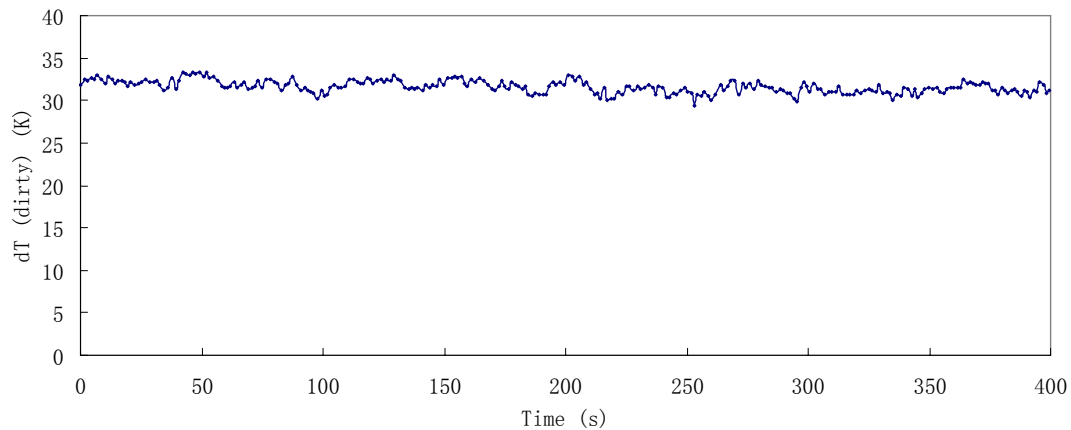


Figure 5-23: "Dirty" sensor temperature difference (T2-s-1700)

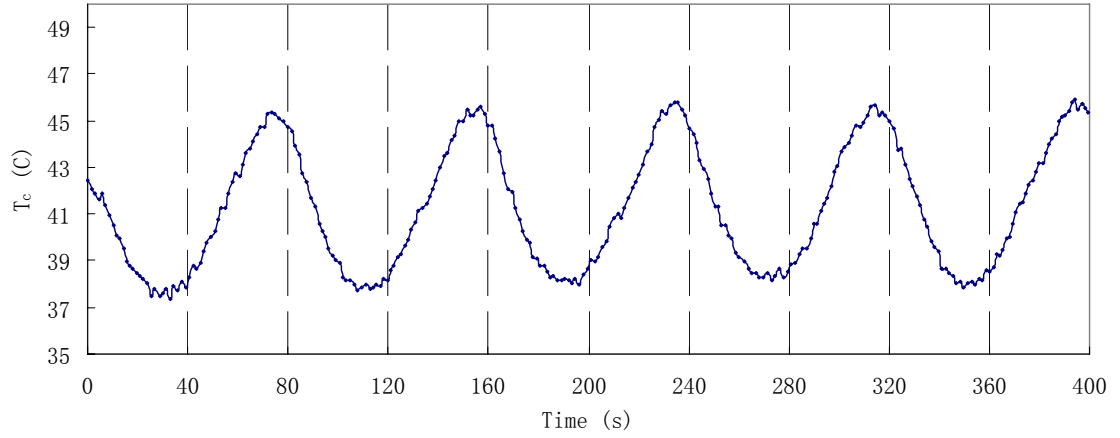


Figure 5-24: T_c oscillation (T2-s-1700)

The shape of the T_c oscillation resembles the numerical results shown in the previous chapter. For the oscillation method, in terms of the shape of the temperature curve, the numerical results agree quite well with the experimental ones. The results of the T_c oscillation amplitude from T1, T2 and T3 are combined and plotted in Figure 5-25. Linear approximation is applied to estimate the sensitivities of the oscillation in this case.

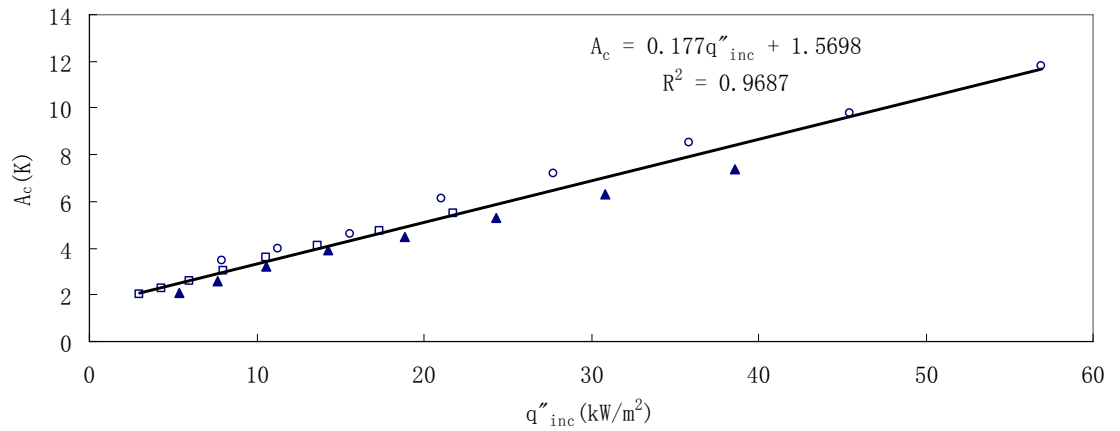


Figure 5-25: Sensitivity for the oscillation method, \square T1-s, \blacktriangle T2-s, \circ T3-s

According to the results shown above, for sensor with 1mm channel, the heat flux can be expressed in terms of the A_c as:

$$q''_{inc} = 5.65A_c - 8.87$$

5-9

$$X_{A_c} = 0.177, \frac{1}{X_{A_c}} = 5.65$$

Oscillating Air Flow Rate (0.5mm channel)

For the 0.5mm channel, the maximum and minimum air flow rates were changed to 3.8 g/s and 0.95 g/s. Figure 5-26 is the air flow rate signal recorded.

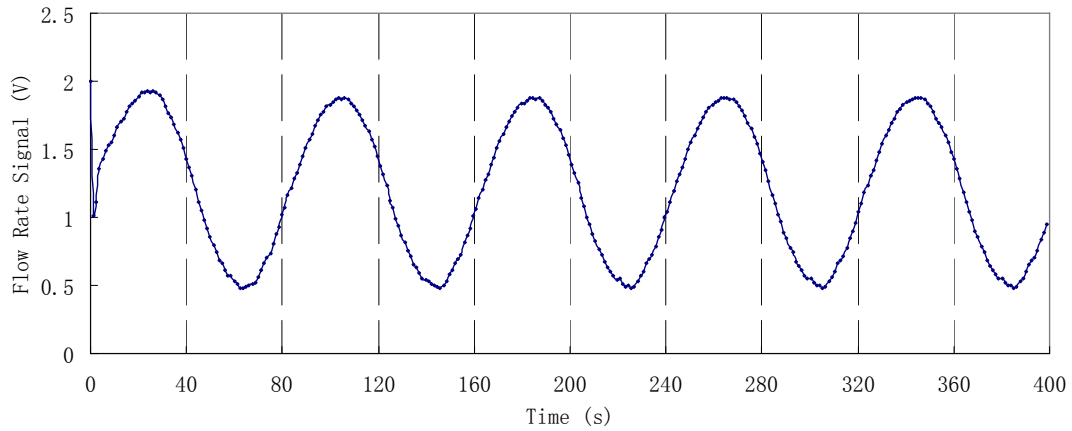


Figure 5-26: Air flow rate signal (T4-s-1700)

The starting air flow rate in this case is 2.5 g/s while the on-hold air flow rate is still 4 g/s. A more obvious drop in air flow rate can be seen at the beginning of the plot, but the rest of the flow rate signal follow closely to the set sinusoidal function. Figure 5-27 shows the "dirty" sensor temperature differences during this test. In this case, the average "dirty" sensor temperature difference was 33.38K. The result of T_c oscillation in case is shown in Figure 5-28.

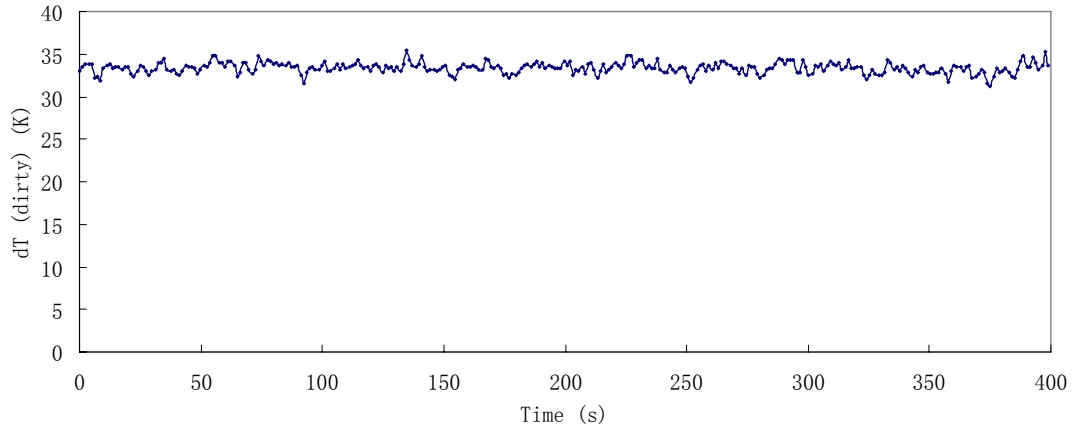


Figure 5-27: “Dirty” sensor temperature difference (T4-s-1700)

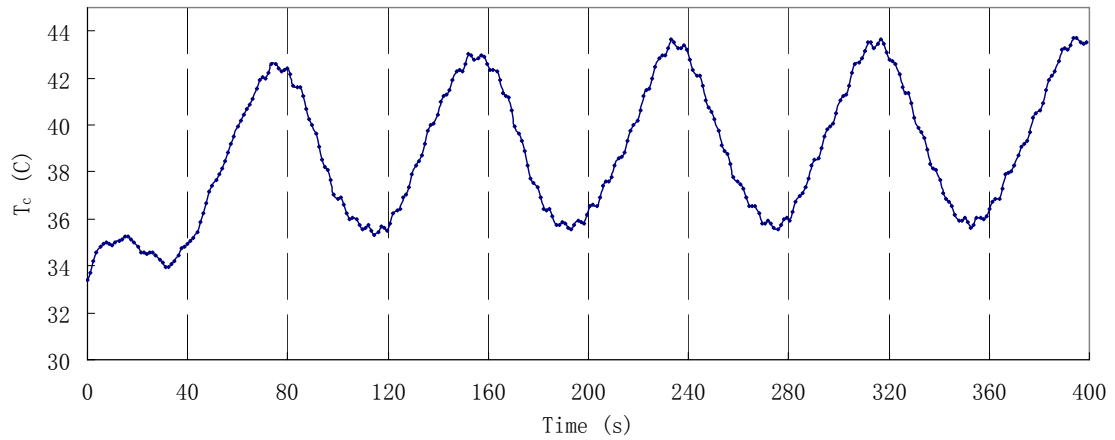


Figure 5-28: T_c oscillation (T4-s-1700)

Unlike the result shown in Figure 5-24, T_c experienced a transition period at the first 20 seconds of the test and then started to oscillate steadily. The transition is caused by the sudden air flow rate drop as shown in Figure 5-26, which led to sudden increase in net heat flux into the sensing element at the beginning of the test and thus distorts the temperature oscillation curve. Similar transition period has been shown in the numerical results where the sensing element also experienced a sudden heat flux increase at the beginning. The results of the T_c oscillation amplitude from T4 and T5 are combined and plotted in Figure 5-29. Linear approximation is again applied to exam the sensitivity.

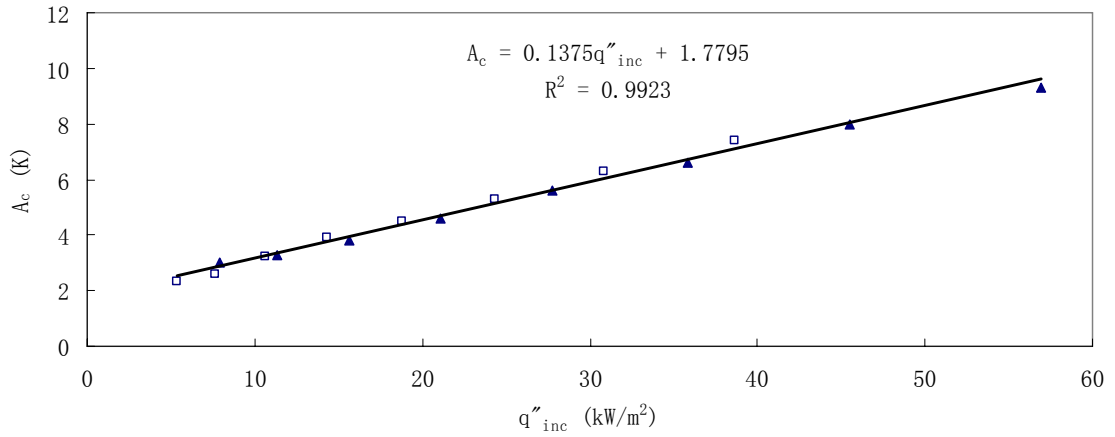


Figure 5-29: Sensitivity for the oscillation method, \square T4-s, \blacktriangle T5-s

According to the results shown above, for sensor with 0.5 mm channel, the heat flux can be expressed in terms of the A_c as:

$$q''_{inc} = 7.27A_c - 12.94 \quad 5-10$$

$$X_{A_c} = 0.1375, \quad \frac{1}{X_{A_c}} = 7.27$$

Based on the experimental results, although the ratio between the maximum and minimum air flow rate was 4 in both cases, the sensitivity with the 1mm channel is about 29% higher than that of the 0.5 mm channel, which contradicts the numerical results where the sensitivity of the oscillation method appears to be 5% higher with the 0.5mm channel. On the other hand, the numerical results also show that the sensitivities of the oscillation method under the tested flow configurations are higher than those of the RTD method. Compared with the results of the sensor with 1mm channel shown in Figure 5-25, the results of the sensor with 0.5mm channel showed better linear correlation (less data scatter).

“Dirty” Heat Flux Sensor

The average “dirty” sensor temperature differences calculated based on the data from T2 and T4 are plotted against the estimated incident radiation heat fluxes as shown in Figure 5-30. The relationship between the incident radiation heat flux and the “dirty” sensor temperature difference is also approximated by a linear equation.

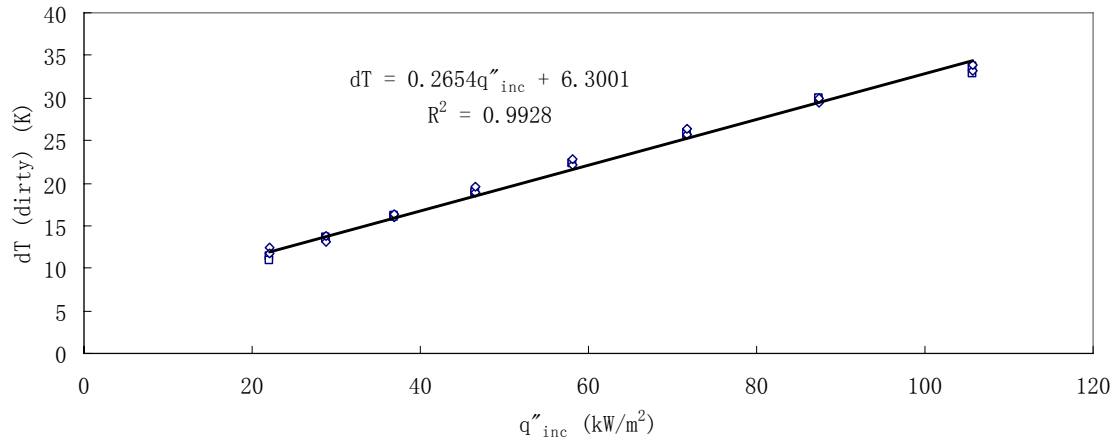


Figure 5-30: Sensitivity for “dirty” heat flux sensor, \diamond T2-c, \square T4-c

According to the linear approximation, the incident radiation heat flux is related to the “dirty” sensor temperature difference as:

$$q''_{inc} = 3.77dT_{Dir} - 23.74 \quad 5-11$$

$$X_{Dir} = 0.2654, \quad \frac{1}{X_{Dir}} = 3.77$$

In practice, the “dirty” heat flux sensor should be calibrated against the absorbed radiation heat flux since it is designed to measure the heat flux received when covered with fuel ash. Theoretically this step can be simply achieved by adding the surface absorptivity into the equation above. However, the actual surface radiation absorptivity of the sensor was uncertain at the moment. Moreover, dramatic surface characteristic change was observed which likely had led to the change in surface absorptivity. More on this will be discussed in Chapter 6.

5.3.2 Unsteady Radiation Heat Flux

According to the results shown in [15], the RTD method has the advantage under unsteady heat fluxes due to the nature of spatial temperature difference based RTD method. Therefore, only the oscillation method was tested under unsteady heat fluxes to study how the temperature behaves and how effective the data processing procedures are when dealing with unsteady heat fluxes. However, with the setup employed in this experiment, it was very difficult to create a step change heat flux. Therefore, the sensors were tested under relatively gradual heat flux changes created in the initial heating and final cooling period. The results shown below are all obtained from T4-s-heating. Figure 5-31 is the recorded “dirty” sensor temperature difference during the heating process, which is used as an approximate indication of the incident radiation heat flux from the heat source.

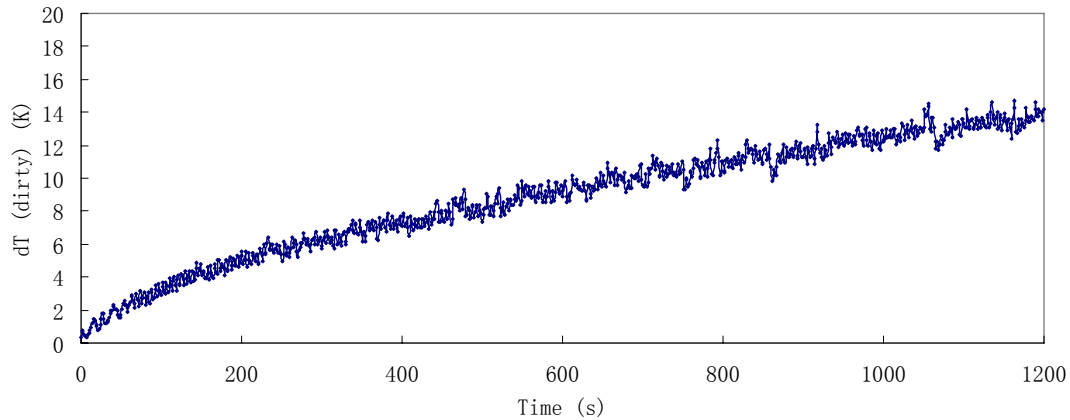


Figure 5-31: “Dirty” sensor temperature difference (T4-s-heating)

As shown in the plot above, the heat flux increasing is gradual and nearly linear from about 300 second to the end of the process. Figure 5-32 is the T_c oscillation recorded during the process.

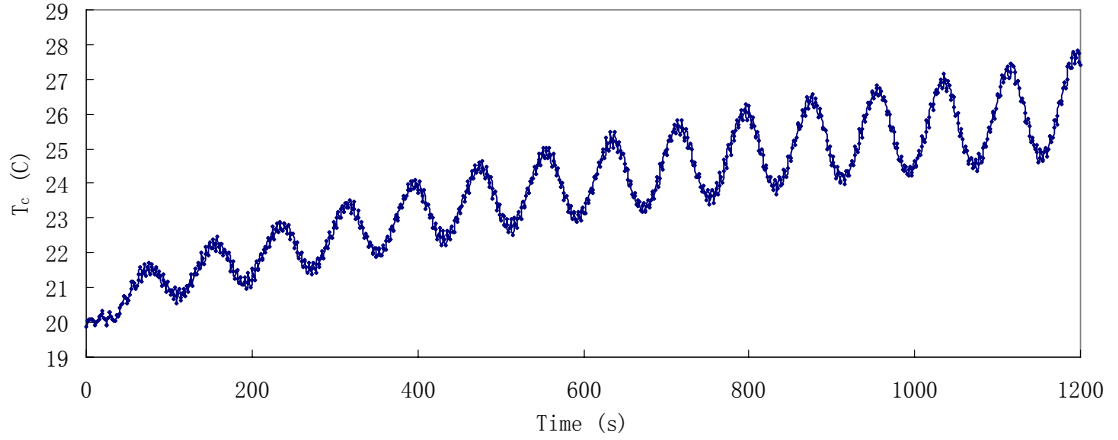


Figure 5-32: T_c oscillation (T4-s-heating)

It can be seen that the overall value of T_c increases steadily, with a shape similar to that of the “dirty” sensor temperature difference, while accompanied by a sinusoidal oscillation with increasing amplitude. This indicates that the T_{dc} and T_{ac} components of T_c are responding to the heat flux change simultaneously. Figure 5-33 is the recorded “dirty” sensor temperature difference during the cooling process. In this case, the furnace was maintained at 1700F for the first 300 seconds and then turned off.

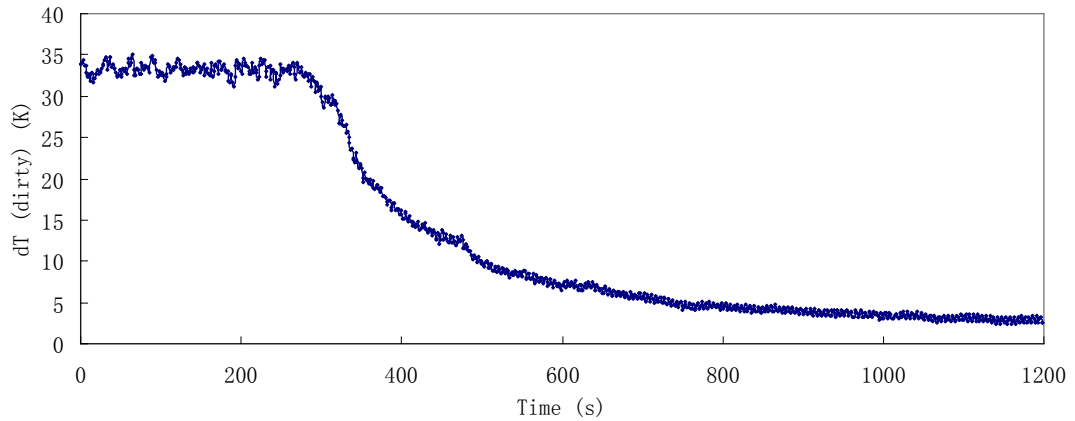


Figure 5-33: “Dirty” sensor temperature difference (T4-s-cooling)

As shown in this plot, the “dirty” sensor temperature different is stable at approximately 33K for the first 300 seconds and then starts to drop exponentially until the end of the test. The resulting T_c oscillation is shown in Figure 5-34.

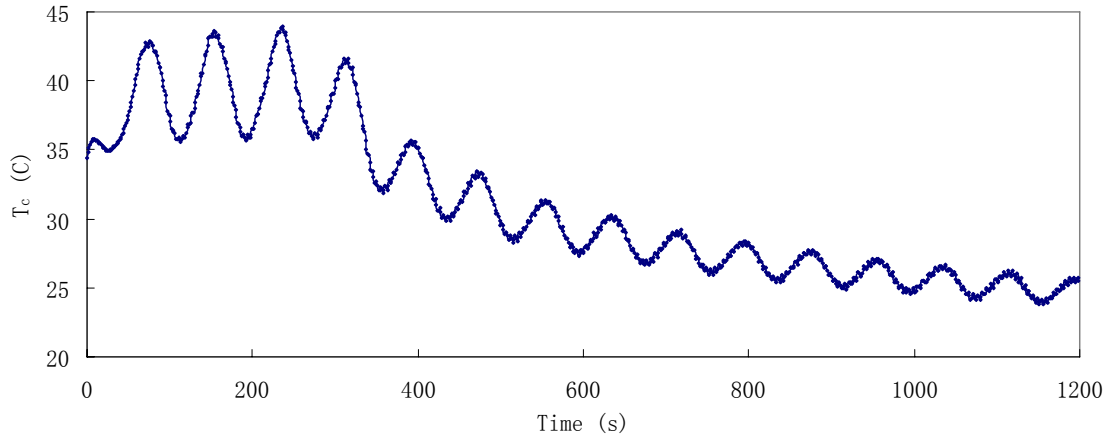


Figure 5-34: T_c oscillation (T4-s-cooling)

For the first 300 seconds, the T_c oscillation is almost the same as the one shown in Figure 5-28. Once the furnace is turned off the overall value of T_c starts to decrease and is accompanied by a noticeable sudden decrease in oscillation amplitude. Which again indicates the simultaneous responses of the T_{dc} and T_{ac} components to the heat flux change.

5.4 Data Processing Procedure Assessment

As mentioned in Chapter 3, over the course of study, three data processing procedures were created, which are essential for on-line heat flux estimation using the oscillation method. To examine their effectiveness, the three procedures are applied to some of the results show above. To help illustrate the two amplitude extraction procedures, the process described in Equation 3-21 and 3-26 are divided into two steps: first, calculate absolute values of the half period temperature differences or central temperature difference, and then search for local maximums which are supposed to represent the A_c . First, the procedures are applied to the results of steady incident radiation case T4-s-1700. Figure 5-35 and 5-36 show the results of the two steps of the half period temperature difference procedure.

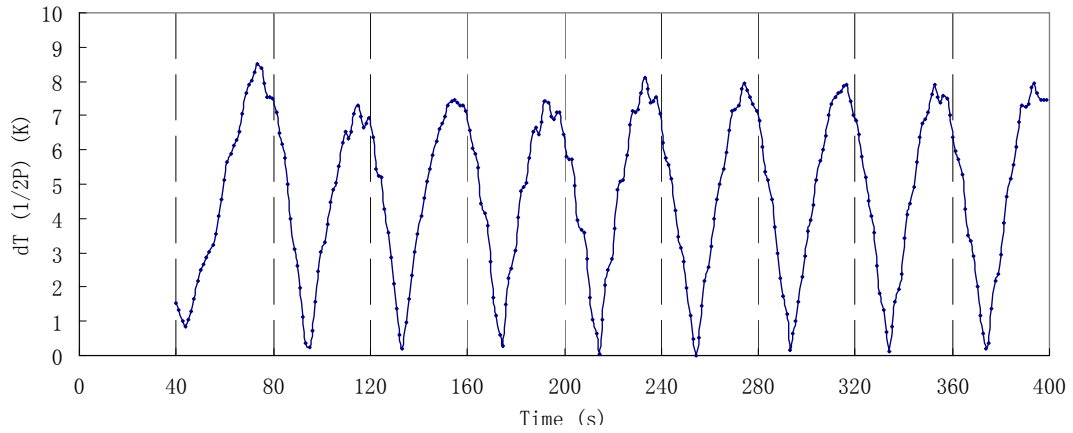


Figure 5-35: Result after first step of the HPTD procedure (T4-s-1700)

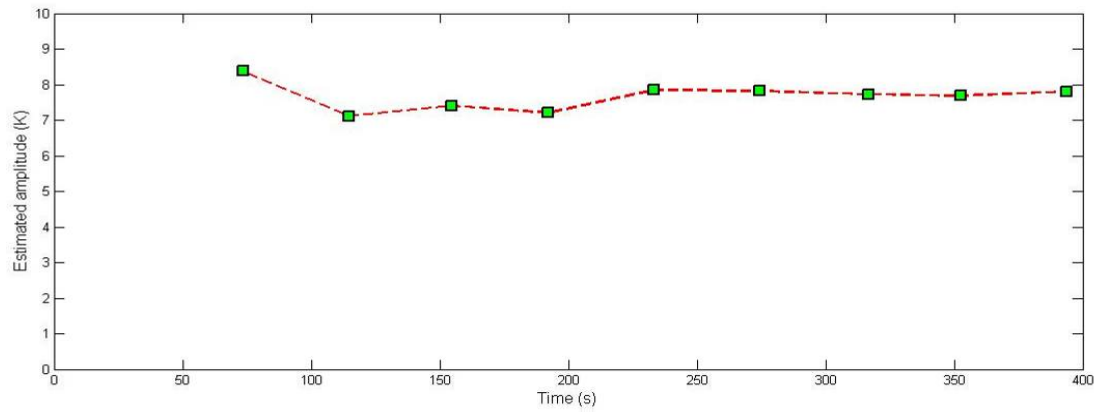


Figure 5-36: Estimated amplitude values, HPTD procedure, (T4-s-1700)

For the half period temperature difference procedure, the first amplitude reading is obtained one period after the data recording is started. As shown in Figure 5-36, the amplitude values are relatively stable, indicating a steady incident radiation heat flux. The same temperature data processed using the one period temperature difference procedure is shown in Figure 5-37.

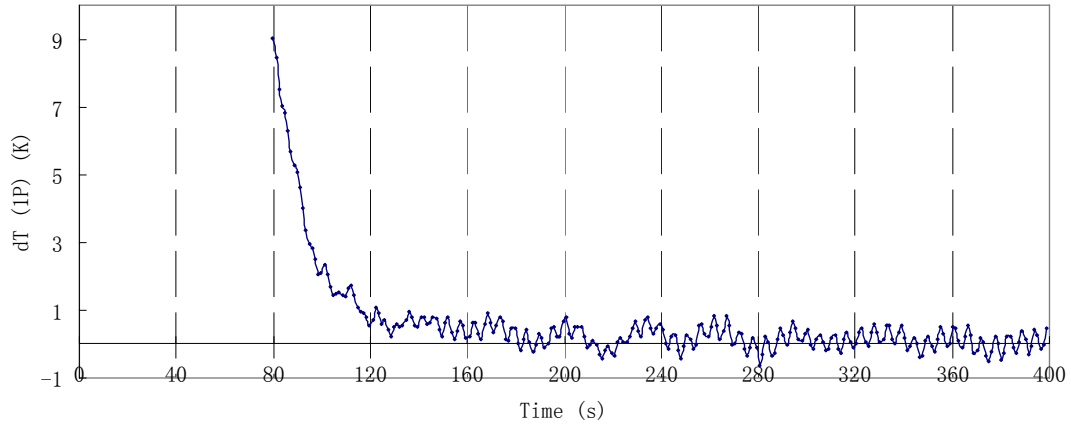


Figure 5-37: Result of the OPTD procedure (T4-s-1700)

The initial spike in the plot indicates the heat flux increase at the beginning of the test as the air flow rate dropped from the on-hold flow rate (4 g/s) to the set flow rate (2 g/s). For the rest of the process, the plot stays close to zero with some fluctuations, which is expected under the stable incident radiation heat flux. The small oscillations are caused mainly by the unstable temperature measurements while the greater fluctuations are likely caused by the procedure itself as will be explained Chapter 6. Figure 5-38 and 5-39 show the results of the two steps of the central temperature difference procedure.

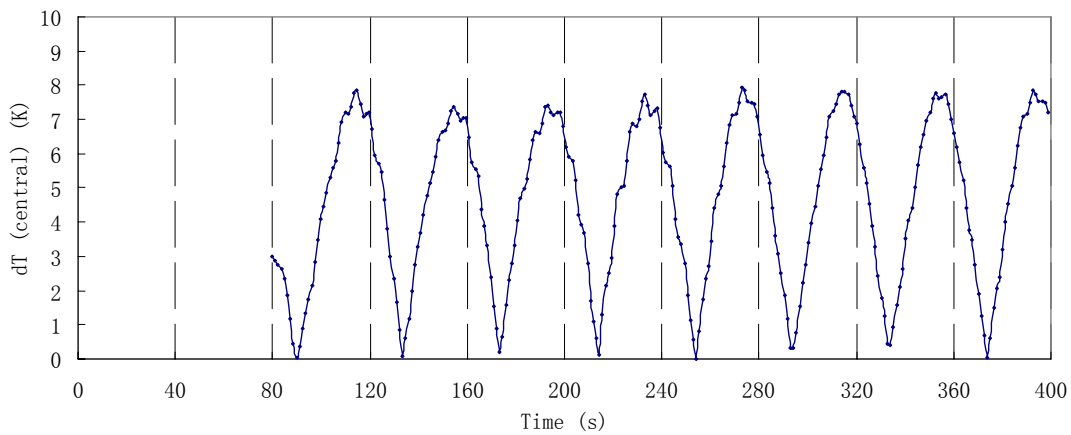


Figure 5-38: Result after first step of the CTD procedure (T4-s-1700)

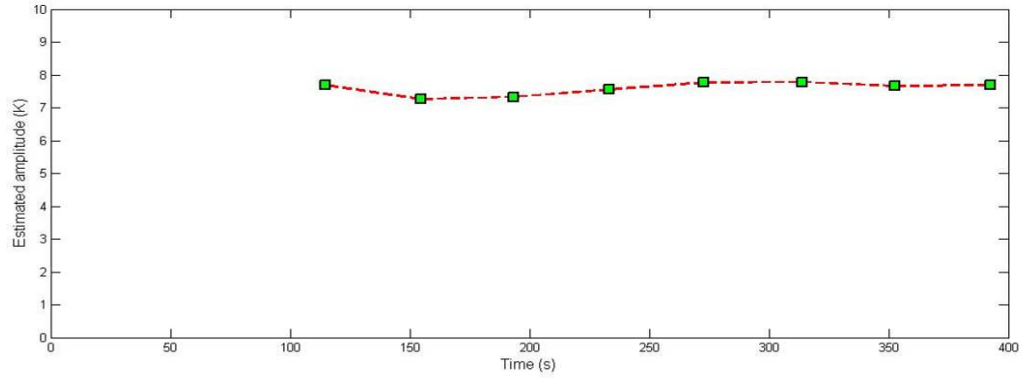


Figure 5-39: Estimated amplitude values, CTD procedure (T4-s-1700)

For central temperature difference procedure, the first reading is obtained one and half period after the data recording is started. When comparing with the results shown in Figure 5-36, the estimated amplitude values are nearly the same but the ones obtained through the central temperature difference procedure are slightly more stable. The three procedures are then applied on the results obtained from the heating process (T4-s-heating). Figure 5-40 and 5-41 show the results of the two steps of the half period temperature difference procedure.

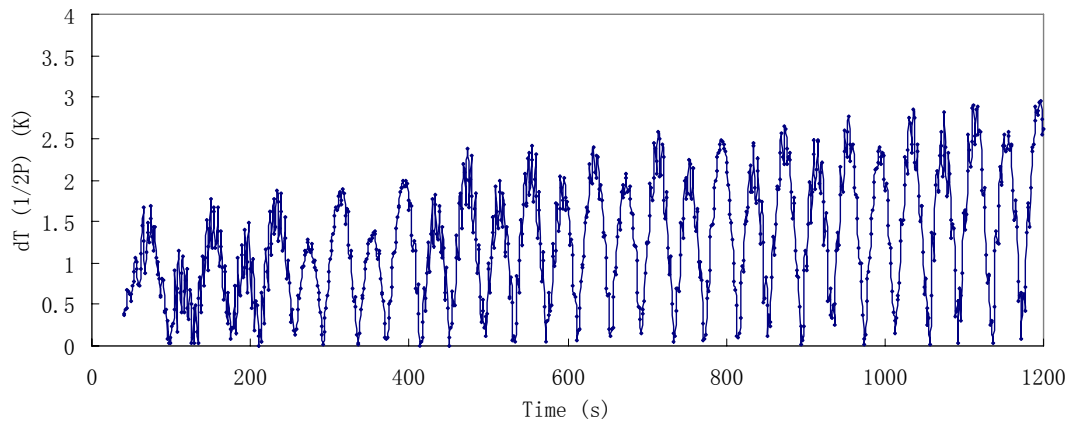


Figure 5-40: Result after first step of the HPTD procedure (T4-s-heating)

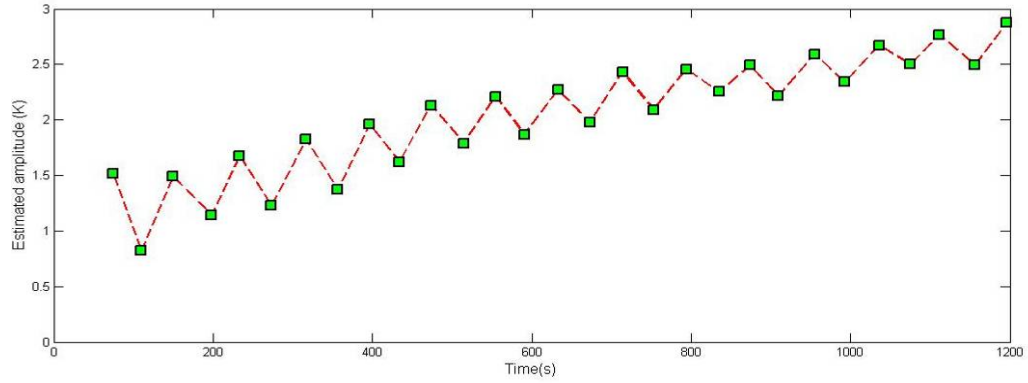


Figure 5-41: Estimated amplitude values, HPTD procedure (T4-s-heating)

As shown above, the problem of the half period temperature difference procedure becomes obvious when dealing with the unsteady heat fluxes. Although it appears that the values of the estimated amplitude increases in the same manner as the incident radiation heat flux indicated by the “dirty” sensor temperature difference shown in Figure 5-31, the estimation result is never stabilized. Therefore, when the half period temperature difference procedure is used, the secondary one period temperature procedure is necessary when dealing with unsteady heat fluxes. Figure 5-42 shows the results of the temperature data after being processed by the one period temperature difference procedure.

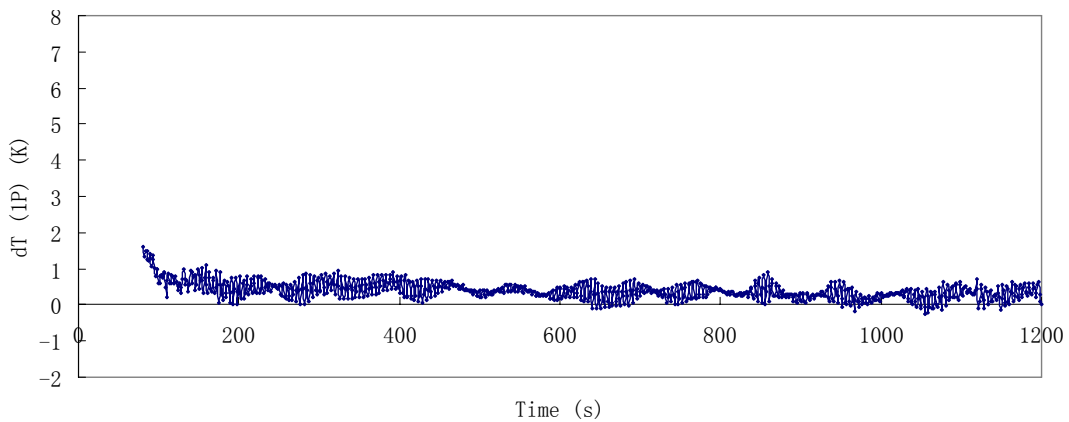


Figure 5-42: Result of OPTD procedure (T4-s-heating)

As shown above, the plot of the one period temperature difference remains relatively stable above 0, indicating a small but steady positive rate of change of the incident radiation heat flux. The

results of the two steps of the central temperature difference procedure are shown in Figure 5-43 and 5-44.

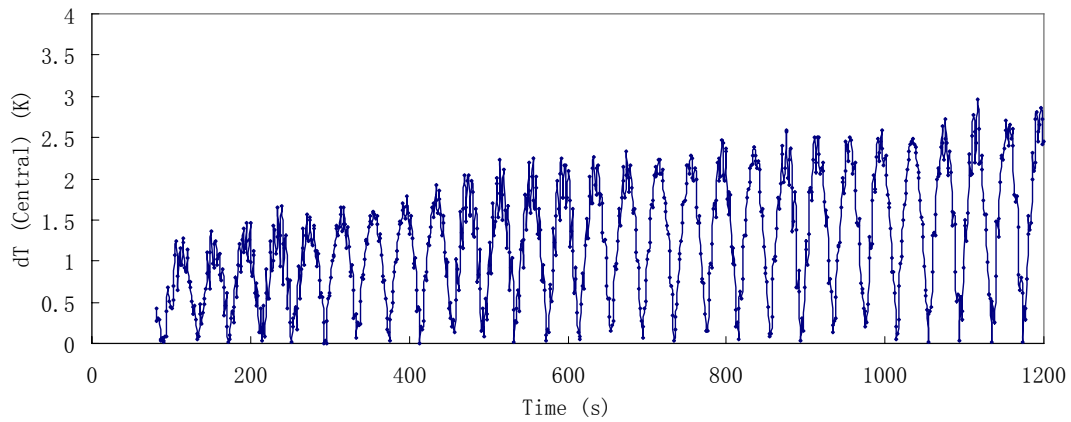


Figure 5-43: Result after first step of the CTD procedure (T4-s-heating)

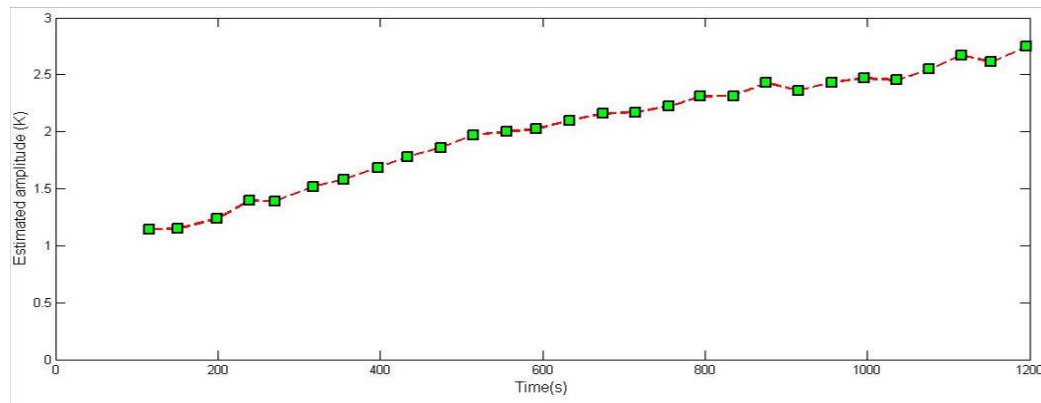


Figure 5-44: Estimated amplitude values, CTD procedure (T4-s-heating)

By comparing the results shown in Figure 5-41 and 5-44, it is obvious that the estimation made by the central temperature difference procedure follows more closely to the incident radiation heat flux change. Although the first reading appears half period later than the half period temperature difference procedure, it effectively eliminates the fluctuation seen in the half period temperature difference results. The three procedures are then applied on the results obtained from the cooling process (T4-s-cooling) to further illustrate these three procedures. Figure 5-45 and 5-46 show the results of the two steps of the half period temperature difference procedure.

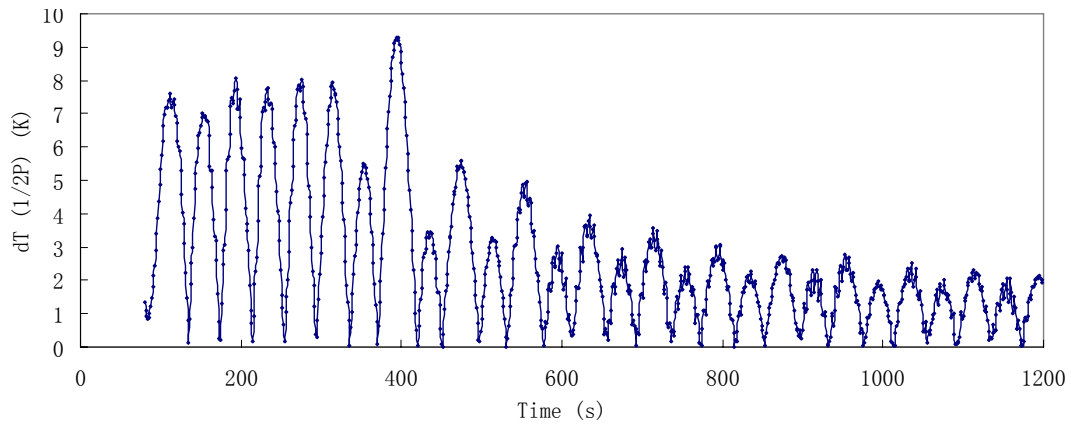


Figure 5-45: Result after first step of the HPTD procedure d (T4-s-cooling)

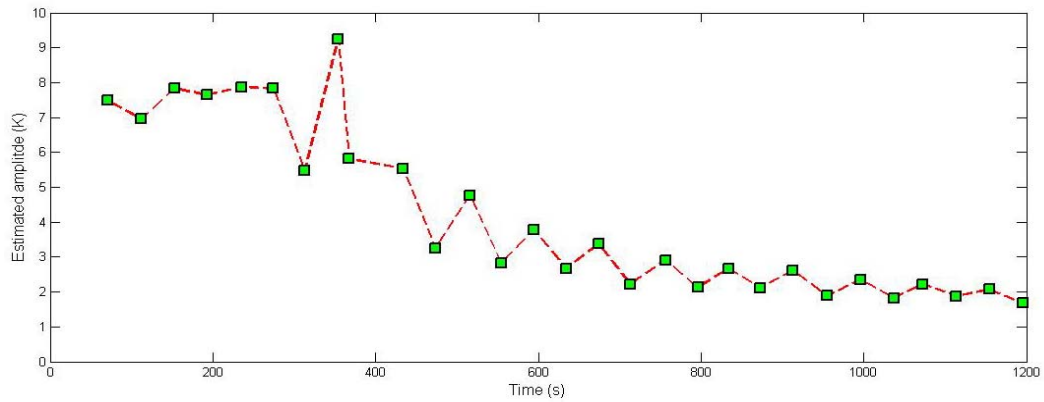


Figure 5-46: Estimated amplitude, HPTD procedure (T4-s-cooling)

Again, the estimation result made by the half period temperature difference procedure becomes unstable when the heat flux is changing. The fluctuation appears to be significant at the onset of the sudden heat flux drop. As the heat flux starts to stabilize near the end of the process, the amplitude of the fluctuation also decreases. Figure 5-47 shows the results of the temperature data after being processed by the one period temperature difference procedure.

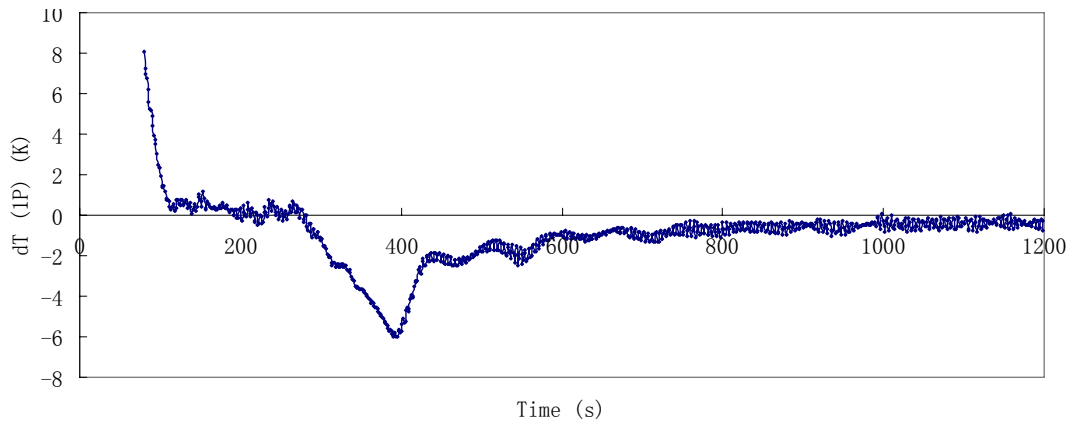


Figure 5-47: Result of OPTD procedure (T4-s-cooling)

Again, the value of the processed temperature correctly reflects the slope of the heat flux change, as the plot remains close to 0 from the 0 to 300 seconds then sharply drops to about -6, and gradually climbs back towards 0. Figure 5-48 and 5-49 show the results of the two steps consist the central temperature difference procedure.

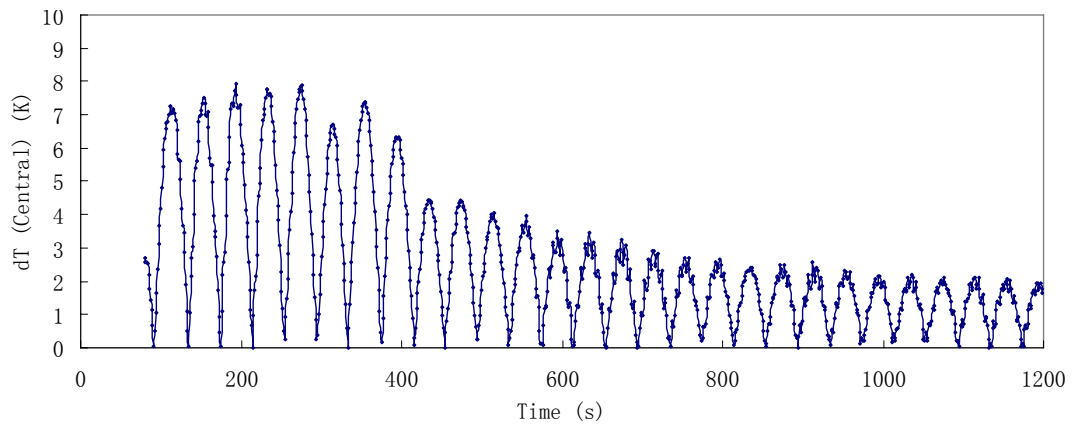


Figure 5-48: Result after first step of the CTD procedure (T4-s-cooling)

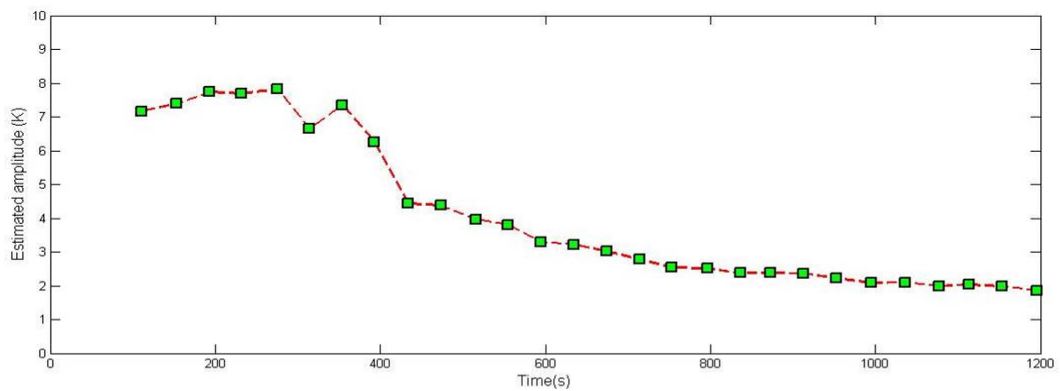


Figure 5-49: Estimated amplitude, CTD procedure (T4-s-cooling)

As shown above, the central temperature difference procedure is more effective when dealing with unsteady heat fluxes. Although slight fluctuation is also observed at the onset of the heat flux drop, its magnitude is much smaller compared with the one shown in Figure 5-46. These results have demonstrated that the central temperature difference procedure can in fact work independently in both steady and unsteady heat flux situations, if piece wise linear approximation is acceptable. On the other hand, it can always be combined with the one period temperature difference procedure to produce continuous heat flux estimations. Although the estimated incident radiation heat fluxes are not shown above, it can be simply obtained by substituting the estimated amplitude values into the linear conversion equations shown earlier. Also, based on the results obtained from the unsteady heat flux cases, the relationship between the one period temperature difference and the incident radiation heat flux can be estimated. It was found that for the sensor with 1mm channel, the incident radiation is related to the one period temperature difference by:

$$q''_{inc} = q''_{initial} + \sum_{i=1}^N 3.6 \frac{dT_{1P}}{P} \quad 5-12$$

For the sensor with 0.5mm channel, the relationship becomes:

$$q''_{inc} = q''_{initial} + \sum_{i=1}^N 4 \frac{dT_{1P}}{P} \quad 5-13$$

In both cases, P represents the oscillation period in second, N represents the total number of temperature data, and $q''_{initial}$ is the starting heat flux level, which in practice is to be estimated by either the half period temperature difference procedure or central temperature difference procedure. This also means that, this secondary method is not supposed to work independently.

Chapter 6 Discussion

6.1 Comparing Experimental and Numerical Results

As shown in the previous two chapters, the relationship between the dependent variables and the incident radiation heat flux estimated based on numerical and experimental results are quite different. Table 6-1 summarizes the parameters of the linear equations obtained from the two groups of results.

Table 6-1: Summary of the parameters in the conversion equations

		Numerical		Experimental	
		1/X	C	1/X	C
RTD method	2 g/s	22.52	-7.02	5.73	-3.6
	7.9 g/s	29.5	-26.27	8.67	-1.49
	0.95 g/s	19.72	-34.12	7.31	-7.5
	3.8 g/s	25.25	-10.13	9.29	-1.7
Oscillation method	2-7.9 g/s	17.39	-60.1	5.65	-8.87
	0.95-3.8 g/s	16.58	-96.49	7.27	-12.9

It can be seen that the parameters of the linear approximations made based on the numerical results are much larger than those based on the experimental results. As mentioned before, the numerical results have shown that the sensitivity of the oscillation is larger when the annular channel is 0.5mm, but the experiment results have concluded the opposite. The differences are smaller though, especially for numerical results. Certainly, errors are expected in the numerical results. The assumptions made in the numerical models about the geometry, material properties and boundary conditions are all possible sources of error. Nevertheless, the apparent difference between the two sets of parameters does not necessarily repudiate the numerical results completely. Several factors in the experiments could also have been the culprits of the deviations between the two groups of results and are discussed below.

First of all, in the final numerical models, the sensor surface is assumed to be a grey surface with

a total hemispherical surface absorptivity (emissivity) of 0.4 that was suggested in the original study [15]. However, the actual surface absorptivity of the newly built sensor was never measured in the present study and some degree of spectral and directional variations were expected according to [27]. While in the simulation, black body emission was assumed at the pressure outlet boundary, the majority of the incident radiation should fall into the $0.2\mu\text{m}$ to $5\mu\text{m}$ range in the experiment. Unlike in the simulation, the majority of the incident radiation heat flux probably came from a narrow angle about the sensor surface normal. Hence, it was the surface absorptivity within this wavelength and incident angle range that determined the experiment results. Therefore, deviations between numerical and experimental results were expected. Moreover, the change of the characteristics of the sensor surface can be visually observed after series of tests (Figure 6-1), which indicates that the surface absorptivity probably has changed during the experiment.



Figure 6-1: “Clean” heat flux sensor surface a) before and b) after experiments

Based on the condition of the “dirty” heat flux sensor, more dramatic change in surface characteristics is likely to occur if the “clean” sensor is deployed into the boiler of the power station for a long period of time. As shown in Figure 6-2, the surface of the “dirty” heat flux sensor certainly has experienced more severe change in characteristics over the series of tests.

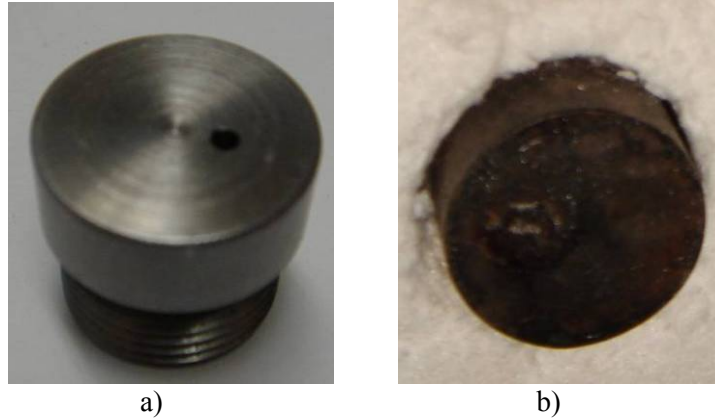


Figure 6-2: “Dirty” sensor surface a) before and b) after experiments

During the experiment, the atmosphere was ash-free. Therefore, the difference between the final surface characteristics of the “clean” and “dirty” is mostly due to the stronger radiation that the “dirty” sensor has endured as it was directly exposed to the heat source while the “clean” sensor was behind the sapphire window. In the real scenario, although the “clean” sensor could probably avoid erosion caused by the ash deposit, the intense radiation in the boiler and high pressure steam from the soot blower will unavoidably alter the characteristics of the surface of the “clean” sensor and hence the surface radiation absorptivity. Nevertheless, the problem might be alleviated by oxidizing the sensor prior to the calibrations process.

In the present work, the incident radiation heat flux was estimated based solely on the radiation transmitted through the sapphire disc while the tip of the “clean” heat flux sensor was essentially placed in a small cavity that was formed by the aluminum brackets, front plate and the aluminum tube which would likely cause multiple radiation reflection and hence increase the actual amount of radiation heat flux received by the sensor surface. Also, although the sensor surface was kept at a certain distance away from the sapphire window, some impact on the air flow structure at the top sensor surface was still expected especially when the distance was small. Even under larger sensor-to-window distances, because the air was ejected into a small cavity rather than an unconstrained environment assumed in the simulation, the flow structure and the hence heat transfer pattern at the top sensor surface were likely to be affected by the flow within the cavity.

The radiation source used in the experiment is less ideal (as mentioned in Chapter 5, spherical blackbody furnace that has uniform cavity temperature and surface emissivity was used for sensor calibrations) but this difference in radiation source is not considered the major source of deviation. The furnace used in this experiment has a rectangular cavity with the heating elements embedded on the two side surfaces and the bottom surface of the cavity. The temperature of the furnace was monitored by a thermocouple installed at the rear surface of the cavity. Although the temperature difference between the elements and the bricks are expected to be measurable, since the elements only take about 7.2% of the total area and because of the geometry of the cavity, the influence of the heating elements on the radiation heat flux imposed on the sensor surface is likely to be small. On the other hand, the set temperature was maintained by constantly switching the heating element on and off. The element was turned on when the measured temperature was about 10F below the set temperature and turned off once it reached the set temperature. The period of the heating cycle was about 30 seconds. Nevertheless, the influence of this heat flux fluctuation on the “clean” sensor was considered small. As shown in Figure 5-13 and 5-18, although the recorded T_c did show some periodical variation, the magnitude was within 1K.

Notwithstanding that, in an attempt to alleviate the influence of the error in incident radiation heat flux estimation in the experiment, the results from the two groups are looked at from a different perspective. Since the A_c and the RTD are both determined by the amount of radiation heat flux absorbed, the results of them are correlated and summarized below. Linear approximation is applied to quantify the relationship between the A_c and the RTD. For the sensor with 1mm channel, the results are shown in Figure 6-3 and 6-4.

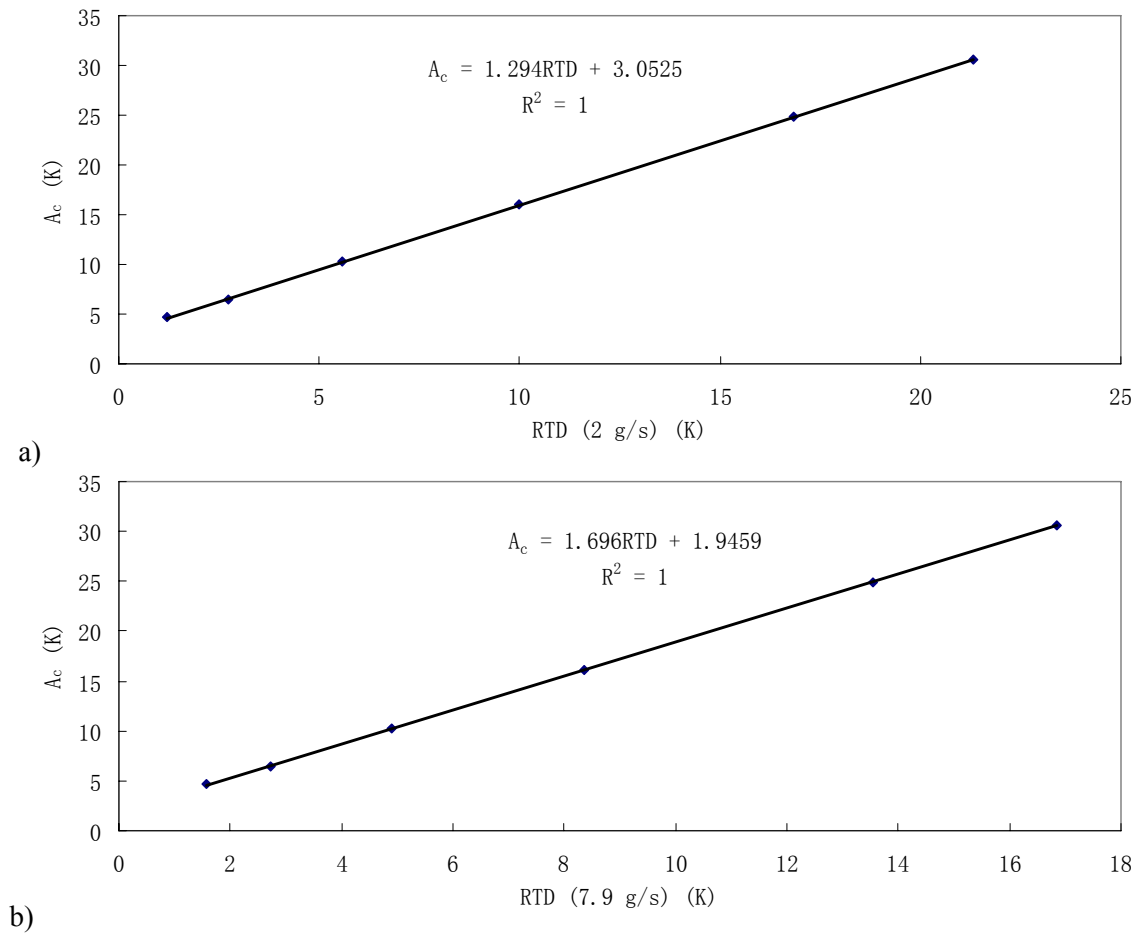


Figure 6-3: Correlation between the amplitude and RTD results, numerical results, a) $\dot{m}=2$ g/s, b) $\dot{m}=7.9$ g/s

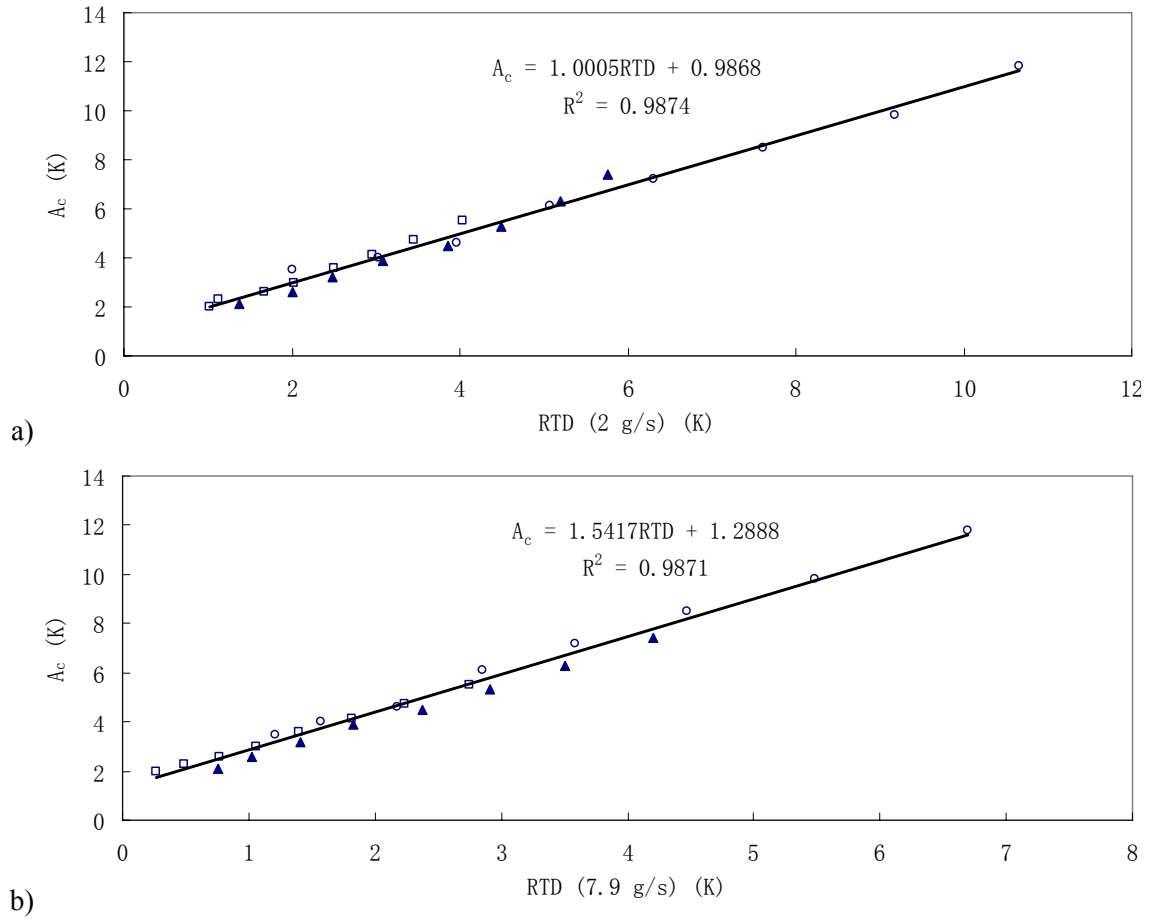


Figure 6-4: Correlation between the amplitude and RTD results, experimental, \square T1-c & T1-s, \blacktriangle T2-c & T2-s, \circ T3-c & T3-s, a) $\dot{m}=2$ g/s, b) $\dot{m}=7.9$ g/s

As shown in the plots above, both experimental and numerical results indicate linear relationships between the A_c and the RTD. The parameters of the linear approximations are much closer to each other compared with the ones shown in Table 6-1, indicating that when the errors in radiation heat flux calculations are not considered, the results from the two groups would be similar. For the sensor with 0.5mm channel, the results are shown in Figure 6-5 and 6-6.

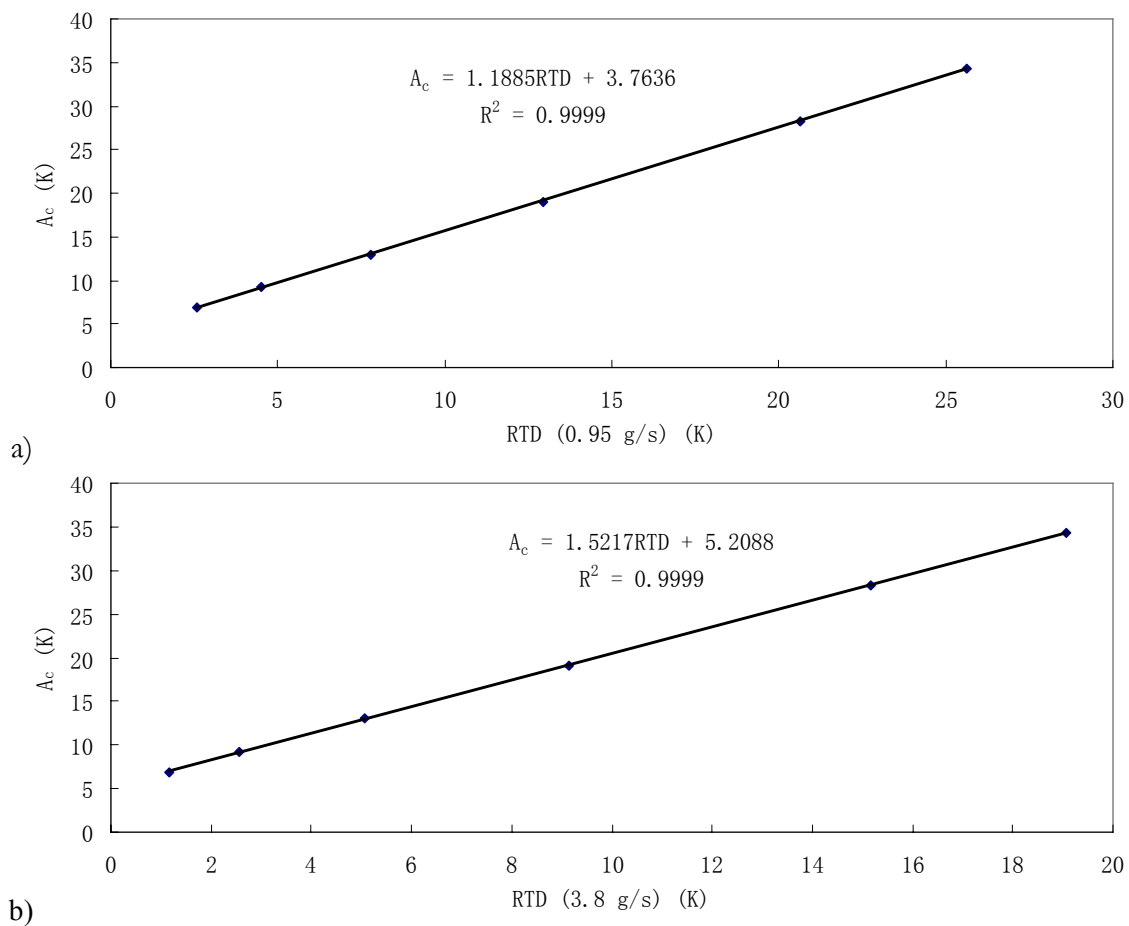


Figure 6-5: Correlation between the amplitude and RTD results, numerical, a) $\dot{m}=0.95$ g/s, b) $\dot{m}=3.8$ g/s

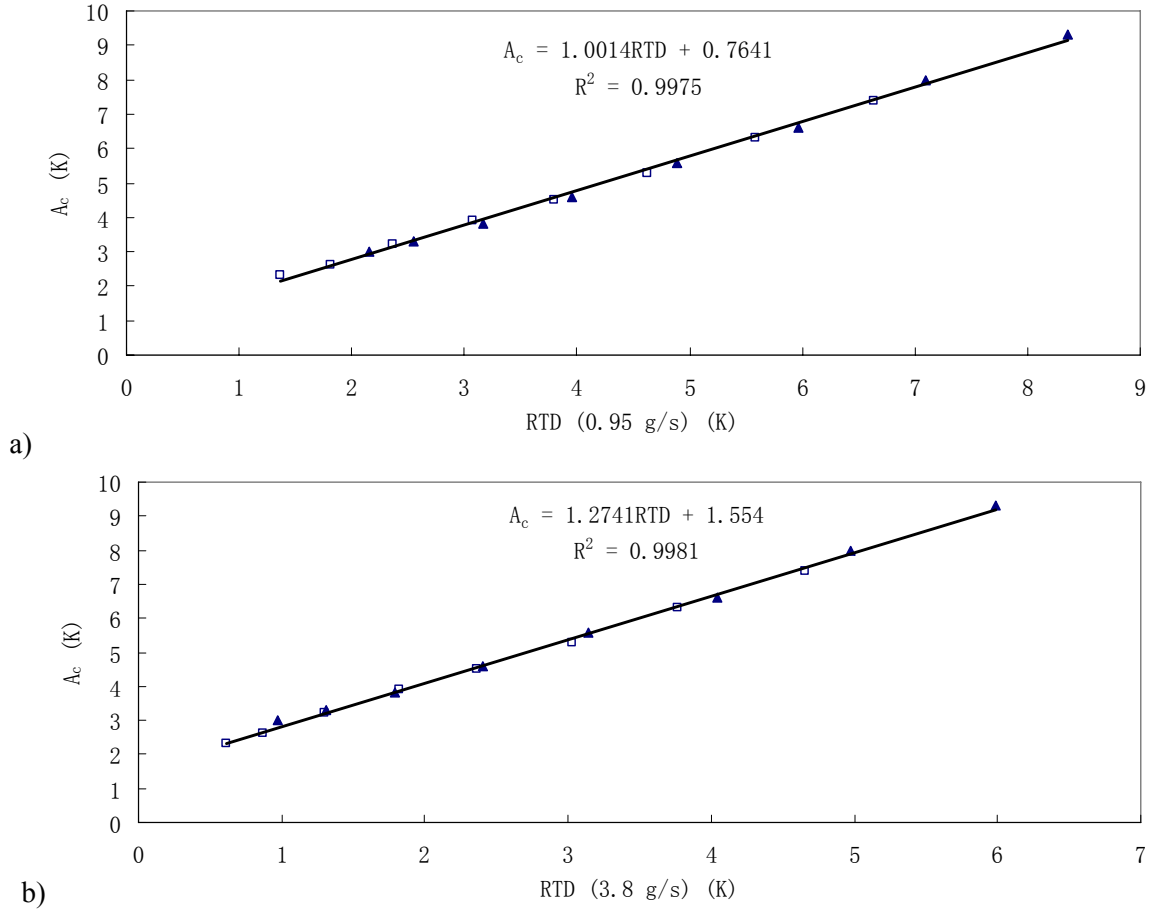


Figure 6-6: Correlation between the amplitude and RTD results, experimental, \square T4-c & T4-s, \blacktriangle T5-c & T5-s, a) $\dot{m}=0.95$ g/s b) $\dot{m}=3.8$ g/s

Again, linear relationships with similar parameters can be observed between the A_c and the RTD when comparing the two groups of results. Another factor that should be taken into consideration, when considering the difference between the numerical and experimental results, is the location of the thermocouple at the periphery of the disc bottom surface. According to the numerical results, the temperature gradient is much larger at the joint of the sensing disc and the insulation shell, where the periphery thermocouple is placed. Figure 6-7 gives an example of the temperature counter at the sensing element.

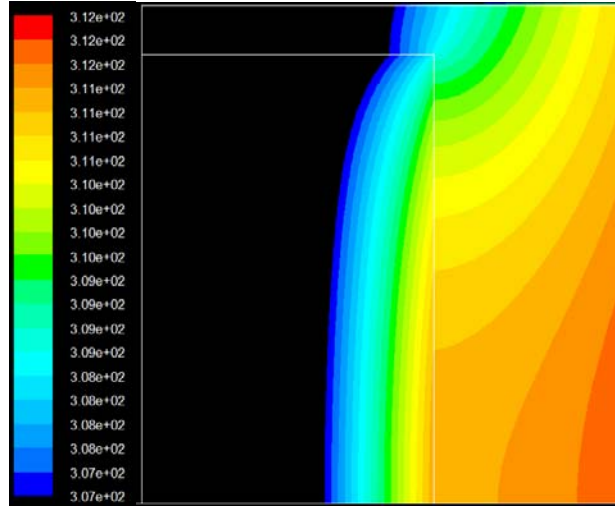


Figure 6-7: Temperature contour at the sensing element (1mm channel, $\dot{m}=2$ g/s, 56.6kW/m^2)

It can be seen that within the sensing disc, the temperature gradient is small at the center and larger at the upper left corner. Therefore, the difference between the two thermocouple measurements is largely dependent on the actual location of the periphery thermocouple, e.g. for the sensor with 1mm channel under 2g/s air flow rate and 56.6kW/m^2 incident radiation heat flux, by moving the thermocouple 0.5 mm towards the center of the sensing disc the RTD would change from 2.75K to 1.61K, and the sensitivity of the sensor (X_{RTD}) under this configuration would change from 0.0444 to 0.0262. In addition, the solder material that was used to secure the thermocouple might alter the local heat transfer pattern at the corner which could also cause the difference between the numerical and experimental results. Also, as mentioned previously, in the simulation, the boundary at the end of the domain was a pressure outlet and was 4.8 mm away from the top surface of the sensor. In the experiment, the air jet was essentially in direct contact with a wall (sapphire window) that was as close as 1.5 cm from the air exit. Although no further study was done to quantify the effect of these differences, it is still reasonable to believe that the jet impingement could have some influence on the CRZ, and hence the convection at the top sensor surface, especially when the sensor-to-window distance is small.

6.2 Discussion on Data Processing Procedures

In this section, the working principles of the three data processing methods are discussed using the experiment results from T4-s-heating. It has been said in Chapter 2 that the temperature of the sensor can be decomposed into three components: T_{air} , T_{dc} and T_{ac} . Under unsteady incident radiation condition, both T_{dc} and T_{ac} become time dependent. In fact, T_{dc} can be considered as the temperature response of the sensor when the air flow rate is constant at the mean oscillation flow rate. Theoretically, a constant air flow rate \dot{m}_{mean} can also be treated as an oscillating flow rate with its mean value equals to \dot{m}_{mean} and its amplitude equals 0. In this case, T_{ac} component is eliminated, and T_c only consists of the time dependent T_{dc} component and the constant T_{air} . In the following example, a quadratic approximation function is applied to the results of T_c from T4-s-heating to extract the T_{dc} and T_{air} components (Figure 6-8).

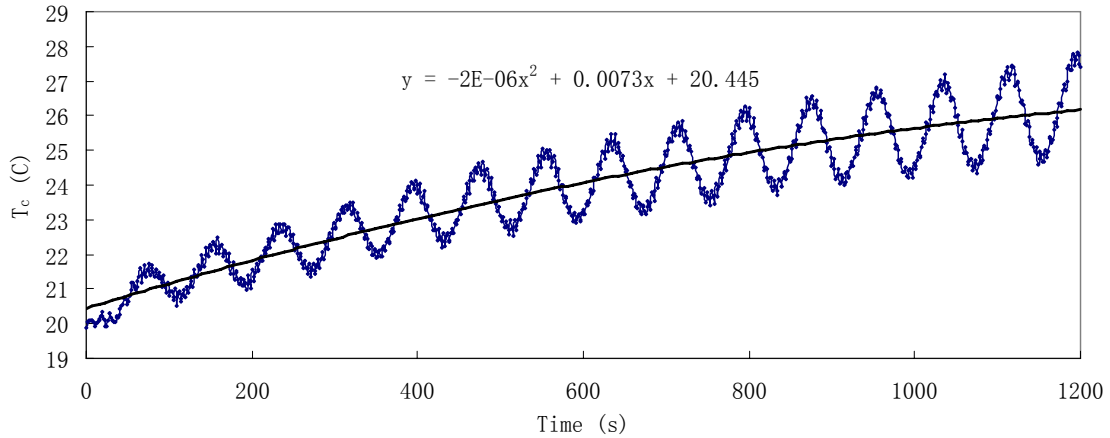


Figure 6-8: Quadratic approximation of T_c (T4-s-heating)

T_{ac} component can be extracted by subtracting the quadratic approximation from the result of T_c . The resulting T_{dc} and T_{ac} components are shown in Figure 6-9 and 6-10.

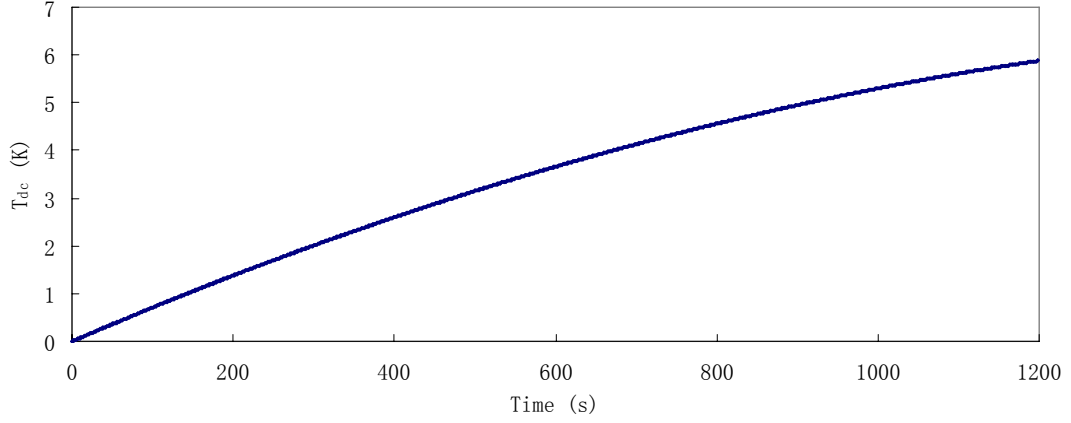


Figure 6-9: T_{dc} component of T_c (T4-s-heating)

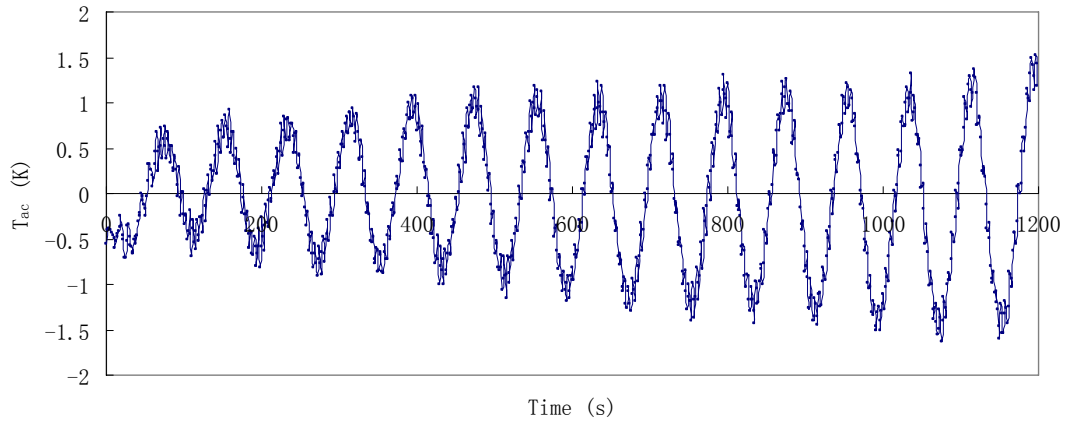


Figure 6-10: T_{ac} component of T_c (T4-s-heating)

It can be seen that T_{dc} is gradually increasing from 0 to 6 while T_{ac} is oscillating about 0 with the amplitude of the oscillation increasing with time. Next, the three data processing procedures are expressed in terms of T_{dc} and T_{ac} components. T_{amb} is assumed to be constant and therefore is not considered here. Equation 6-1 is the decomposed half period temperature difference calculation.

$$dT_{1/2P}(i) = [T_{dc}(i) - T_{dc}(i - 1/2n)] + [T_{ac}(i) - T_{ac}(i - 1/2n)] \quad 6-1$$

As shown in Figure 6-9, T_{dc} is increasing with time, hence the component in the first bracket is always positive. Therefore, even though the component in the second bracket can calculate the peak to peak values of the T_{ac} component, the final result is distorted by the positive component from the first bracket. When the incident radiation heat flux is stable, T_{dc} is constant, the

component in the first bracket then becomes 0 and this procedure can work properly. The decomposed one period temperature difference calculation is shown in Equation 6-2:

$$dT_{1/2P}(i) = [T_{dc}(i) - T_{dc}(i - n)] + [T_{ac}(i) - T_{ac}(i - n)] \quad 6-2$$

In this case, the purpose is actually to capture the rate of change of T_{dc} . The component in the first bracket is always positive in this case but the component in the second bracket is oscillating about 0, hence the final result should be a positively shifted oscillation with the same period as the air flow rate oscillation, which could explain the fluctuations shown in the plots of the one period temperature differences. However, because the magnitude of oscillation in the T_{ac} component is relatively small compared with the value of the T_{dc} component, the T_{dc} component will still dominate the final result. Also, the periodic nature of this component indicates that it has little effect on the estimation at the end of one period. Finally, the decomposed central temperature difference calculation is shown in Equation 6-3:

$$dT_{central}(i) = \left[\frac{T_{dc}(i) + T_{dc}(i - n)}{2} - T_{dc}(i - 1/2n) \right] + \left[\frac{T_{ac}(i) + T_{ac}(i - n)}{2} - T_{ac}(i - 1/2n) \right] \quad 6-3$$

The purpose of this procedure is again to extract the amplitude of the T_{ac} component. However, instead of calculating peak to peak values directly, the component in the second bracket in fact estimates the average of the two consecutive peak to peak values. In this procedure, the effect of the component in the first bracket is essentially eliminated when T_{dc} change within one oscillation period is nearly linear. This gives the central temperature difference procedure the advantage over the half period temperature difference procedure when dealing with unsteady heat fluxes. As shown in the previous chapter, under stable incident radiation heat flux, the T_{dc} component becomes constant, and the result obtained through this procedure becomes the same as the one from the half period temperature difference procedure except the first reading is available one period after the test. From decomposed equation, the limitation of this procedure also becomes

clear. If the change of T_{dc} is very nonlinear within the one period duration, i.e under sudden heat flux drop like the one shown in T4-s-cooling, it will still have a noticeable impact on the final results as shown in the previous chapter. This also implies that a shorter oscillation period will likely produce smoother estimation as the nonlinearity of T_{dc} is likely to be less significant within shorter period of time.

6.3 Comparing RTD and Oscillation Method

It was expected, at the earlier stage of the project, that the sensitivity of the oscillation method would be more consistent than that of the RTD method at high incident radiation heat flux levels. However, this premise was established under simplified conditions and solely from the conduction heat transfer point of view. According to the analysis in Chapter 3, the sensitivity of the oscillation method is determined by the diffusivity and effusivity of the sensor disc material while the sensitivity of the RTD method depends on the thermal conductivity of the material. For most real materials, their thermal properties are usually temperature dependent. For most metals, when experiencing the same temperature change, the change in thermal diffusivity or effusivity is often smaller than that of the thermal conductivity [55]. However, the results of the final simulations did not show any indication of nonlinearity in the relationship between the dependent variables of either measurement method and the incident radiation heat flux over the range of heat flux from 19kW/m^2 to 473kW/m^2 . The finding is in fact not surprising when considering that the overall sensor temperature increase was limited to less than 100K in the numerical results which led to only about 5% increase in thermal conductivity and even smaller change in diffusivity and effusivity.

On the other hand, as mentioned in Chapter 3, the original intention of the oscillation method was simply to create a method that could have higher sensitivity than the RTD method under the same sensor structure. The proposed method was prompted by the results shown in [15] that the

sensitivity of the RTD method was insensitive to the air flow rate change. The sensitivity of the original sensor was increased by about 14% when the air flow rate was changed from $1.9 \cdot 10^{-3}$ to $6.8 \cdot 10^{-3} \text{ m}^3/\text{s}$. This response was opposite to that of the newly built sensor and with a smaller magnitude. It was believed that the sensitivity of the RTD method, based on the original results, had reached its limit under the sensor structure because of the air flow rate available. For the new sensor with 1mm channel (same as the original design), the sensitivity of the RTD method decreased by about 24% as the air flow rate was changed from 2 g/s to 7.9 g/s. The reversed trend means that the sensitivity can be increased simply by using a smaller air flow rate as long as the air jet can still prevent ash deposit. Moreover, it was realized that the sensitivity of the RTD method could also be increased by securing the periphery thermocouple onto the insulation shell. The shell acts as an extension of the sensing disc and as shown in Figure 6-11, the temperature at the shell can be much lower than the temperature at the corner which leads to a larger difference between the two temperature measurements. Of course, according to Equation 2-45, this increase in temperature difference is at a cost of sensor response time since the distance between the two thermocouples is effectively increased.

Chapter 7 Conclusion

An ash monitoring system prototype that consists of a “clean” heat flux sensor and a “dirty” heat flux sensor was developed. The “clean” heat flux sensor, which was the major scope of this project, was designed based on the sensor reported in [14, 15]. Modifications were made to satisfy the requirements in the present project and also to allow easy configuration change which was proved to be helpful later in the study.

The “dirty” heat flux sensor was based on spatial temperature gradient and was only tested experimentally. The “clean” heat flux sensor, with two different measurement methods, one used in the original study that operates under constant air flow rate, and one proposed in the present work that operates under oscillating air flow rate, were studied numerically and experimentally. The original RTD method was based on spatial temperature gradient concept while the new method was based on temporal temperature difference concept. Over the course of study, three data processing procedures were developed so that the sensor with the new method could operate in an on-line basis. The results have shown that the central temperature different procedure was the most reliable one.

Valuable information about the heat transfer pattern at the sensing element was obtained through numerical study and the sensitivities of the sensor at high radiation heat flux levels which can not be reached in the experiment was also tested numerically. Both “clean” and “dirty” heat flux sensors were tested experimentally and the results offered a rough estimation of the relationships between the dependent variables and incident radiation heat flux for sensors with slightly different dimensions and with two different measurement methods. With the current equipment and setup, high accuracy calibration could be difficult. Nevertheless, the experimental results still served as a primary assessment for both sensors.

Contrary to the results shown in the original study, the sensitivity of the RTD method appeared to be more responsive to the air flow rate change with the newly built sensor, and more interestingly, the trend of the response was opposite to that of the original sensor.

The expected nonlinearity at high heat flux levels did not appear in the numerical results of either measurement method. Low overall sensor temperature change was considered the main cause as it meant less change of the thermal properties of the sensing disc.

The numerical and experimental results have shown that under the current sensor structure, the RTD method has the advantage in almost every aspect. Compared with the oscillation method, the RTD method has lower response time, simple data processing procedure, and competitive sensitivity. Notwithstanding the apparent disadvantage, by utilizing an alternative heat flux measurement concept, the oscillation method opens up the possibility for further improvements of the “clean” heat flux sensors. Since it is based on the temporal temperature difference concept, it has almost no requirement on the size of the sensing element and the insulation layer underneath the sensing disc also becomes unnecessary, both of which are essential to generate the spatial temperature difference on which the RTD method is established. In another word, sensors that employ the oscillation method could have smaller and simpler structure. More importantly, the new method has less stringent requirement on the thermal properties of the material for the sensing element, which means a wider range of materials can be selected and thus increases the possibility of resolving the surface characteristic variation problem that is considered crucial for both methods if the sensor is to be used in the boiler.

Modifications can be made in the future on the sensor structure and material to fully utilize the advantages of the oscillation method. Although series of tests were done in the present work, more tests can be done in the future to ensure the accuracy of the sensor calibration.

References

- [1] A. Valero and C. Cortbs, Ash fouling in coal-fired utility boilers: monitoring and optimization of on-load cleaning, *Prog. Energy Combust. Sci*, 22, 1996, 189-200
- [2] N.S. Harding, D.C. O'Connor, Ash deposition impacts in the power industry, *Fuel Processing Technology* 88, 2007, 1082-1093
- [3] Sylwester Kalisz, Marek Pronobis, Investigations on fouling rate in convective bundles of coal-fired boilers in relation to optimization of sootblower operation, *Fuel*, 84, 2005, 927-937
- [4] Alien L. Robinson, Steven G. Guckley, Gian Sclipa and Larry L. Baxter, In Situ Measurements of The Thermal Conductivity of Ash Deposits Formed in a Pilot-scale Combustor, *Impact of Mineral Impurities in Solid Fuel Combustion, IV*, 1999, 485-496
- [5] Xu Z.M, et al, Cost Due to Utility Boiler Fouling in China, *Heat Transfer-Asian Research*, 34(2), 2005, 53-63
- [6] Jan Sandberg¹, Ulf Sand¹ and Rebei Bel Fdhila, Long time investigation of the effect of fouling on the super-heaters in a circulating fluidized biomass boiler, *Int. J. Energy Research*, 30, 2006, 1037-1053
- [7] W.L van de Kamp, M.K. Cieplik, J. Kalivodova and T.J. Zagorski, In-boiler diagnostics of Slagging and Fouling Propensity for Pulverised Coals and Biomass/Wastes Fuels at Laboratory and Full scale, 8th European Confrence INFUB 2008
- [8] Mischa Theis, Bengt-Johan Skrifvars, MikkoHupa and Honghi Tran, Fouling tendency of ash resulting from burning mixtures of biofuels, Part 1: Deposition rates, *Fuel*, 85, 2006, 1125-1130
- [9] Mischa Theis, Bengt-Johan Skrifvars, Maria Zevenhovenm, MikkoHupa and Honghi Tran, Fouling tendency of ash resulting from burning mixtures of biofuels, Part 3: Influence of probe surface temperature, *Fuel*, 85, 2006, 2002-2011
- [10] Marek Pronobis, The influence of biomass co-combustion on boiler fouling and efficiency, *Fuel*, 85, 2006, 474-480

- [11] A.K. Chamber, J.R. Wynnycky and E. Rhodes, Development of a Monitoring System for Ash Deposits on Boiler Tube Surfaces, *The Canadian Journal of Chemical Engineering*, 59, 2, 1981, 230-235
- [12] Minghou Xu, Xiuguang He, J. L. T. Azevedo and M. G. Carvalho, An advanced model to access fouling and slagging in coal fired boilers, *Int. J. of Energy Research*, 26, 2006, 1211-1236
- [13] Enrique Teruel, Cristobal Cortes, Luis Ignacio Diez, Inmaculada Arauzo, Monitoring and prediction of fouling in coal-fired utility boilers using neural networks, *Chemical Engineering Science*, 60, 2005, 5035-5048
- [14] Branislav Brajuskovic, Miodrag Matovic and Naim Afgan, A heat flux-meter for ash deposit monitoring systems—I Ash deposit prevention, *Int. J. Heat mass transfer*, 34(9), 1991, 2291-2301
- [15] Branislav Brajuskovic and Naim Afgan, A heat flux-meter for ash deposit monitoring systems—II “clean” heat flux-meter characteristics, *Int. J. Heat mass transfer* 34(9), 1991, 2303-2315
- [16] Norio Arai, Aritaka Matsunami, Stuart W. Churchill, A Review of Measurements of Heat Flux Density Applicable to the Field of Combustion, *Experimental Thermal and Fluid Science*, 12, 1996, 452-460,
- [17] James V. Beck, Ben Blackwell, Charles R., Jr. St. Clair, *Inverse heat conduction: ill posed problems* (Wiley-Interscience, 1985)
- [18] Schmidt, E. U.S. Patent No. 1,528,383 (1925)
- [19] Frank P. Incropera, David P. DeWitt, *Fundamentals of heat and mass transfer* (John Wiley & Sons, Inc, 2002)
- [20] Diller, T. E.: “*Heat Flux*”, Measurement and Instrumentation Handbook, Ch. 34 in “The Measurement, Instrumentation and Sensors Handbook”, Ed. J. G. Webster, CRC Press, Boca Raton, Florida.
- [21] H.A. Warda, S.Z. Kassab, K.A. Elshorbagy and E.A. Elsaadawy, An experimental investigation of the near-field region of free turbulent round central and annular jets, *Flow Measurement and Instrumentation*, 10, 1999, 1-14

- [22] Himadri Chattopadhyay, Numerical investigations of heat transfer from impinging annular jet, *International Journal of Heat and Mass Transfer*, 47, 2004, 3197-3201
- [23] H.J. Sheen, W.J. Chen and I.S. Wu, Flow patterns for an annular flow over an axisymmetric sudden expansion, *J. Fluid Mech*, 350, 1997, 177-188
- [24] M. Vanierschot and E. Van Den Bulck, influence of swirl on the initial merging zone of a turbulent annular jet, *Physics of fluids*, 20, 10, 2008, 105104-105104-18
- [25] Fluent Incorporated. FLUENT User's Guide, 2008
- [26] P.H. Oosthuizen, David Naylor, *Introduction to Convective Heat Transfer Analysis*, (William C Brown Pub, 1998)
- [27] Robert Siegal and John Howell, *Thermal Radiation Heat Transfer* 4th ed (New York: Tayler & Francis, 2002)
- [28] A. Aziz, *Conduction Heat Transfer*, John Wiley & Sons, 2003
- [29] Andreas Frank Hoffie (2006) Master thesis (Department of Mechanical Engineering, Virginia Polytechnic institute and State University, Blacksburg, Virginia, USA)
- [30] Agustin Salazar, Energy propagation of thermal waves, *European Journal of Physics*, 27, 2006, 1349-1355,
- [31] Robert Gardon, An Instrument for the Direct Measurement of Intense Thermal Radiation, *The review of scientific instruments*, f22 (5), 1952, 366-370
- [32] W. J. Cook and F. J. Felderman, Reduction of data from thin-film heat transfer gages: A concise numerical technique, *AIAA J.*, 4, 1966, 561-562
- [33] E.W. Northover and J.A Hitchcock, A heat flux meter for use in boiler furnace, *J.Sci. Instrum.*, 44, 1967, 371-374
- [34] Baker, H. D., Ryder, E. A. and Baker, N. H., *Temperature Measurement in Engineering* (Omega Press, Stamford, 1, 1975)

- [35] Neal, S. B. H. C. and Northover, E. W., The measurement of radiant heat flux in large boiler furnaces-I. problems of ash depositions relating to heat flux, *Int. J. Heat Mass Transfer*, 23, 1980, 1015-1021
- [36] Neal, S. B. H. C., Northover, E. W. and Preece, R. J., The measurement of radiant heat flux in large boiler furnaces-II. development of flux measuring instruments, *Int. J. Heat Mass Transfer* 23, 1980, 1023-1031,
- [37] Hoogendoorn, C.J., Ballintijn, C.M., and Dorresteyn, W.R., Heat flux studies in vertical tube furnaces, *Journal of the institute of fuel*, 1970, 511-516
- [38] N. Martins, M.G. Carvalho, N.H. Afgan and A.I. Leontiev, A new instrument for radiation heat flux measurement- analysis and parameter selection, *Heat Recovery Systems & CHP*, 15(8), 1995, 787-796
- [39] N. H. Afgan and A. I. Leontiev, Instrument for thermal radiation flux measurement in high temperature gas flow, *Heat Recovery Systems & CHP*, 15(4), 1995, 347-350,
- [40] N. Martins, M.G. Carvalho, N.H. Afgan and A.I. Leontiev, A radiation and convection flux meter for high temperature applications, *Experimental Thermal and Fluid Science*, 22, 2000, 165-173
- [41] N. Martins, H. Calisto, N.H. Afgan and A.I. Leontiev, The transient transpiration heat flux meter, *Applied Thermal Engineering*, 26, 2005, 1552-1555
- [42] E. P. Stoyarov, Simulation of process in heat sensors based on solution of inverse problems in heat conduction, *Heat and Mass Transfer and Physical Gasdynamics*, Vol.43, No.1, 2005, 071-085
- [43] H. K Versteeg & W Malalasekera, *An introduction to computational fluid dynamics*, Person Education Limited, Edinburgh Gate, 1995
- [44] The Engineering ToolBox, http://www.engineeringtoolbox.com/thermal-conductivity-d_429.html, 2005, (2009 Mar)
- [45] N. W. M. Ko and W. T. Chan, Similarity in the initial region of annular jet: three configurations, *J Fluid Mech*, 84(4), 1978, 641-656
- [46] J. Ballestrin, C.A. Estrada, M. Rodriguez-Alonso, C. Perez-Rabago, L.W. Langley and A. Barnes, Heat flux sensor: Calorimeters or radiometers, *Solar Energy*, 80, 10, 2006, 1314-1320

- [47] National Institute of Standards and Technology, Optical Technology Division,
<http://physics.nist.gov/TechAct.2001/Div844/div844h.html>, (2009 Mar)

- [48] Omega Engineering Inc,
http://www.omega.com/literature/transactions/volume1/calibrate2.html#blackbody_cavities ,
(2009 Mar)

- [49] A.V.Murthy B.K. Tsai and R.D Saunder, High-heat-flux sensor calibration using blackbody radiation, *Metrologia*, 1998, 25, 501-504

- [50] J.R. Filtz, T. Valin, J. Hameury and J. Dubard, New vacuum blackbody cavity for heat flux meter calibration, *Int, J, Thermophys*, 30, 1, 2009, 236-248

- [51] J Ballestrin, C.A. Estrada, M. Rodriguez-Alonso, C. Perez-Rabago, L.W. Langley and A. Barnes, High-heat-flux sensor calibration using calorimetry, *Metrologia*, 41, 2004, 314-318

- [52] N. Martins, M.G. Carvalho, N.H. Afgan, A.I. Leontiev, Experimental verification and calibration of the blow-off heat flux sensor, *Applied Thermal Engineering*, 18, 6, 1998, 481-489

- [53] ESCO products, Inc, <http://www.escoproducts.com/html/sapphire.html>, 2005, (2009 Mar)

- [54] John R. Howell, A catalog of radiation heat transfer configuration factors
<http://www.me.utexas.edu/~howell/sectionc/C-41.html>, (2009 Mar)

- [55] Carslaw HS and Jaeger JC, *Conduction of Heat in Solids* (London: Oxford University Press, 1959)

Appendix A

Preliminary model results

As mentioned in Chapter 3, the results of the preliminary models identified several parameters that are relevant to the sensitivity of the oscillation method. Since incompressible flow was assumed in the preliminary model, velocity inlet boundary was used to control the air flow. Air flow speed at the inlet was set to oscillate between 20m/s and 30m/s in the square wave form and the BFT was set at 1000K. Figure A-1 illustrates the T_c oscillation obtained under two oscillation periods: 20s and 40s as well as the upper (with 20m/s air inlet velocity) and lower (with 30m/s air inlet velocity) steady state temperatures under the same BFT.

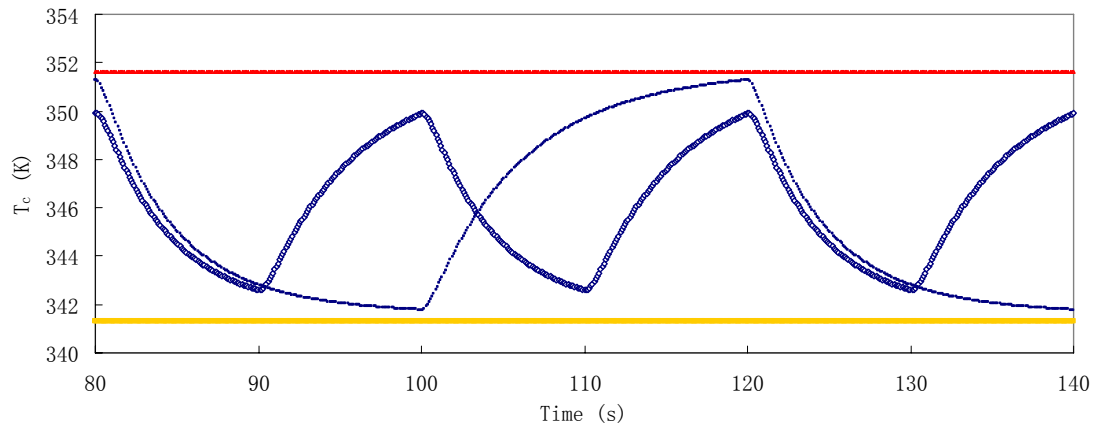


Figure A- 1: Effect of flow oscillation period, ◇ P=20s, ■ P=40s, △ T_c at 20m/s ■ T_c at 30m/s

As shown above amplitude of the temperature oscillation increases with the oscillation period. Since the flow oscillation is in square wave form, when experiencing a stable incident radiation heat flux, T_c oscillates exponentially within the upper and lower steady state temperatures that are determined by the air flow rate, surface radiation absorptivity and material properties of the sensing disc. The effect of the thermal properties of the sensing disc was also tested in the preliminary model. Figure A-2 compares the results from two simulations that specified the thermal properties of sensing disc according to stainless steel and nickel respectively.

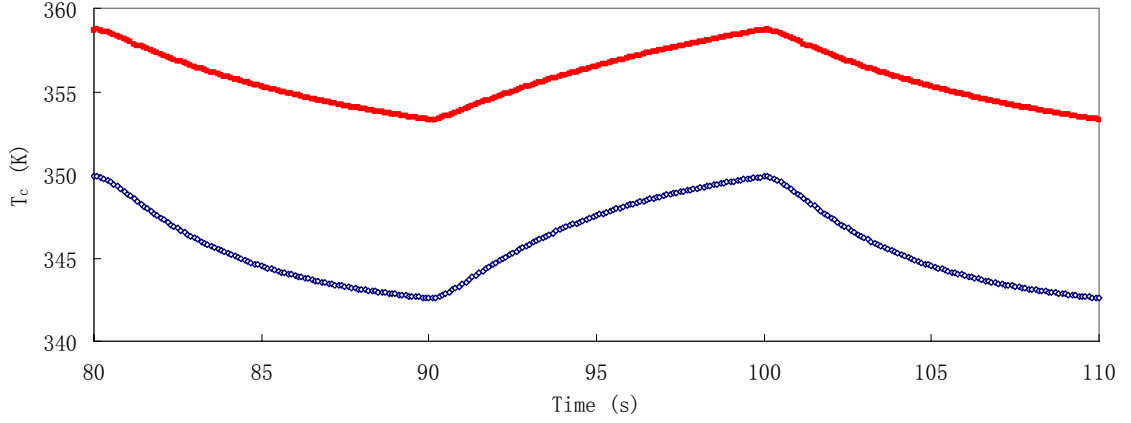


Figure A- 2: Effect of the thermal properties of the sensing disc, \diamond steel, \blacksquare nickel

In this case, the inlet air velocity was set to oscillate between 20 and 30m/s and with a period of 20 second, the BFT was set at 1000K, and the material properties were set constant in this test. It can be seen that under the same circumstance, the amplitude of the T_c oscillation is lower but the overall value is higher when the properties of nickel is applied to sensing disc ($\rho=8900\text{ kg/m}^3$, $k=90.7\text{ W/m}\cdot\text{K}$, $c_p=444\text{ J/kg}\cdot\text{K}$ [19]), under the environment. Using the same flow condition as the pervious test, the effect of the thickness of the sensing disc was tested under a fluctuating incident radiation heat flux with a stable mean value. Sensors with 2mm and 3mm thick sensing discs were tested and the results are compared in Figure A-3.

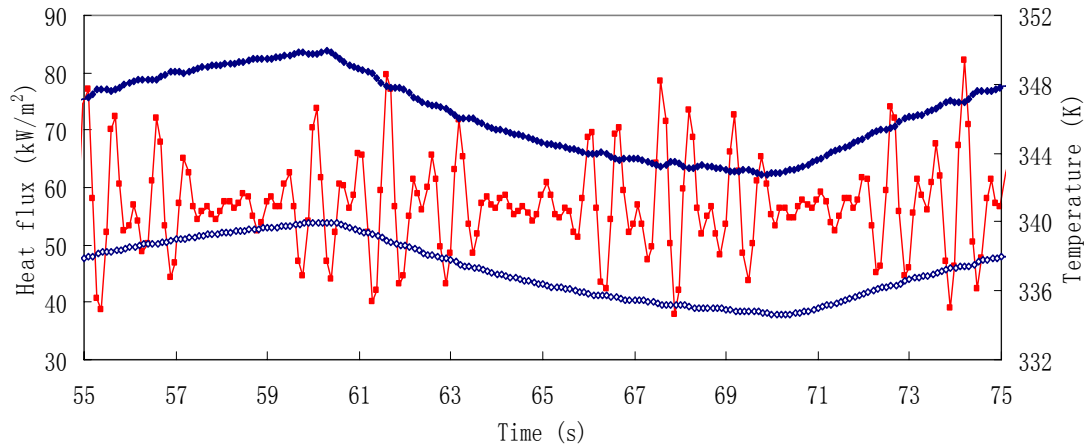


Figure A- 3: Effect of the thickness of the sensing disc, \blacksquare Heat flux, \blacklozenge T_c ($\delta=2\text{mm}$), \diamond T_c ($\delta=3\text{mm}$)

As expected, the overall value of T_c is lower when the thickness of the sensing disc is higher. Also the heat flux fluctuations generated by the radiation source as well as the oscillation of the air flow rate are more damped when using the thicker sensing disc, which causes a smoother but flatter T_c oscillation compared with the one using the 2mm thick sensing disc. These preliminary tests confirmed the relationship between the sensor parameters and the amplitude of the T_c oscillation suggested in Equation 3-15.

Besides the cases under stable incident radiation heat fluxes, the preliminary models also tested the oscillation method under various unsteady incident radiation heat flux situations, which allowed the problem associated with the oscillation method to be realized in the early stage of the project and provided enough time for the development of the data processing procedures that are essential for the application of the oscillation method. Results obtained from two different unsteady heat flux situations are shown here to illustrate the behavior of T_c under unsteady heat fluxes. The first case is a two-step-change heat flux and the second case consists of three sections: gradual heating, steady heat flux, and gradual cooling. Figure A-4 illustrates the step change heat flux and the corresponding response of T_c .

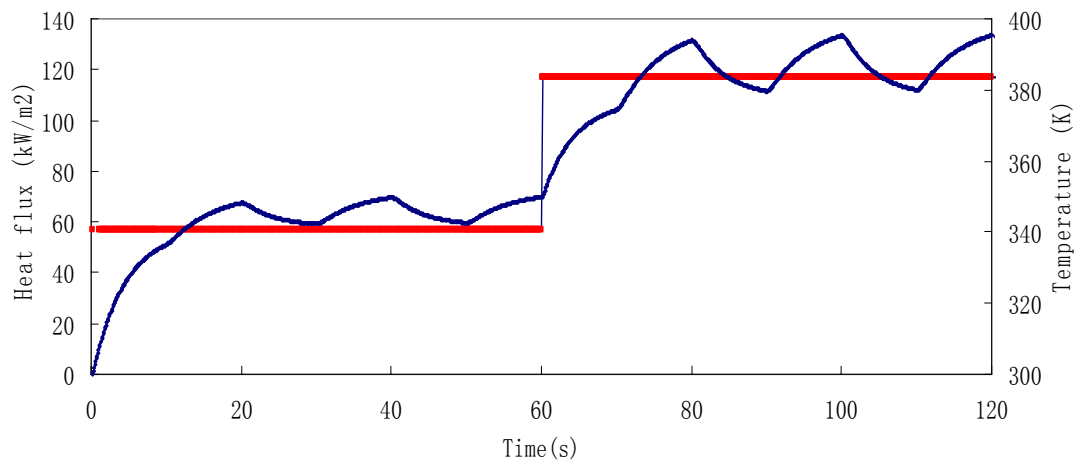


Figure A- 4: Unsteady heat flux and the corresponding T_c oscillation (case 1), ■ Heat flux, ◆ T_c

The heat flux jumped from 0 to 56kW/m² at the beginning of the simulation and then jumped from 56kW/m² to 120kW/m² 60 seconds later. The period of the air flow oscillation in this case is

20 seconds. As shown above, the T_c oscillation requires about 20 seconds (one period) to stabilize after the interruption caused by the sudden heat flux change. As mentioned in Chapter 3, the half period temperature difference procedure was first created when realizing the A_c can be extracted by calculating the peak to peak temperature difference. However, large errors were found at the transition period when using this procedure. The heat flux and the corresponding T_c oscillation of the second case are shown in Figure A-5.

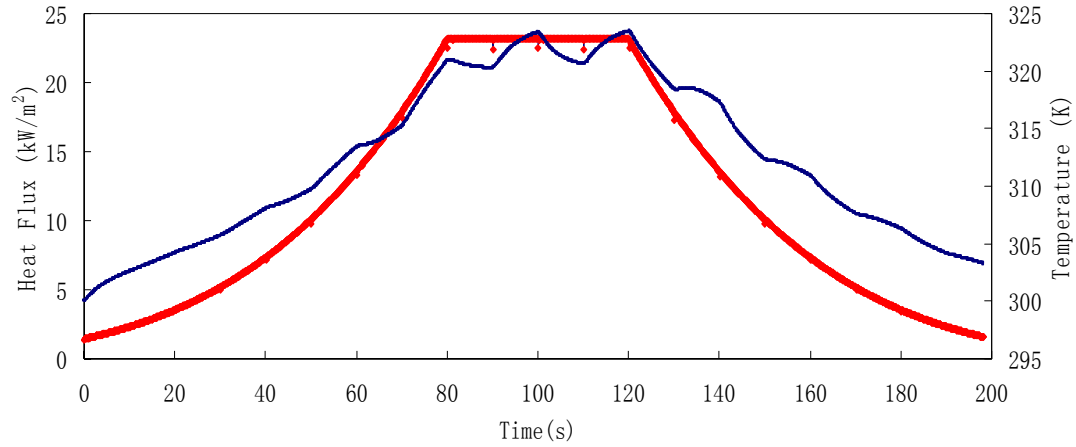


Figure A- 5: Unsteady heat flux and the corresponding T_c oscillation (case 2), ■ Heat flux, ◆ T_c

Same air flow configuration was applied in the second case. As shown above, the T_c oscillation is distorted during the heating and cooling period, and stabilized oscillation can only be seen in the steady heat flux section from 80 second to 120 second. The result of the second case raised serious doubt about the feasibility of the oscillation method as the A_c calculated by the half period temperature difference procedure always gives false estimation under unsteady heat flux and it is unrealistic to assume that the heat flux in the boiler will always remain constant. Attempts were made to resolve this problem which led to the development of the secondary one period temperature difference procedure and eventually and the central temperature difference procedure. From the preliminary results, it was also realized that the results obtained using greater oscillation period are more susceptible to the heat flux variation.

Appendix B

FLUENT, UDF

(Preliminary model, square wave form air flow rate, random fluctuation heat flux)

/* UDF for setting target mass flow rate in pressure-outlet */

```
#include "udf.h"
```

```
DEFINE_PROFILE(inlet_velocity, t, nv)
```

```
{  
    face_t f;
```

```
    real flow_time = RP_Get_Real("flow-time");
```

```
    int phase, od, stupid;
```

```
    phase = (flow_time)/10;
```

```
    stupid = -1;
```

```
    od = pow(stupid, phase);
```

```
    if (od <= 0.0)
```

```
    {  
        printf("Time          = %f sec. \n", flow_time);  
        printf("inlet velocity set at 20 m/s \n");
```

```
        begin_f_loop(f, t)
```

```
        {  
            F_PROFILE(f, t, nv) = 20.0 ;  
        }
```

```
        end_f_loop(f, t)
```

```
    }
```

```
    else
```

```
    {  
        printf("Time          = %f sec. \n", flow_time);  
        printf("inlet velocity set at 30 m/s \n");
```

```
        begin_f_loop(f, t)
```

```
        {  
            F_PROFILE(f, t, nv) = 30.0 ;  
        }
```

```
        end_f_loop(f, t)
```

```
    }
```

```
}
```

```
DEFINE_PROFILE(back_flow_temp, t, i)
```

```
{  
    face_t f;
```

```
    real ft = RP_Get_Real("flow-time");
```

```
    int phase, od, stupid;
```

```

begin_f_loop(f,t)
{
    F_PROFILE(f,t,i) = sin(10.0*ft-2.0)*sin(0.5*ft-4.0)*sin(2.0*ft+1.0)*100.0+1000.0;
}
end_f_loop(f,t)
}

```

(Final model ,0.5mm channel, sinusoidal air flow rate)

/* UDF for setting target mass flow rate in pressure-outlet
*/

#include "udf.h"

```

DEFINE_PROFILE(mass_flow, t, nv)
{
    face_t f;
    real flow_time = RP_Get_Real("flow-time");
    double mh, ml, m_amp, m_mean, w, pi;
    mh=70.736;
    ml=17.684;
    w=0.025;
    pi=3.1415926;
    m_amp = (mh-ml)/2.0;
    m_mean = (mh+ml)/2.0;
    begin_f_loop(f,t)
    {
        F_PROFILE(f,t,nv) = m_amp*sin(w*pi*flow_time)+m_mean;
    }
    end_f_loop(f,t)
}

```

Appendix C

Excel VB, flow control and data acquisition code

```
Private Sub cmdInit_Click()
```

```
'Shared parameters-----
Dim BoardName As String
Dim BoardNum As Integer
Dim FirstPoint As Long ' set first element in buffer to transfer to array

Dim CBCount As Long ' Number of data points
Dim NumofP
Dim Period!
Dim Freq!
Dim HalfP!
Dim RunTime!
Dim Vh!
Dim V!
'Define parameters for temperature channels-----
Dim UlstatT As Integer
Dim OptionT As Integer ' Temperature signal options
Dim CBScale As Integer 'Temperature unit
Dim LowChan As Integer ' Start Channel index
Dim HighChan As Integer ' High Channel index
Dim NumChanT As Integer ' Number of channels
Dim Temperature!()

'Define Flow output signal parameters-----
Dim UlstatFO As Integer ' flow output
Dim ChanO As Integer ' Channel Number
Dim GainO As Integer ' Gain
Dim OutVolt!
Dim OptionO&
'Define Flow input data parameters-----
Dim ChanI As Integer ' Channel Number
Dim UlstatFI As Integer ' flow input
Dim GainI As Integer ' Gain
Dim FlowRate!
'Channel designations -----
Dim AAir As Integer ' Air flow rate
Dim CleanTc As Integer ' Center disc temperature "clean sensor"
Dim CleanTp As Integer ' Periphery disc temperature "clean sensor"
Dim DirtyTc As Integer ' Center disc temperature "dirty sensor"
Dim DirtyTp As Integer ' Periphery disc temperature "dirty sensor"
Dim Furnace As Integer ' Furnace temperature
'Dimension arrays to hold data-----
Dim ADData() As Integer ' 1D array to hold the input values
Dim AAir_flow() As Integer ' Annular air flow rate
'-----
```

```

Dim i As Integer
Dim j As Integer
Dim k!
'-----
'Shared parameters-----
NumofP = Range("$B$10")
BoardNum = 0
Period = Range("$B$11")

'CBCount = Range("$B$2")
'CBCount = (CBCount + 1) / 64 ' total number of data points to collect
'CBCount = CBCount * 64 'Because it is a USB/USB/PMD-1608FS the number of points
                        'must be an integer multiple of 64
'If CBCount < 64 Then CBCount = 64
'Range("$B$2").Value = CBCount
FirstPoint = 0
'output signal parameters-----
ChanO = 0 'VDAC0
GainO = BIP5VOLTS
OptionO = DEFAULTOPTION
'flow data parameters-----
GainI = UNI5VOLTS
ChanI = 7 'Channel0
'Temperature parameters-----
CBScale = CELSIUS 'Temperature conversion unit in Celsius
LowChan = Range("$D$4")
HighChan = Range("$D$5")
NumChanT = HighChan - LowChan + 1
ReDim Temperature(0 To NumChanT)
OptionT = FILTER 'option for cbTIn ( FILTER, NOFILTER)
'-----

Workbooks("sin-05-gap.xls").Activate
'-----
' Collect the values with cbAInScan%()
' Parameters:
' BoardNum% :the number used by CB.CFG to describe this board
' LowChan% :the first channel of the scan
' HighChan% :the last channel of the scan
' CBCount& :the total number of A/D samples to collect
' CBRate& :sample rate
' Gain :the gain for the board
' ADDData :the array for the collected data values
' Options :data collection options
'-----

i = 1
j = 2
Vh = Range("$B$8")
Vl = Range("$B$9")
Freq = Range("$B$12")
k = Timer

```

```

Do While Timer < k + Period * NumofP
    RunTime = Timer - k
    Cells(i + 1, 7) = RunTime
    OutVolt = (Vh - Vl) / 2# * Sin(RunTime * Freq * 3.1415926) + (Vh + Vl) / 2#
    UlstatFO = cbVOut(BoardNum, ChanO, GainO, OutVolt, OptionO)
    'Measure flow rate-----
    UlstatFI = cbVIn(BoardNum, ChanI, GainO, FlowRate, OptionO)
    ' If UlstatFI <> 0 Then Stop
    ' Measure Temperature-----
    UlstatT = cbTInScan(BoardNum, LowChan, HighChan, CBScale, Temperature(0), OptionT)
'temperature acquisition
    If UlstatT <> 0 Then Stop
    Cells(i + 1, 8) = FlowRate
    Cells(i + 1, 17) = OutVolt * 2
    'If NumChanT > 2 Then
    Cells(i + 1, 9) = Temperature(0) 'dirty sensor temperature high
    Cells(i + 1, 10) = Temperature(1) 'dirty sensor temperature low
    ' End If
    Cells(i + 1, 11) = Temperature(2) 'clean sensor temperature high
    Cells(i + 1, 12) = Temperature(3) 'clean sensor temperature low
    'Cells(i + 1, 16) = Temperature(4) 'plate back temperature/ water temperature in
    'Cells(i + 1, 13) = Temperature(0) - Temperature(1) 'RTD
    'Cells(i + 1, 14) = Temperature(2) - Temperature(3) ' Dirty dT
    'If Timer > k + Period Then
    'HalfP = (i + j) / 2
    'Cells(j, 15) = Abs((Cells(i, 11) + Cells(j, 11)) / 2 - Cells(HalfP, 11))

    'j = j + i
    ' End If
    i = i + 1
Loop
    UlstatFO = cbVOut(BoardNum, ChanO, GainO, 1#, OptionO)
End Sub

```

Appendix D

Matlab, data processing

(Combine HPTD with OPTD)

```
function ConvertS (B, P, F1,iHF)
%input time and temperature data, period, conversion factor
%and initial heat flux
%A is the fluent output temperature data, with time
%P is period or air oscillation, F1 is factor for amplitude conversion
%F2 is factor for dT slope integration
%iHF is the initial heat flux
A=Predata(B,P);
%add pre-heat flux data
time=A(:,1);
temp=A(:,2);
range = length (temp); %original data range
range2= range-P/2; %1/2 period dT range
range3= range-P; %1 period dT range

% calculate dT 0.5P and dT 1P
for k = 1:range2;
    dT1(k)=temp(k+P/2)-temp(k);
    %half period temperature difference
    %10 represents 10 data points per second
end;
    %calculate dT1 wave magnitude
j=0;
while P*0.5*j < (range2-P);
    Amp(j+1)=max(abs(dT1(j*P*0.5+1:(j+1)*P*0.5)));
    %calculate the amplitude of the wave every half period
    %convert the amplitude into average heat flux in this half period
    for k=1:P*0.5;
        HF1(k+j*P*0.5)= Amp(j+1)*F1;
    end;
    j=j+1;
end;
range4 = length(HF1);
%heat flux estimation through integration method
HF2(1)= iHF;
%F2 is determined by the temperature of the sensor disc
%F2=a*Tavg+b , a and b estimated based on the temperature and actual flux
a=6e-3;
b=-0.68;
%estimate the heat flux
for k = 1:range3;
    dT2(k)=temp(k+P)-temp(k);
    %one period temperature difference-slope
    F2=a*(temp(k+P)+temp(k))/2+b;
```



```

    %temperature dependent integral factor
    HF2(k+1)=HF2(k)+dT2(k)/P*F2;
end;

%combination of two method : hybrid method

k=1;

while k<range4+1;
    %switching criteria is the 1P temperature difference
    if abs(dT2(k))<=1;
        HF3(k)= HF1(k);
    else
        F2=a*(temp(k+P)+temp(k))/2+b;
        if k==1;
            HF3(k)=iHF+dT2(k)/P*F2;
        else
            HF3(k)=HF3(k-1)+dT2(k)/P*F2;
        end;
    end;
    k=k+1;
end;

```

(Second step in HPTD and CTD)

```

function Searchmax (A)
Time=A(:,1);
Temp=A(:,2);
P=80;
window=int16(33/1.246);
space=int16(40/1.246);
N=int16((Time(end)-Time(1))/P*2);
temp=0;
for i=1:N;
    for j=((i-1)*space+8):((i-1)*space+window+8)
        if Temp(j)>=temp;
            temp=Temp(j);
            jj=j;
        end
    end
    peak(i)=mean(Temp((jj-1):(jj+1)));
    time(i)=Time(jj);
    temp=0;
    i;
end;
plot(time,peak,'--rs','LineWidth',2,...
     'MarkerEdgeColor','k',...
     'MarkerFaceColor','g',...
     'MarkerSize',10)

```